5-2010

An Experimental investigation of chemical mass transfer processes in crystallizing, hydrous silicate magmas: The genesis of ore deposits and metasomatic fluids

Aaron S. Bell
University of Nevada Las Vegas

AN EXPERIMENTAL INVESTIGATION OF CHEMICAL MASS TRANSFER PROCESSES IN CRYSTALLIZING, HYDROUS SILICATE MAGMAS: THE GENESIS OF ORE DEPOSITS AND METASOMATIC FLUIDS

by

Aaron S. Bell

Bachelor of Science
University of Oklahoma
2006

A dissertation submitted in partial fulfillment of
the requirements for the

Doctor of Philosophy Degree in Geoscience
Department of Geoscience
College of Science

Graduate College
University of Nevada, Las Vegas
May 2010

UNLV
UNIVERSITY OF NEVADA LAS VEGAS

THE GRADUATE COLLEGE

We recommend the dissertation prepared under our supervision by

Aaron S. Bell

entitled

An Experimental Investigation of Chemical Mass Transfer Processes in Crystallizing, Hydrous Magmas: The Genesis of Ore Deposits and Metasomatic Fluids

be accepted in partial fulfillment of the requirements for the degree of

Doctor of Philosophy in Geoscience

Adam Simon, Committee Chair

Eugene Smith, Committee Member

Oliver Tschauner, Committee Member

Jean Cline, Committee Member

Clemens Heske, Graduate Faculty Representative

Ronald Smith, Ph. D., Vice President for Research and Graduate Studies
and Dean of the Graduate College

May 2010

ABSTRACT

An Experimental Investigation of Chemical Mass Transfer Processes in Crystallizing, Hydrous Silicate Magmas: The Genesis of Ore Deposits and Metasomatic Fluids

by

Aaron S. Bell

Dr. Adam Simon, Examination Committee Chair
Assistant Professor of Geology
University of Nevada, Las Vegas

This dissertation is comprised of three broadly related experimental petrology projects on phase equilibria and noble metal solubility in hydrous silicate melts. Chapters two and three combine experimental petrology with high precision laser ablation inductively coupled plasma mass spectrometry (LA-ICP-MS) analysis of experimental run products in order to quantitatively constrain the behavior of the investigated metals. Chapter four presents experimental evidence detailing a novel oxidation mechanism for degassing silicate liquids as well as exploring the geochemical consequences of the proposed mechanism.

Chapter two presents the results of an experimental study on Au, Pt, and Pd behavior in coexisting silicate melt-sulfide-oxide phase assemblages. Data from this study suggest the combined effect of oxygen and sulfur fugacity dictates the identity of stable magmatic sulfide phase assemblages, as well as dictating the concentration of Pt and Pd in monosulfide solid solution; both of these factors are critical components that determine metal tenor and the ore-deposit forming potential of a given magma.

Chapter three presents an experimental study of Au solubility in hydrous, chloride rich basaltic liquids as a function of oxygen fugacity (fO_2). LA-ICP-MS determined Au

concentrations in the quenched melt do not strictly adhere to the relationship between fO_2 and Au solubility predicted for a monovalent Au oxide species. The observed relationship between Au and fO_2 suggests the existence of alternative, non-oxide species in the melt. The solubility data presented in this chapter constrain the maximum Au concentration of natural hydrous basaltic liquids to values less than 2 μg g^{-1}.

Chapter four presents experimental evidence suggesting a new mechanism for chloride degassing induced auto-oxidation of silicate liquids. The chemical exchange between silicate melts and chloride bearing fluids preferentially removes ferrous iron from the melt relative to ferric iron. The net effect of this preferential scavenging effect is to enrich the residual melt in ferric iron, increasing the melt's intrinsic fO_2. Dynamically changing magmatic oxygen fugacities profoundly affect the stability liquidus silicate phases in addition to potential sulfide phases involved in ore forming processes.

TABLE OF CONTENTS

LIST OF FIGURES

LIST OF TABLES

ACKNOWLEDGEMENTS

I would first like to thank all of the members of my committee for their time, support, and assistance with a multitude of issues and tasks during my time at UNLV. I would like to especially thank my advisor Adam Simon for all of the thoughtful advice that he has given me on both scientific and professional matters over the last four years. I also am deeply appreciative of his generous financial support that allowed me to attend multiple Goldschmidt and AGU conferences. Adam and his wife Alicia's willingness to open their home for many dinner parties for his students and visiting seminar speakers was especially enjoyable, and always a welcome diversion.

I must also thank Chris Heinrich and the other members of his isotope group at ETH in Zurich, Switzerland for granting me access to LA-ICP-MS facility. The friendly ETH group made multiple trips across the Atlantic a thoroughly enjoyable cultural experience (complete with fondue, trips to the Alps, and Swiss beer). Marcel Guillong is also thanked for assisting with LA-ICP-MS analyses, data reduction, as well as stringently inspecting all of data that left Zurich and eventually found its way into this dissertation. Ed Mathez, Thomas Pettke, and Chusi Li, and Ed Ripley are all thanked for providing constructive reviews of some of the material that was submitted as manusctipts; these reviews greatly enhanced both stylistically and substantively the manuscripts that comprise this document. James Webster of the American Museum of Natural History is thanked for performing three experiments in his IHPV apparatus; data from these experiments were invaluable in the completion of the final chapter. Oliver Tschauner is thanked for providing me with much enlightening discussion about

the interpretation experimental results, along with unique insight and perspectives on the behavior of crystalline material and silicate liquids.

Sean Mulcahy is thanked for his seemingly endless capacity to indulge me in discussing all aspects of electron microprobe analyses. I owe a debt of gratitude of Jim Norton and Amo Sanchez of the HiPSEC machine shop for great deal of assistance with experimental equipment, ranging from re-machining parts to modifying blueprints. Many friends and colleagues in the UNLV geosciences department are also thanked for the copious fun times and many parties that were much needed diversions from work! Finally, I must thank Meghan Magill for her understanding and unwavering support for the past four years particularly when I was either traveling or mentally unavailable.

This work was supported primarily by National Science Foundation grant EAR 0609550, and additional funding from the UNLV High Pressure Science and Engineering Center (HiPSEC) via the U.S. Department of Energy Cooperative Agreement Nos. DE-FC08-01NV14049 and DE-FC8806NA27684. Additional support from the Society of Economic Geology, Geological Association of Canada/Mineralogical Association of Canada, the UNLV Department of Geoscience and the UNLV Graduate and Professional Student Association was provided for travel and consumable materials.

CHAPTER ONE

DISSERTATION OVERVIEW

Fundamental Dissertation Objectives

The formation of magmatic-hydrothermal ore deposits is intimately related to fundamental magmatic differentiation processes such as crystal fractionation of oxide, sulfide, and silicate phases or the exsolution of magmatic volatile phase(s), and auto-oxidation processes. The collective effects of magmatic oxygen fugacity (fO_2), sulfur fugacity (fS_2), melt alkalinity, and the chemical identity of dissolved volatile phases ultimately define the volatility of a given metal species dissolved in a silicate liquid. As such, the ore forming potential of a given magmatic systems is fundamentally related to all of these variables. Despite these generalizations, many aspects of the distillation process that amplifies (often by orders of magnitude) the naturally diffuse ore-metal concentrations remain controversial and poorly understood.

Detailed experimental investigations of the solubility and partitioning behavior of ore metals are required in order to construct quantitative models that will ultimately predict the behavior and evolution of ore metal concentration in natural magmas. In the spirit of producing experimental data to be applied to this end, this study broadly examines the effects of fO_2, fS_2, variable magmatic phase assemblages, and chloride bearing aqueous fluids on ore-metal behavior in synthetic magmatic systems.

The Application of Novel Analytical Techniques

To Established Problems

Much of the novelty and utility of this experimental work lies in the application of

state of the art laser ablation inductively coupled plasma mass spectrometry (LA-ICP-MS) in quantifying the extremely low noble metal content of the quenched experimental melts and crystalline material. This analytical method provides distinct advantages over the bulk and micro-analytical methods employed in previous studies of the behavior of noble metals in silicate liquids. The high degree of spatial resolution and low limits of detection inherent to the technique offer unique insight to subtle variation in noble metal concentration as a function of the depth of the ablation crater as well as allowing the analyst to discriminate between equilibrium metallic alloy or sulfide phases and pristine quenched melt.

With application of this technique, the origin and consequences of the widely recognized "nano-nugget" problem have been explored. The nanonugget effect has significantly hampered the interpretations noble metal solubility and speciation in previous experimental studies. Chapter three of this study specifically addresses the long standing controversy revolving around cryptic nanonugget-bearing LA-ICP-MS signals. A detailed examination of the LA-ICP-MS signals from the basaltic melts in chapter three reveals that subtly heterogeneous LA-ICP-MS count rates may be related to the application of the analytical technique, and as such do not represent nano-scale, zero valence metal particles.

Summary of Salient Results

The sum of the experimental metal solubility results indicate that Au concentrations do not exceed 2 µg g-1 for hydrous basaltic liquids and 0.65 µg g^{-1} for haplogranitic liquids. Pt solubility does not exceed 1.2 µg g^{-1} in haplogranite melts, and appears to be

a function of the activity of Pt in the experimental system. Maximum Pd solubility in the haplogranite liquid was 0.33 μg g^{-1}; these low values reflect the low Pd activity in the in the sulfide phase assemblages. All Au solubility values reported in this work represent Au behavior in systems where Au activity is fixed at unity. Thus, these values represent the maximum attainable Au concentrations in natural silicate liquids at similar P-T-X conditions. Viewing these solubility values as a limiting case, the noble metal budgets of silicate melts in equilibrium with low activity values of these metals in common magmatic sulfides should be vanishingly small.

Experimental results detailed in chapter three call into question some long standing assumptions about the speciation of Au in basaltic melts. Potential Au species other than $AuO_{0.5}$ may nullify increasing Au concentrations as a function increased fO_2 values in the manner indicated by simple silicate melt-metallic Au equilibria. Further spectroscopic work is required to unequivocally demonstrate the specific speciation of Au in volatile bearing melts. This future work remains difficult, if not impossible, with current spectroscopic techniques considering the meager Au concentrations (< 2.0 μg g^{-1}) in the experimental melts.

The redox and phase equilibria consequences and ferrous iron solubility in chloride-bearing magmatic volatile phase(s) is addressed in chapter four. Evolving olivine compositions and phase assemblages in experiments equilibrated with supercritical NaCl-KCl-HCl fluids indicate that FeO activity in the melt is buffered by the aqueous phase. The preferential leaching of FeO alters the $Fe^{3+}/\sum Fe$ of the residual as well as the fO_2 defined by the homogeneous ferric-ferrous equilibria of the melt. Chloride

degassing may be an alternative, albeit non-mutually exclusive, mechanism by which magmatic fO_2 is altered.

Submission of Individual Chapters As Manuscripts for Publication

Each individual chapter of this document was written as a manuscript intended for publication in a scientific journal. Brief summaries and descriptions of the original manuscripts serving as chapters are detailed in following sections along with the co-authors and the submission/publication dates.

Chapter Two Synopsis

Chapter Two presents the results of an experimental study of Au, Pt, and Pd partitioning in a water-saturated haplogranite, sulfide, and oxide phase assemblage. This chapter examines the effect of sulfur fugacity on the fractionation of Au, Pt, and Pd in a haplogranite melt, sulfide, oxide, aqueous fluid phase assemblage. This chapter comprises a manuscript that was submitted and published in Geochimica et Cosmochimica Acta in October 2009. Experiments and all electron microprobe analyses in this study were performed at UNLV. LA-ICP-MS data was collected at the Institute for Isotope Geology at ETH in Zurich Switzerland in the laboratory of Dr. Christoph Heinrich. Collection and reduction of the data was assisted by Dr. Marcel Guillong of ETH; Dr. Adam Simon assisted with equipment in the experimental laboratory as well as the interpretation of the LA-ICP-MS data for the sulfides and quenched melts. Both contributors appear as co-authors on the final publication.

Data from this chapter indicate that increasing sulfur fugacity does not enhance Au, Pt, or Pd solubility in the melt; however high sulfur fugacity values do significantly influence Pt and Pd compatibility as lattice bound constituents of monosulfide solid solution. Working in concert, magmatic sulfur and oxygen fugacity values determine the stable sulfide phase assemblage. In this way, the Au, Pt, and Pd contents of the residual silicate melt in equilibrium with a sulfide phase assemblage are critically dependent upon the identity and abundance of the stable sulfide phases. The fractionation effect of magmatic sulfides ascertained from these experiments appears produce a fractionation trend inverse to the Pt-Pd ratios observed in PGE rich porphyry ore deposits.

Chapter Three Synopsis

The source of chapter three comprises a manuscript submitted to Geochemica et Cosmochimica Acta in March 2010. This manuscript outlines the experimental determination of Au solubility in hydrous, chlorine bearing basaltic melts and olivine at variable oxygen fugacity. Experimental work presented in this chapter was performed was primarily performed at UNLV with some exploratory experiments performed at the California Institute of Technology. LA-ICP-MS analyses of the experiments were performed at the Institute for Isotope Geology at ETH in Zurich, Switzerland in the laboratory of Dr. Christoph Heinrich. Dr. Marcel Guillong of ETH assisted with the LA-ICP-MS analyses and interpretation of the resultant data. Dr. Adam Simon assisted in the preparation of the experiments as well as the interpretation of the resultant EPMA

and LA-ICP-MS data. For these contributions, both appear as co-authors on the submitted manuscript.

Results from this chapter indicate that fO_2 may not be the sole variable dictating the absolute magnitude of noble metal solubility in silicate liquids containing appreciable quantities of dissolved chlorine and sulfur. As such the metallic Au precipitation is a subtle function of fO_2, although not in the manner expected if Au were dissolved solely as an oxide species. Thus, the data from this chapter suggest that the assumption of $AuO_{0.5}$ as the preeminent Au species may not be warranted for volatile bearing silicate melts at low oxygen fugacity. Data from the study also suggest that Au behaves as an incompatible element with respect to olivine and clinopyroxene. Noble metal solubility values for the basaltic liquids examined in this study place an upper constraint on the metal budgets of natural magmas. As no natural silicate magmas have been reported to be saturated with metallic Au, Pt, or Pd phase(s), experimental data from these studies place a strict upper limit on the range of possible Au concentrations in natural silicate magmas. These data also impose a limit on the maximum possible proliferation of Au concentration in silicate liquids of no more than a 2 $\mu g\ g^{-1}$ during the fractionation of common silicate and oxide phases.

Chapter Four Synopsis

The material contained in Chapter Four comprises a manuscript submitted to the Journal of Geology for publication in March, 2010. This final chapter of the dissertation presents experimental work regarding the preferential scavenging of ferrous iron from silicate liquids by chloride bearing aqueous fluids. Experiments from this chapter were

performed at UNLV, as well as three that were performed at the American Museum of Natural History. All electron microprobe analyses were performed at UNLV. Dr. Adam Simon assisted in the preparation of the experiments. LA-ICP-MS analyses were performed at Institute for Isotope Geology at ETH in Zurich Switzerland in the laboratory of Dr. Christoph Heinrich. Dr. Marcel Guillong of ETH assisted with the LA-ICP-MS analyses as well as the interpretation and reduction of the data. Both contributors appear as co-authors on the manuscript.

Data from this chapter suggest the oxidizing effects of HCl bearing fluids may act in an auxiliary capacity with degassing H_2S to dynamically change magmatic fO_2 values. The oxidizing effects of these fluids have potentially important implications for the stability of redox sensitive phase assemblages (e.g., magmatic sulfides) in degassing magmas.

CHAPTER TWO

EXPERIMENTAL CONSTRAINTS ON Pt, Pd AND Au PARTITIONING AND FRACTIONATION IN SILICATE MELT–SULFIDE–OXIDE–AQUEOUS FLUID SYSTEMS AT 800°C, 150 MPa AND VARIABLE SULFUR FUGACITY

Abstract

We have performed experiments to constrain the effect of sulfur fugacity (fS2) and sulfide saturation on the fractionation and partitioning behavior of Pt, Pd and Au in a silicate melt–sulfide crystal/melt–oxide–supercritical aqueous fluid phase–Pt–Pd–Au system. Experiments were performed at 800° C, 150 MPa, with oxygen fugacity (fO_2) fixed at approximately the nickel–nickel oxide buffer (NNO). Sulfur fugacity in the experiments was varied five orders of magnitude from approximately log $fS_2 = 0$ to log $fS_2 = -5$ by using two different sulfide phase assemblages. Assemblage one consisted initially of chalcopyrite plus pyrrhotite and assemblage two was loaded with chalcopyrite plus bornite. At run conditions pyrrhotite transformed compositionally to monosulfide solid solution (mss), chalcopyrite to intermediate solid solution (iss) and in assemblage two, chalcopyrite and bornite formed a sulfide melt. Run-product silicate glass (i.e., quenched silicate melt) and crystalline materials were analyzed by using both electron probe microanalysis and laser ablation inductively coupled plasma mass spectrometry. The measured concentrations of Pt, Pd and Au in quenched silicate melt in runs with log fS_2 values ranging from approximately 0.0 to -5.0 do not exhibit any apparent dependence on fS_2. The measured Pt, Pd and Au concentrations in mss do vary as a function of fS_2. The measured Pt, Pd and Au concentrations in iss do not appear dependent on fS_2. The data suggest that fS_2, working in concert with fO_2, via the

determinant role that these variables play in controlling the magmatic sulfide phase assemblage and the solubility of Pt, Pd and Au as lattice bound components in magmatic sulfide phases, is a controlling factor on the budgets of Pt, Pd and Au during the evolution of magmatic systems.

Introduction

Quantitative constraints on the geochemical behavior of precious and base metals in silicate melt–aqueous volatile phase(s) systems are intrinsically valuable in elucidating the redistribution of metallic, siderophile and chalcophile elements during the evolution of ore-forming magmatic systems. Metallically fertile magmas are a necessary, albeit not sufficient, condition for the formation of magmatic ore deposits. Magmatic differentiation processes play the critically instrumental role in amplifying, by orders of magnitude, the low abundance of most ore metals in crustal reservoirs (cf., Rudnick and Gao, 2003) to ore-grade concentrations. Understanding the character of these processes is critical to the development of predictive models for ore deposit formation. The partitioning of the platinum group elements (PGE) and base metals has been investigated in natural and experimental assemblages in broadly mafic systems, defined as silicate melt coexisting with immiscible Fe–Ni–sulfide melt and/or crystals. Such studies have yielded both empirically estimated and experimentally determined partition coefficient values for the PGE and other metals between co-existing sulfide crystals and/or liquid and silicate liquid, defined as $D_{PGE}^{sul/sil}$. Published $D_{PGE}^{sul/sil}$ values for the entire group of platinoids range from 10^3 to 10^5 (Fleet et al., 1991, Peach et al., 1990 and Stone et al., 1990; Peach et al., 1994; Fleet et al., 1999), consistent with the

long recognized enrichment and association of the PGE with sulfide phases in layered-mafic-intrusion-hosted PGE–Ni–Cu deposits. Significant effort, and concomitant controversy, has been aimed at quantifying the solubility and oxidation state of many noble and base metals in silicate melts. Experimental studies aimed at elucidating noble metal solubilities in Fe-free, mafic-analog silicate melts have demonstrated consistently that PGE concentrations at metal saturation vary proportionally with the oxygen fugacity (fO_2) imposed upon the system (Ertel et al., 1999). Laboratory studies have demonstrated that Pt solubility in melts ranging from basalt to rhyolite, excluding high Ca melts, is less than 1 μg g^{-1} at redox conditions (log fO_2 NNO) approximating those present in most natural magmatic systems (Borisov and Palme, 1997, Farges et al., 1999, Ertel et al., 1999 and Blaine et al., 2005). In addition to the dependence of PGE solubility on fO_2, it is likely that PGE solubilities are dependent on sulfur fugacity (fS_2). Jugo et al. (1999) hypothesized that fS_2 is important in controlling the solubility of Cu and Au in sulfide phases during the evolution of magmatic systems. While their experimental study was performed at a single fO_2 (NNO + 0.5) and fS_2 (log $fS_2 = -1$) condition, they hypothesized that fS_2 may control the partitioning of Au between silicate melt and sulfide, in this case pyrrhotite (po), by one possible equilibrium such as

Eq. 1 $$\mu^{melt}_{AuO_{0.5}} + \mu^{po}_{FeS} + \tfrac{1}{2}\mu^{sys}_{S_2} = \mu^{po}_{AuFeS_2} + \tfrac{1}{4}\mu^{sys}_{O_2} + \mu_{Fe_3O_4}$$

where μ_i^j is the chemical potential of component *i* in phase *j*. Equation 1 suggests that variation in fS_2 and fO_2, owing to processes such assimilation of country rock (i.e. introduction of reduced and/or oxidized sulfur) and degassing, and associated auto-oxidation of the magma (cf., Candela, 1991), may play a determining role in the metal enrichment process of the evolving magmatic system. For example, assimilation of

reduced country rock will drive the magma toward lower fS_2; hence favoring the mass transfer of ore metals from the silicate melt into sulfide (e.g., Au into sulfide as written in Eq. 1). Fractionation and subsequent removal of sulfide phases at depth during ascent of the magma will reduce the potential for metals to be later scavenged and redistributed by magma-evolved aqueous fluids. In this study we investigated the role of fS_2 on the solubilities of Pt, Pd, Au and Cu in an H_2O-saturated rhyolite silicate melt, sulfide and oxide phase system at 800 °C and 150 MPa. Sulfur fugacity was controlled by using different sulfide phase assemblages to impose fS_2 that span the range of fS_2 values found in many natural systems. The results demonstrate that changes in fS_2 of an evolving sulfide-saturated magma shift the stable phase assemblage to an assemblage with a different capacity to sequester metals. Such chemical changes affect the inherently finite metal budget of the system and have important consequences for the metals available for transport during sulfide fractionation and/or magmatic degassing at the level of ore deposit formation.

Procedures

Starting Materials

Starting materials utilized in this study were a synthetic Corning haplogranite glass (provided by Dr. David London, University of Oklahoma), natural hexagonal pyrrhotite (po), bornite (bn), and chalcopyrite (ccp; provided by Dr. George Harlow, American Museum of Natural History), Calumet magnetite (mt; Calumet Skarn, Colorado), and 10 wt.% NaCl eq. NaCl–KCl ± HCl aqueous solutions. The composition of the starting rhyolite glass is provided in Table 1. The starting sulfide phases and mt were

characterized by using electron probe microanalysis (EPMA) for major and most of the minor elements and laser ablation inductively coupled plasma mass spectrometry (LA-ICP-MS) for Pt, Pd and Au. The concentration of these elements is less than 1 μg g^{-1} in all phases. Small aliquots of Pt and Pd metal foil were added to serve as the Pt and Pd metal sources. Phase relations for the NaCl–KCl–H_2O system indicate that the aqueous fluid at run conditions exists as a one-phase supercritical aqueous fluid (Bodnar et al., 1985 and Chou et al., 1992).

Experimental Design

Experiments were performed at 800 °C and 150 MPa in René-41 cold seal pressure vessels. Rhyolite glass, sulfide phases, mt and aqueous solution were loaded (Table 2) into Au capsules (5 mm OD × 2.5 cm length with a 0.2 mm wall thickness) and sealed with a carbon electrode arc welder. Three different assemblages were loaded as follows: Assemblage 1 initially contained cp + po + mt + glass + aqueous fluid, the latter had an initial ratio of NaCl–KCl–HCl of unity. Assemblage 2 contained cp + po + mt + glass + aqueous fluid, the latter had an initial NaCl–KCl ratio of unity and no HCl. Assemblage 3 contained cp + bn + mt + glass + aqueous fluid, the latter had an initial ratio of NaCl–KCl–HCl of unity. At run conditions cp and po in assemblages 1 and 2 transformed to iss and mss; assemblage 3 is interpreted to have contained a sulfide liquid formed from the reaction of bn and cp. Table 2 provides the details of each assemblage. Water was used as the pressure medium. The fO_2 of each experiment was buffered at approximately Ni–NiO by relying on the intrinsic buffering capacity of the René-41 pressure vessels (cf., Chou, 1987). The fO_2 buffering capacity of the vessel has been evaluated by using external Au capsules loaded with Ni and NiO

to verify the stability of both phases over run times exceeding 1000 h. Temperature was monitored with factory-calibrated Omega type K (Chromel–Alumel) thermocouples. Run pressure was monitored with a bourdon tube pressure gauge which was calibrated against a factory-calibrated Heise gauge. Thermal gradients in the pressure vessels are 5–7 °C over the length of the experimental capsule. Experimental run duration was varied from 67 to 672 hrs; run times are provided in Table 3. Experiments were terminated by a nearly isobaric quench in a stream of compressed air from 800 to 200 °C and then immersed in an ambient temperature water bath. Capsules were removed from the vessels, cleaned with lab-grade H_2O, examined optically and weighed to determine if the capsules remained sealed during the experiment. Only capsules that exhibited mechanical integrity, evinced a mass change of ≤0.3 mg, and yielded a strong hiss when pierced with a hypodermic syringe, evincing high internal capsule pressure, were processed for analysis.

Sulfur and Oxygen Fugacity

Two different starting sulfide phase assemblages were used in an attempt to control fS_2 at a fixed fO_2. The starting sulfide assemblages were po plus cp in assemblages 1 and 2, and cp + bn in assemblage 3. Despite the interdependent nature of the equilibria controlling fO_2 and fS_2, it is routinely assumed that the vastly greater buffering capacity of the Ni-rich pressure vessel fixes the fO_2 (cf. Chou, 1987) of the experimental assemblage via the equilibrium, in the case of po and mt,

Eq. 2 $$6FeS^{po} + 4O_2^{sys} = 2Fe_3O_4^{mt} + 3S_2^{mvp}$$

In the absence of large quantities of sulfide, the fO_2 imposed by the vessel in conjunction with the water pressure medium will fix the fH_2 imposed on the

experimental system, thus the vessel-controlled fH_2 imposed on the experimental system controls fS_2 via the equilibrium in Eq. (2). As a consequence of fixing fH_2 and fS_2, the fH_2S of the experimental system must also be fixed by the equilibrium:

Eq. 3 $$H_2 + \tfrac{1}{2}S_2 = H_2S$$

We hypothesize that the progressive sulfidation of the Pt metal chip, added as the Pt source, dynamically removed sulfur from the magmatic volatile phase (mvp) over the course of the run via the equilibrium:

Eq. 4 $$Pt^o + \tfrac{1}{2}S_2^{mvp} = PtS$$

EPMA-analysis of the Pt chips recovered from runs of different durations indicates that a sulfidation front propagated toward the center of the Pt chip. The sulfidation front was observed as a rind of PtS which thickens progressively with increasing run time. The subtly changing experimental fS_2 conditions are reflected compositionally in the dissolved sulfur content of the quenched silicate melt and also the metal content of the recovered mss. In light of the relatively small range in fS_2 values for a given assemblage, with respect to the long experimental run durations (a maximum difference of ~1.0 log unit for run durations in excess of 600 hours is observed), we postulate that the composition of the experimental run products represents a steady state (on the time scale of 2–3 days) or perhaps an equilibrium state, reflective of the "instantaneous" fS_2 of the system. Thus, the quenched-in compositions of the experimental run products represent a snapshot of a system continuously evolving toward its final equilibrium fS_2 condition defined by the Pt–PtS buffer. The sluggish decline in fS_2values (approximately 0.04 log units day^{-1}) coupled with the relatively

high reactivity of the sulfide and silicate melt phases as observed in other studies at similar *P–T* conditions (e.g.,Ballhaus and Ulmer, 1995; Clemente et al., 2004) suggests that the fS_2 of the system at the time of the termination of the run, is accurately reflected in the run products (i.e., the run products closely maintained an equilibrium relationship with system fS_2 as this parameter slowly changed). While the experiments did not reach a final "equilibrium" sulfidation state, the relative differences in the experimental partitioning behavior for Pt, Pd, Cu and Au place important constraints on the geochemical behavior of these metals in magmatic-hydrothermal systems.

Analytical Procedures

EPMA Analysis

Recovered glass (i.e., quenched melt) and sulfides were analyzed by using wavelength dispersive spectrometry (WDS) with a JEOL® JXA-8900 SuperProbe at the University of Nevada, Las Vegas. Glasses were analyzed for major elements using a 15 kV accelerating voltage and a 5 nA Faraday cage current. A 10 μm de-focused beam was used in conjunction with the low beam current in order to minimize current–flux–density-induced alkali diffusion (cf., Morgan and London, 1996). The concentration of *S* in the quenched glasses was quantified by using a 10 μm diameter beam and a 50 nA Faraday cage current with counting times of 90 s on peak and 90 s on the background. The position of the S Kα peak was determined with a PET spectrometer for individual aliquots of experimental glass by using a statistical, automated peak search function in the JEOL® software. Natural ZnS was used as a standard for the *S* analysis. The applied ZAF matrix correction procedure for the S analyses employed the averaged

major element composition of the glass as determined by the previously described analytical conditions. Calculated analysis-specific 3σ limits of detection (LOD) for *S* in the glasses range from 60 to 70 μg g^{-1} for the entire suite of analyses. The low concentration of *S* in the experimental glasses prevented us from using the peak shift in the *S* Kα radiation, determined by EPMA, to estimate the proportion of sulfide to sulfate species dissolved in the glass. However, considering the relatively low oxidation state of the runs (≈NNO), we estimate that greater than 95% of the sulfur present in the melt is dissolved as the reduced species S^{2-} (Carroll and Rutherford, 1988). Secondary standards VG-A99 and VG-2 were analyzed to evaluate the performance of the *S* analytical routine. Using our analytical routine, the concentration of *S* in standard glasses VG-2 and VG-A99 were quantified at 1300 ± 44 and 155 ± 9 μg g^{-1}, respectively. Previous studies that used EPMA to quantify the *S* content of VG-2 report 1403 ± 44 μg g^{-1} (O'Neill and Mavrogenes, 2002) and 1340 ± 80 μg g^{-1} (Dixon et al., 1991). The concentration of *S* in VG-2 has been reported as 1320 ± 50 μg g^{-1} ,when quantified by wet chemical methods (Wallace and Carmichael, 1992). The *S* content of VG-A99 as determined by EPMA has been reported as 138 ± 13 μg g^{-1} (Witter et al., 2005) and 170 ± 80 μg g^{-1} (Dixon et al., 1991). The agreement between our EPMA-determined S values and extant literature values suggests that the S concentrations reported herein are accurate. Recovered Cu–Fe sulfide crystals were analyzed by using a 30 kV accelerating voltage and a 30 nA beam current. Iron, S, Ni and Cu were quantified by using Kα X-ray emission lines, whereas Pt, Pd and Au were quantified by using Lα X-ray emission lines in order to mitigate spectral interferences observed in the M series lines for these latter elements. A beam diameter of 15 μm was used in order to

reintegrate the composition (presumably at run conditions) of the fine scale (<1 μm) exsolution features of the recovered sulfide material. Quenched sulfide melts were analyzed with a broad 40 μm beam to obtain the average composition of the sulfide melt at run conditions.

LA-ICP-MS-Analysis

LA-ICP-MS analyses were performed at the Institute for Isotopengeologie and Mineral Rohstoffe at ETH in Zürich, Switzerland by using a homogenized prototype Excimer ArF laser (λ = 193 nm) system, similar to the Geolas System, coupled with a Perkin-Elmer Elan 6100 DRC quadrupole ICP mass spectrometer. To improve the limits of detection for Pt, Pd and Au, a carrier gas mixture comprised of a helium (1.15 L/min) and hydrogen (6 ml/min) mixture was utilized (Guillong and Heinrich, 2007). The diameter of the ablation crater was varied from 90 μm for quenched glasses and mt to 30 μm for sulfide run products; ablations were carried out at an energy density of 25 J cm^{-1} and a repetition rate of 10 Hz for silicate glasses and mt. To improve the transient signal from the sulfides, the energy density was decreased to 10 J cm^2 and 3 Hz repetition rate. NBS-610 was utilized as a standard reference material for all investigated phases. Additionally, a synthetic PGE-doped Cu–Fe sulfide standard (Wohlgemuth-Ueberwasser et al., 2007) was utilized for Pt and Pd in some sulfide phases. The polyatomic interference from $^{65}Cu^{40}Ar^+$ produced in the plasma on the isotope ^{105}Pd is problematic for the analysis of Pd in Cu rich phases (i.e., iss). The $^{65}Cu^{40}Ar^+$ species production rate was quantified by ablating 99.999% Cu and measuring the resultant count rates on mass 65 and 105; $CuAr^+$ interference was measured to be 0.05% of the counts measured on mass 65. Based on this, the raw counts

from ^{105}Pd can be corrected for interfering $^{65}Cu^{40}Ar^{+}$ species if necessary. The data indicate that the use of NBS-610 and the synthetic PGE sulfide standards to reduce and calculate Pd and Pt concentrations in sulfide phases yield statistically similar, albeit slightly different results. As discussed below, both the EPMA- and LA-ICP-MS-determined concentrations of Pd and Pt are presented to allow a comparison of the use of the silicate glass standard (i.e., NBS-610) vs. the synthetic PGE-doped standard to quantify Pd, Pt and Au concentrations. Data processing and reduction of the raw LA-ICP-MS data were performed by using SILLS (Guillong et al., 2008) using EPMA-determined element concentrations as the internal standard. Aluminum was used as the internal standard for the silicate glass analyses. Iron was utilized as the internal standard for mt, mss and iss.

Results

Major Element and Chlorine Concentrations in the Silicate Glass

The silicate glass recovered from all runs is crystal free and homogenous within a given experiment with respect to the concentrations of Si, K, Na, Al and Cl (Table 3). The concentration of Fe exhibits slight variability; however, the range of Fe concentrations in silicate glass is consistent with that reported in previous experimental studies at similar conditions (e.g., Simon et al., 2008). The concentration of S in some recovered glasses exhibits slight heterogeneity; these values are attributed to uncertainty associated with analyzing low sulfur concentrations that are near the detection limit. EPMA data indicate that all glasses are slightly peralkaline to peraluminous; the aluminum saturation index (ASI), the ratio of Al/Na + K, ranges from 0.97 to 1.14. The

solubility of water in the melt, estimated by using the EPMA difference method, ranges from 7 to 8.5 wt.%. This estimate is consistent with the expected water solubility of 6–8 wt.% in rhyolite melt at 800 °C and 150 MPa (McMillan and Holloway, 1987).

Cu, Au, Pt and Pd Concentrations in the Silicate Glass

The major and trace element concentrations including Cu, Au, Pt and Pd in the recovered silicate glasses are provided in Table 3. The concentration of Cu in silicate glass ranges from 5 to 22 μg g^{-1} and is homogeneously distributed within glass beads recovered from all runs. These values are consistent with the published Cu concentrations of 4 μg g^{-1} (Lynton et al., 1993), 26 μg g^{-1} (Jugo et al., 1999) and 1 μg g^{-1} (Simon et al., 2006) for similar bulk assemblages at similar experimental conditions. In this study, melts reacted with low sulfidation Cu-rich phase assemblages have the highest Cu concentrations, whereas high sulfidation Cu-poor phase assemblages generally yield lower Cu concentrations in rhyolite melt. The quantification of the concentrations of Au, Pt and Pd in recovered silicate glass is complicated owing to the observed heterogeneous distribution of these metals in glass (Fig. 1a and b). Several previous studies have discussed the inherent difficulty in quantifying the solubility of noble metals in quenched silicate melts with oxidation states lower than the mt–hematite buffer. The LA-ICP-MS spectra from ablation of silicate glasses are routinely complicated by the presence of spatially heterogeneous distributions of some metals (e.g., Ag; Simon et al., 2008). This so called “nano-nugget effect” (cf., Borisov and Palme, 1997, Simon et al., 2007 and Ertel et al., 1999), as observed in LA-ICP-MS spectra has been interpreted previously as either a quench-exsolution phenomenon (e.g., Cottrell and Walker, 2006) or as a product of redox reactions within the charge

(e.g., Ertel et al., 1999). Stable PtO species within the melt structure are reduced to elemental Pt in colloidal suspension within the melt (Ertel et al., 1999) as a function of the reduction of the experiment oxidation state during run up. Simon et al. (2008) suggest that initial noble metal solubilities in the melt are relatively high, approaching the 10 μg g^{-1} range, over the first 12–24 h of a run before the experimental charge comes to equilibrium with the intrinsic redox state of the pressure vessel; hence, an excess of Pt is initially dissolved in the melt. As the charge approaches osmotic redox equilibrium, the fO_2 of the metal-oversaturated melt decreases. During the period of reduction the melt gradually exsolves excess Pt, Pd and Au, forming nano-nuggets, until the melt fO_2 reaches the buffered value of [redacted]NNO. Ertel et al. (1999) demonstrated that during a period of fO_2 reduction, Pt and Rh solubilities decrease in the melt, causing the melt to exsolve the excess metals and forming nano-nuggets until the melt fO_2 reaches its final state. We specifically note the congruency of the Pd, Au and to a much lesser extent Cu in LA-ICP-MS signals from the nugget bearing analyses (Fig. 1a). Such signals have the appearance that the nugget-forming metals are either alloyed or enjoy an intimate, mechanical association. Only nugget free analyses of silicate glasses (Fig. 1b) have been considered in this study, as these LA-ICP-MS signals are assumed to approximate best the equilibrium solubility of the noble metals in the melt. The measured solubility of Au in silicate glass from individual runs and among runs in the present study is variable (Table 3). The data in the present study indicate that the best estimate for Au solubility in S-bearing rhyolite melt is on the order of a few tens to a few hundreds of ng/g (Table 3). Frank et al. (2002) reported that Au solubility at 800 °C and 100 MPa in a S-free Au-saturated rhyolite melt is 1 μg g^{-1}. As discussed

by Frank et al. (2002), it is possible that the quenched silicate glasses produced in their experiments contained submicroscopic gold particles or regions of increased Au concentration within the glass that formed during quenching. Frank et al. (2002) discussed the nugget effect, with specific reference to Instrumental Neutron Activation Analysis (INAA) and Secondary Ion Mass Spectrometry (SIMS), and concluded that the best estimate of Au solubility in S-free rhyolite melt was on the order of 1 μg g^{-1}. Simon et al. (2005) used nugget-free LA-ICP-MS analyses to quantify that the solubility of Au in S-free rhyolite is on the order of 500 ng/g. Jugo et al. (1999)reported Au solubility in S-bearing Au-saturated rhyolite melt, saturated with iss and po at 850 °C and 100 MPa, to be on the order of 2–4 μg g^{-1}. Simon et al. (2007) report that the solubility of Au in S-bearing rhyolite, equilibrated with arsenopyrite (FeAsS), is 0.6 μg g^{-1}. All of these experimental studies were conducted at broadly similar fS_2, fO_2, pressure and temperature conditions. We suggest that the higher reported Au solubility values may reflect the nature of the analytical technique. Jugo et al. (1999) and Frank et al. (2002) used the bulk analytical technique INAA which would incorporate Au nuggets and include them in the analytical totals. The solubilities of Au in assemblages 1, 2 and 3 are 0.26 ± 0.34, 0.11 ± 0.13 and 0.16 ± 0.03 μg g^{-1}, respectively; the average solubility is 0.18 ± 0.07 μg g^{-1}. As stated above, the uncertainties do not reflect the presence of nuggets in the integrated portion of the signal. In light of the aforementioned issues, we suggest that the data in the current study constrain the solubility of Au in S-bearing rhyolite melt, at the PTX conditions in this study, to no more than a few 100 ng/g, consistent with previous studies.

The concentrations of Pt and Pd in silicate glass are reported in Table 3. A systematic decrease in the abundances of Pt and Pd in the quenched melt occurs as a function of increasing run duration for each experimental assemblage (Fig. 2). Decreasing metal concentrations may be a function of the temporal evolution of the redox state of the system (initially) and/or by the additional possibility of decreasing the activities of the soluble metals or metal alloys in the experimental system via sulfidation and progressive alloying of elemental metallic species (i.e., the Pt and Pd metal chips used as the source of Pt and Pd). Platinum dissolution into the silicate melt structure may occur via the reaction proposed by Borisov and Palme (1997)

Eq. 5 $$Pt^{metallic} + \tfrac{1}{2}O_2^{system} = PtO^{melt}$$

with the corresponding equilibrium constant written as:

Eq. 6 $$K_3 = \frac{xPt^{metallic}\gamma Pt^{metallic}}{xPtO^{melt}\gamma PtO^{melt}} \cdot fO_2^{-\frac{1}{2}}$$

where x and γ are the mol fraction and activity coefficient, respectively. The numerator of the expression may be written as:

Eq. 7 $$xPt \cdot \gamma Pt = aPt$$

where a is the activity of Pt in Eq. (5). The solubility of Pt, as expressed in Eq. (4), is a function of the activity of Pt in the source phase, a_{Pt}^{source}, (i.e., native metal, metallic alloy, or sulfide) and the fO_2 imposed on the system. The choice of PtO as the stable Pt species in the melt is based on the strong positive correlation observed between Pt solubility and fO_2 reported by Ertel et al. (1999). Eq. (4) governs the solubility of Pt as a divalent oxide species within the silicate melt structure. The observed decrease in the measured abundances of Pt and Pd in the quenched glasses (Fig. 2) with increasing run

duration may reflect the decreasing activity of Pt and Pd in the experimental system as governed by the interaction of sulfur in the aqueous phase with alloys of the Pt and Pd foils via the following sulfidation reaction:

Eq. 8 $$x\mathrm{Pt}^{\mathrm{source}} + (1-x)\mathrm{Pd}^{\mathrm{source}} + \tfrac{1}{2}\mathrm{S}_2^{\mathrm{vapor}} = (\mathrm{Pt}_x\mathrm{Pd}_{1-x})\mathrm{S}$$

The activity of Pt in the system may be further decreased via the addition of Pd and Fe in solid solution on the PtS lattice. A similar relationship was also noted by Li et al. (2003) for Ni in*S* bearing magmas. The a_{Pt}^{source} is defined by the equilibrium expression in Eq. 9 where:

Eq. 9 $$a_{\mathrm{Pt}}^{\mathrm{source}} = \left(\frac{a_{(\mathrm{Pt,Pd})\mathrm{S}}}{(a_{\mathrm{Pd}}^{\mathrm{metal}})^{1-x} \cdot (f\mathrm{S}_2^{\mathrm{vapor}})^{1/2} \cdot \mathrm{K}_5} \right)^{1/x}$$

Substitution of the expression for Pt activity derived in Eq. (7) into the numerator of the equation governing Pt solubility as an oxide species (Eq. (4)) clearly shows that Pt solubility in the silicate melt phase in the investigated system is not only proportional to the oxygen fugacity of the system, but a complex function of the $f\mathrm{S}_2$ imposed on the experimental system and the composition of the phase acting as the Pt source to the melt. The a_{Pt}^{source}, as defined in Eq. (7), via progressive reaction of elemental Pt with Pd, *S* and Fe, will decrease until the composition of the Pt–Pd–Fe–S overgrowths on the Pt metal come to equilibrium with the system, only then will the a_{Pt}^{sys} be fixed. Thus, it is predicted that Pt solubility in the melt in sulfide–oxide–silicate melt systems should vary with changes in the $f\mathrm{O}_2$, $f\mathrm{S}_2$ and the a_{Pt}^{source} of the experimental system. Platinum solubility in the experimental system is thusly controlled by the variables $f\mathrm{S}_2$ and $f\mathrm{O}_2$ where a_{Pt}^{metal} of the source is a function of the $f\mathrm{S}_2$ imposed on the experimental system.

Monosulfide Solid Solution Composition

Recovered mss varies remarkably little in the *S* to Σ Fe–Pd–t–Au–Cu ratio within a set of analyses for multiple grains from individual experiments. Mss from nearly all runs contains measurable quantities of Ni, an element which is not present at measurable concentrations in any of the starting materials. Nickel may be introduced via the diffusion of Ni through the Au capsule from the pressure vessel via the water pressure medium and direct mechanical contact of po with the Au metal capsule as observed in previous experimental studies (Scaillet and MacDonald, 2001). The composition of mss is provided in Table 4. The solubility of Au in mss in the current study is of 170 ± 71 μg g^{-1}, similar to the value of 470 μg g^{-1} for Au solubility in mss reported by Jugo et al. (1999) at similar pressure–temperature-composition (PTX) conditions; log fS_2 values overlap statistically in both studies.

Ubiquitous exsolution features (Fig. 3) less than 1 μm in width were observed in most of the recovered mss crystals. Although the exsolution features were too small to be individually resolved quantitatively with EMPA-WDS or LA-ICP-MS, the exsolution features have been qualitatively characterized chemically by using energy dispersive X-ray spectrometry (EDS) and identified as predominately Pd–Cu–Ni-rich-sulfide relative to the host mss. Exsolution features observed in mss are likely the product of a relatively slow quench rate; i.e., 2 min. The solubilities of Pt and Pd in mss have been demonstrated to be a strong function of temperature (Ballhaus and Ulmer, 1995). The presence of quench-exsolution texture in our experimental mss is consistent with the down temperature decrease in Pt and Pd solubility observed by Ballhaus and Ulmer (1995). Mss at run conditions is expected to take on the hexagonal structure with

a fully disordered Fe sublattice; however, upon termination of the run, ordering of the vacancies on the Fe sublattice and eventual conversion or partial conversion to a monoclinic form, is speculatively responsible for the pervasive exsolution textures.

Integration of the composition of the exsolution features with the composition of the matrix mss is required to accurately quantify the concentration of these elements at run conditions. We used a 30 μm beam diameter for both EPMA and LA-ICP-MS analyses of mss. The data reported in Table 4 indicate that both methods effectively reintegrate the mss and exsolution lamellae and yield similar metal concentrations. The reported EPMA-determined concentrations of Fe and Cu suggest that both metals are homogenously distributed in the mss.

Intermediate Solid Solution Composition

Intermediate solid solution was observed in all run products; however, the iss observed in runs 32, 33 and 34 is inter-grown with bn and is thought to have exsolved from the sulfide melt, discussed below, during quench. Iss from these three runs is thus not reported as it was reintegrated into the sulfide melt composition. The measured compositions of iss reported in Table 5, is similar in all experiments. The composition of run product iss deviates significantly from the stoichiometry of the starting chalcopyrite. Total *S* content of recovered iss appears to vary little from the average value of ~35.0 wt.%. Platinum and Pd concentrations in iss were generally near or below the EPMA limit of detection, whereas Au concentrations within individual iss crystals in a given experiment exhibited variability. We hypothesize that the observed heterogeneity of Au within recovered iss is a quench phenomenon; i.e., the presence of Au lamellae in iss, observed by using back scattered electron (BSE) imaging, indicate

exsolution of Au during quench as reported by Jugo et al. (1999). The concentration of Au in run-product iss in the current study ranges from 0.37 to 0.72 wt.%, with an average on the order of 0.5 wt.%. This is similar, albeit lower than the experimentally determined value (±1σ) of 1.9 ± 0.4 wt.% for Au solubility in mss reported by Jugo et al. (1999).

Sulfide Melt Composition

The run products from charges loaded initially with cp and bn contain a single sulfide entity that we interpret to be a quenched sulfide liquid (Fig. 4). The sulfide entity encapsulates entire mt crystals and the boundary between the two appears to be a wetting surface. The EPMA-determined composition of the sulfide melt phase is provided in Table 6. This phase exhibits a complex intergrowth texture between Cu-rich and Fe-rich sulfide phases. The average composition provided in Table 6 reflects the inherent difficulty in reintegrating such a complex quench phase. Sulfide quench textures in our runs are consistent with the observed sulfide quench textures from other studies of sulfide melts (cf., Ripley et al., 2002). Recently revised phase relations for the Cu–Fe–S–O system from Tsujimura and Kitakaze (2004) place the melting temperature for the dry iss-bornite system at less than 800 °C, the temperature of experiments in the current study. Experiments in this study were performed at water-saturated conditions and the effect of fH_2O on sulfide melt–solid phase relations is unknown. We did not attempt to quantify the oxygen content of the sulfide melt phases owing to the relatively slow quench rate which likely promoted the extensive crystallization of the sulfide melt phase which renders it unlikely that the original oxygen content of the sulfide liquid was preserved.

Magnetite Composition

Magnetite was recovered in all successful experimental runs. The concentrations of all analyzed metals (Au, Cu, Pd and Pt) in mt are on the order of a few ng/g. EPMA analyses of run-product mt indicate that the final composition is near stiochiometric end-member mt.

Evaluation of Experimental Sulfur Fugacity

Sulfur fugacity was calculated by using the measured *S* solubilities of the recovered experimental glasses following Toulmin and Barton (1964) and the empirical model of Clemente et al. (2004). In the Clemente et al. (2004) model, fS_2 values are calculated relative to the metallic Fe-troilite sulfidation (FFS) buffer, utilizing an internally consistent fO_2 corresponding to NNO + 0 for all of the experimental runs. Eq. 10 was used to calculate fS_2 values:

Eq. 10 $$\Delta FFS = \frac{\log S(ppm) - 0.001T + 0.2567(\Delta NNO)}{0.1713 + 0.0034(\Delta NNO)}$$

where Δ FFS is the log fS_2 value defined relative to the FFS buffer. Sulfur fugacity was also calculated by using the $Fe_{(1-x)}S$ indicator method, formulated by Toulmin and Barton (1964) as:

Eq. 11 $$\log_{10} fS_2 = (70.03 - 85.83x)(1000/T - 1) + 39.30\sqrt{1 - .9989x} - 11.91$$

where *x* represents the mole fraction of the FeS component of mss. Palladium, Pt, Au, Cu and Ni have been assumed to substitute ideally for Fe in the mss lattice on a one to one basis (cf., Jugo et al., 1999). The effect of these metals on the mss solution behavior is assumed to be ideal given the low measured concentrations of these metals in mss.

Values for fS_2 calculated by both methods are reported in Table 7. The fS_2 values from experimental runs have been plotted relative to the liquid sulfur condensation curve, Pt–PtS buffer, and the metallic FFS buffer curve in Fig. 5. We suggest that the observed discrepancies between fS_2 values calculated from the two methods may reflect the kinetically sluggish nature of S dissolution into the melt (i.e., minor disequilibrium with respect to S solubility in the melt phase). Additionally, in runs 33 and 34, some individual EPMA analyses of *S* in the glass were at or below the detection limit. The average sulfur concentration for these runs included only values that were above the EPMA limit of detection; thus, it is likely that fS_2 values calculated from the EPMA averages for these runs are systematically biased toward higher values. We suggest that using the mss composition to calculate the fS_2 of a system is a more robust method than using the sulfur content of the silicate melt owing to the much higher degree of complexity in the solution behavior of the latter. Additionally the mss composition appears to be temporally more responsive to changing fS_2 conditions.

Sulfur fugacity values calculated from both methods appear to converge in experimental runs of intermediate duration. This reflects the attainment of a steady state with respect to both S solubility in the silicate melt and the metal composition of the recovered mss. We interpret this decrease in calculated fS_2 values to be a function of the progressive sulfidation of the Pt and Pd metal loaded initially as a metal source for the experiments. The reaction of the finite reservoir of sulfur within the experimental charge with the metal sources (i.e., the Pt and Pd foil chips) should result in depletion of the sulfur within the supercritical aqueous fluid phase with increasing progress of favorable Pt and Pd sulfidation reactions. Evidence for the progressive removal

of *S* from the supercritical aqueous fluid phase was observed in the form of the development of a PtS "rind" on the recovered pieces of Pt metal foil. Evidence for the removal of *S* from the supercritical aqueous fluid phase is also observed in the systematic decrease of the calculated fS_2 values for the runs. Analogous Cu–sulfide overgrowths have been observed encapsulating molten Cu metal blebs in a study of Cu solubility in mafic silicate melts (Holzheid and Lodders, 2001). The advancing sulfidation front (Fig. 6 and Fig. 7) is truncated at the interface with elemental Pt. This elemental Pt forms the core of the recovered foil chip. No elemental Pd was recovered in any of the runs indicating that all Pd present was either lattice bound in mss and Cu–Fe sulfide phases, alloyed with Au and Pt, or bound in separate, ubiquitous PdS phases.

Discussion

Fractionation of Pt, Pd and Au in Nature: The Effect of fO_2 and fS_2

The new data place constraints on the relative fractionation effects induced by the precipitation of mss, iss and sulfide–oxide melts on the abundances of Pt, Pd and Au in silicate magma. Silicate melts can reach sulfide saturation owing to magmatic fractionation or the addition of *S* sourced from outside of the magma (e.g., assimilation of biogenic pyrite from a sedimentary sequence). Both processes result in an increase in the aS_2 in the melt, hence promoting the saturation of the silicate melt with a sulfide phase. It is the fO_2–fS_2 condition at which sulfide saturation occurs that ultimately controls which sulfide phase will be stable (cf., Jugo et al., 1999), and how it will affect the Pd–Pt–Au budget of the evolving magmatic system prior to the exsolution of an

aqueous magmatic volatile phase. Here we discuss the effects of mss, iss and sulfide melt on modifying the metal budget of magmatic systems.

The Effect of mss Saturation

The data in this study suggest that saturation of a magmatic system with mss should strongly fractionate Pd from Pt, and both of these PGE from Au. In addition to fractionation effects, the ability for mss to scavenge Pt and Pd from a silicate melt is dependent upon the fS_2 of the system; i.e., higher fS_2 yields higher Pt and Pd solubilities in mss. This relationship is consistent with the results of Ballhaus and Ulmer (1995); however, the absolute concentrations of both Pt and Pd in mss in this study are lower than the values reported by Ballhaus and Ulmer (1994) for experiments performed at identical temperatures similar fS_2 values. Discrepancies between the solubility data in the two studies may be attributed to the more complex nature of the solid solutions utilized in the current study. Ballhaus and Ulmer (1994) equilibrated mss with either Pt or Pd, but never both simultaneously; additionally, their study did not include additional competing metals. The current study has utilized assemblages containing a more complex metal assemblage, thus, we hypothesize that more complex assemblages may be the cause of the variability in measured solubility values. The presence of Cu at several wt.% and Ni at slightly less than 1 wt.% may inhibit the solubility of Pt and Pd on the Fe sublattice of the mss lattice. Future work is planned to quantify the crystallographic residency of metals in mss solid solutions.

To calculate Nernst-type partition coefficients for Pt, Pd and Au between rhyolite melt and mss, taking into consideration the variation in values determined in this study, we used lower and upper values for each metal as a limiting case. Using a lower and

upper solubility value of 0.1 and 0.5 μg g^{-1} for Pt, Pd and Au in the rhyolite melt yields apparent Nernst-type partition coefficients that range from a low of $D_{Pd}^{mss/melt}$ = 4.4 × 10^4 to a high of = 2.2 × 10^5. Similarly for Pt, $D_{Pd}^{mss/melt}$ ranges from a low of 6 × 10^3 to a high of 3 × 10^4. These calculated $D_{Pt}^{mss/melt}$ values indicate that crystallization of mss leads to significant fractionation of Pt from Pd during silicate melt solidification. Thus, during mss fractionation, the absolute concentration of Pd in the silicate melt may decrease by a factor 10 relative to the concentration of Pt in the silicate melt. Gold is the most refractory of the three metals with measured concentrations in the silicate melt ranging from 0.35 to 0.01 μg g^{-1} with an average on the order of 0.1 μg g^{-1}. These Au solubility values yield a minimum $D_{Au}^{mss/melt}$ = 2.3 × $10^3$and a maximum $D_{Au}^{mss/melt}$ = 1 × 10^4. A comparison of these new results with those of Ballhaus and Ulmer (1994) suggests that the calculated partition coefficient values may increase with decreasing Cu content of the mss and additionally, increase with increasing fS_2 of the system.

The absolute magnitude of the depletion of Pt and Pd from the silicate melt phase ultimately depends on the fS_2 of the magmatic system, as the stability field for mss at magmatic conditions spans nearly 10 orders of magnitude. Thus, it is conceivable that a silicate melt could precipitate mss, yet retain significantly less Pt and Pd than are soluble in mss at much higher fS_2, significantly lowering the apparent partition coefficient values. Similarly, mss saturation may be inhibited entirely given the appropriate fO_2, fS_2, and fH_2O conditions. Hydrous silicate melts containing dissolved *S* at a fixed fO_2 and fH_2O posses a defined and fixed fH_2S, given the

appropriate low magmatic fO_2. Sulfidation reactions involving ferrous iron dissolved in the silicate melt or the transformation of mt to mss may be described by the following equilibria:

Eq. 13 $$FeO^{melt} + H_2S = FeS^{mss} + H_2O$$

Eq. 14 $$\tfrac{1}{3}Fe_3O_4 + H_2S = FeS^{mss} + H_2O + \tfrac{1}{6}O_2$$

Assuming the mss in Eqs. (8) and (9) and mt in Eq. (9) are pure phases, these reactions work in concert with the iron activity in the melt, fS_2 and fO_2 to buffer the fugacity of the gaseous species H_2S and H_2O in the melt.

Eq. 15 $$K_8 = \frac{fH_2O}{X_{FeO}^{melt} \cdot fH_2S} \cdot (\gamma_{FeO}^{melt})^{-1}$$

where X_{FeO}^{melt} is the mole fraction of dissolved FeO in the silicate melt, fH_2O is the fugacity of water, fH_2S is the fugacity of H_2S, and γ_{FeO}^{melt} is the activity of FeO in the melt. The fH_2O is related to fO_2 and fH_2S via the equilibrium:

Eq. 16 $$K_9 = \frac{fH_2O \cdot fO_2^{1/6}}{fH_2S}$$

If the intrinsic values of fH_2O and fH_2S fixed by the water content, sulfur content and oxidation state of the melt are out of equilibrium with the buffered values required by Eqs. (8) and (9), mss will be either resorbed and consumed until it is exhausted, or crystallize until the ratio of fH_2S and fH_2O of the silicate melt reach the equilibrium buffered values. Alternatively in sulfide unsaturated systems, high fH_2O values may impede entirely the crystallization of a sulfide phase given that the melt is sufficiently oxidized (i.e., at oxidation states where H_2S formation is limited, as reduced melts with high fH_2O will have a high propensity to crystallize an oxide phase). The

"instantaneous" water fugacity of the melt at any point during magmatic evolution (prior to vapor saturation by second boiling) exerts a first order control on the stability and modal abundance of crystalline mss present in the system. The reduction in a_{FeS}^{mss} by the incorporation of additional metal components (i.e., Cu, Ni and Co) into the mss lattice will shift the pure end member equilibrium dictated by Eqs. 8 and 9 in a direction that represses mt crystallization.

The model equilibria discussed above indicate that early saturation of a silicate melt with mss (given an appropriately high fS_2), provided that the mss is removed from the system via a Rayleigh type fraction process, may effectively reduce the PGE budget of the system levels that preclude the development of a PGE rich porphyry system. However, mss saturation at lowfS_2 values may be possible given a high a_{FeO}^{melt} and appropriate fO_2, fH_2O and fH_2S. Under such low fS_2 conditions, the ability of mss to deplete the melt of Pt and Pd should be drastically reduced relative to high fS_2 conditions. Additionally, at low fS_2 conditions conducive to the saturation of a magmatic sulfide phase the modal abundance of crystalline mss should be extremely low due to the low concentrations of S acting as a limiting reagent.

The Effect of iss Saturation

Crystallization of iss also appears to fractionate Pt, Pd and Au in the silicate melt. The effect of iss crystallization is to fractionate Au and Pd from Pt in the silicate melt with Pt being retained most strongly in the melt phase. Gold and Pd concentrations in iss range from 1000 to 5000 μg g^{-1}, whereas the concentration of Pt in iss is consistently below the EPMA limit of detection. It is interesting to note the similarity of the geochemical behavior of Pd and Au in iss when contrasted with the distinctly, dissimilar

behavior of these metals in recovered mss. There appears to be no systematic variation of the Pt, Pd or Au solubility in iss with variation in either fS_2 or the Fe/Cu ratio of the recovered iss. Gold concentrations reported in this study are similar to, albeit larger, than those reported in Simon et al. (2000). The fractionation trend of Pt and Pd, induced by the stability of magmatic iss, mirrors the mss fractionation trend where the concentration of Pt in the silicate melt exceeds that of Pd. The relatively compatible behavior of Au in iss differs distinctly from that observed in mss at the same experimental conditions. The compatible behavior of Au in the iss lattice should result in an inverse fractionation effect with respect to the ratio of Au to Pt and Pd in the residual silicate melt. Such a situation should strip Au from the melt relative to Pd and Pt.

Applications to Natural Systems

The observed fractionation trends induced by the crystallization of mss with respect to the metal content of the residual melt are not in agreement with the high Pt/Pd ratios observed in some porphyry ore systems (Auge et al., 2005). The discord between Pt/Pd ratios observed in PGE-rich porphyry ore deposits (Werle et al., 1984, Mutschler et al., 1985 and Hulbert et al., 1988, Mulja and Mitchell, 1991, Cassidy et al., 1996 and Ohnenstetter and Watkinson, 1998) and the Pt/Pd ratios caused by sulfide saturation, as constrained in this study, suggest that magma oxidation and subsequent sulfide resorption and/or chemical exchange of metallic species between crystalline magmatic sulfide material and an evolved aqueous magmatic fluid play dominant roles in the determination of the final Pt/Pd ratio of the ore system. Furthermore, sulfide

saturation early in the evolution of a rhyolite silicate magma and the subsequent removal of the sulfide phase via Rayleigh fractionation may reduce the concentrations of Pt and Pd in the silicate melt to levels too low for the PGE to be effectively scavenged and concentrated by a magmatic volatile phase in porphyry ore-forming systems.

Concluding Remarks

Our experimental results constrain fractionation trends amongst Pd, Pt and Au in rhyolite magmatic systems. The data suggest that the timing of sulfide saturation and the nature of magmatic sulfide phase stability may control the ultimate abundances and ratios of Pd, Pt and Au transported by magmatic hydrothermal fluids to porphyry-type ore forming systems. Early crystallization of a magmatic sulfide phase in an evolving rhyolite melt system (and the removal of this phase from further chemical interaction with the rest of the magmatic system) may effectively stifle volatile-phase transport of the PGE and their enrichment in the magmatic-hydrothermal environment with metal ratios consistent with those observed in nature. Magmatic sulfide phases may, however, play an important temporal role in liberating sequestered Pt and Pd via oxidation and resorbtion into the melt or via direct sulfide–aqueous fluid chemical interaction late in the magmatic-hydrothermal transition phase.

Table 1. Haplogranite Glass Composition; analyzed by ICP,EPMA and LA-ICP-MS.

Oxide Constituent	Wt %[1]
SiO_2	77.68
TiO_2	0.01
Al_2O_3	12.7
Fe_2O_3	0.28
Na_2O	4.49
K_2O	4.5
Total	99.66

Table 2. Summary of all experimental assemblages at run conditions. All starting solutions had a NaCl/KCl ratio of unity

Assemblage	Run Numbers	Phases At Run Conditions	NaCl/HCl[1]	P (MPa)	T (°C)	$\log_{10} fO_2$	$\log_{10} fS_2$[2]
One	12, 13, 15	iss + mss + mt + rhyolite melt + aqueous supercritical fluid + Pt + Pd + Au	1	150	800	~NNO	-0.19 (0.29)
Two	46, 47, 48, 49, 50	iss + mss + mt + rhyolite melt + aqueous supercritical fluid + Pt + Pd + Au	0	150	800	~NNO	-0.73 (0.11)
Three	32, 33, 34	Intergrown bn and iss + mt + rhyolite melt + aqueous supercritical fluid + Pt + Pd + Au	1	150	800	~NNO	-5.16 (NA)

1. This is the starting NaCl/HCl ratio of the aqueous fluid.
2. Nominal sulfur fugacity values are reported as averages calculated with the Toulmin and Barton (1964) algorithm with 1σ errors and should be considered estimates for a given set of experimental runs. See text in section 2.3 Sulfur and Oxygen fugacities for a discussion of calculation and interpretation of the experimental meaning of these values.

Table 3. The mean EPMA determined major element composition of quenched silicate melts.

Run	Duration	SiO_2	FeO	K_2O	Na_2O	Al_2O_3	Cl
Iss + po + magnetite + rhyolite melt + aqueous supercritical fluid + Pt + Pd + Au; no HCl added to starting solution							
12	69	71.11 (0.75)	0.67 (0.10)	5.26 (0.21)	3.04 (0.19)	11.71 (0.21)	0.2 (0.02)
13	167	70.87 (0.49)	0.55 (0.05)	4.96 (0.17)	2.99 (0.10)	11.69 (0.17)	0.15 (0.15)
15	360	71.89 (0.75)	0.73 (0.03)	5.32 (0.21)	3.13 (0.06)	11.65 (0.28)	0.2 (0.01)
Iss + po + magnetite + rhyolite melt + aqueous supercritical fluid + Pt + Pd + Au; Na/K/H of starting solution equals one							
46	160	70.45 (0.52)	0.90 (0.43)	5.90 (0.10)	3.17 (0.09)	11.54 (0.22)	0.18 (0.04)
47	336	71.55 (0.60)	0.94 (0.05)	5.83 (0.11)	2.99 (0.09)	11.29 (0.18)	0.18 (0.02)
48	483	70.78 (0.41)	0.96 (0.05)	5.9 (0.10)	3.06 (0.08)	11.67 (0.21)	0.21 (0.03)
49	607	72.68 (0.30)	0.59 (0.07)	5.42 (0.17)	2.85 (0.09)	11.10 (0.21)	0.13 (0.01)
50	672	72.34 (0.26)	0.71 (0.04)	5.63 (0.11)	2.92 (0.08)	11.28 (0.27)	0.15 (0.01)
Iss + bn + magnetite + rhyolite melt + aqueous supercritical fluid + Pt + Pd + Au							
32	140	71.08 (0.4)	0.52 (0.2)	5.89 (0.2)	2.93 (0.34)	11.51 (0.18)	0.14 (0.03)
33	231	72.46 (0.7)	0.34 (0.04)	5.68 (0.14)	2.57 (0.32)	11.26 (0.20)	0.09 (0.02)
34	281	71.09 (0.5)	1.91 (0.2)	5.49 (0.3)	2.99 (0.15)	10.55 (0.6)	0.18 (0.10)

All values reported are in Wt. % and the 1σ standard deviation is given in parentheses.

Table 4. Summay of the trace element concentrations, EPMA analytical total and calculated ASI values from the quenched silicate melts (continued from Table 3).

Run	Duration	S (µg/g)	Cu (µg/g)	Pt (µg/g)	Pd (µg/g)	Au (µg/g)	Total	ASI
Iss + po + magnetite + rhyolite melt + aqueous supercritical fluid + Pt + Pd + Au; no HCl added to starting solution								
12	69	152 (39)	8 (2)	1.2 (0.17)	0.34 (.31)	0.65 (0.49)	91.64	1.09
13	167	233 (48)	6 (1.4)	0.893 (0.03)	0.16 (.09)	0.038 (0.01)	91.53	1.14
15	360	245 (44)	13.6 (4)	0.266 (0.37)	0.21 (.22)	0.086 (0.04)	92.72	1.07
Iss + po + magnetite + rhyolite melt + aqueous supercritical fluid + Pt + Pd + Au; Na/K/H of starting solution equals one								
46	160	152 (49)	4.8 (0.89)	1.03 (0.15)	0.074 (0.05)	0.043 (0.02)	91.97	0.99
47	336	227 (49)	9.6 (2)	0.046 (0.03)	NA	0.35 (0.30)	91.88	1.01
48	483	184 (34)	6.7 (1)	0.17 (0.11)	0.046 (0.046)	0.100 (0.02)	91.98	1.02
49	607	153 (14)	4.8 (1.9)	0.01 (0.01)	0.033 (0.027)	0.06 (0.03)	92.69	1.05
50	672	143 (9)	5.2 (1.4)	0.027 (0.02)	0.010 (0.01)	0.019 (0.01)	92.83	1.05
Iss + bn + magnetite + rhyolite melt + aqueous supercritical fluid + Pt + Pd + Au								
32	140	151 (19)	13 (1.4)	1.1 (0.11)	0.02 (0.01)	0.14 (0.11)	91.77	1.03
33	231	83 (27)	NA	NA	NA	NA	91.52	1.09
34	281	74 (17)	22 (21)	0.6 (0.04)	0.027 (0.01)	0.18 (0.13)	91.62	0.97

1σ standard deviation is given in parentheses.

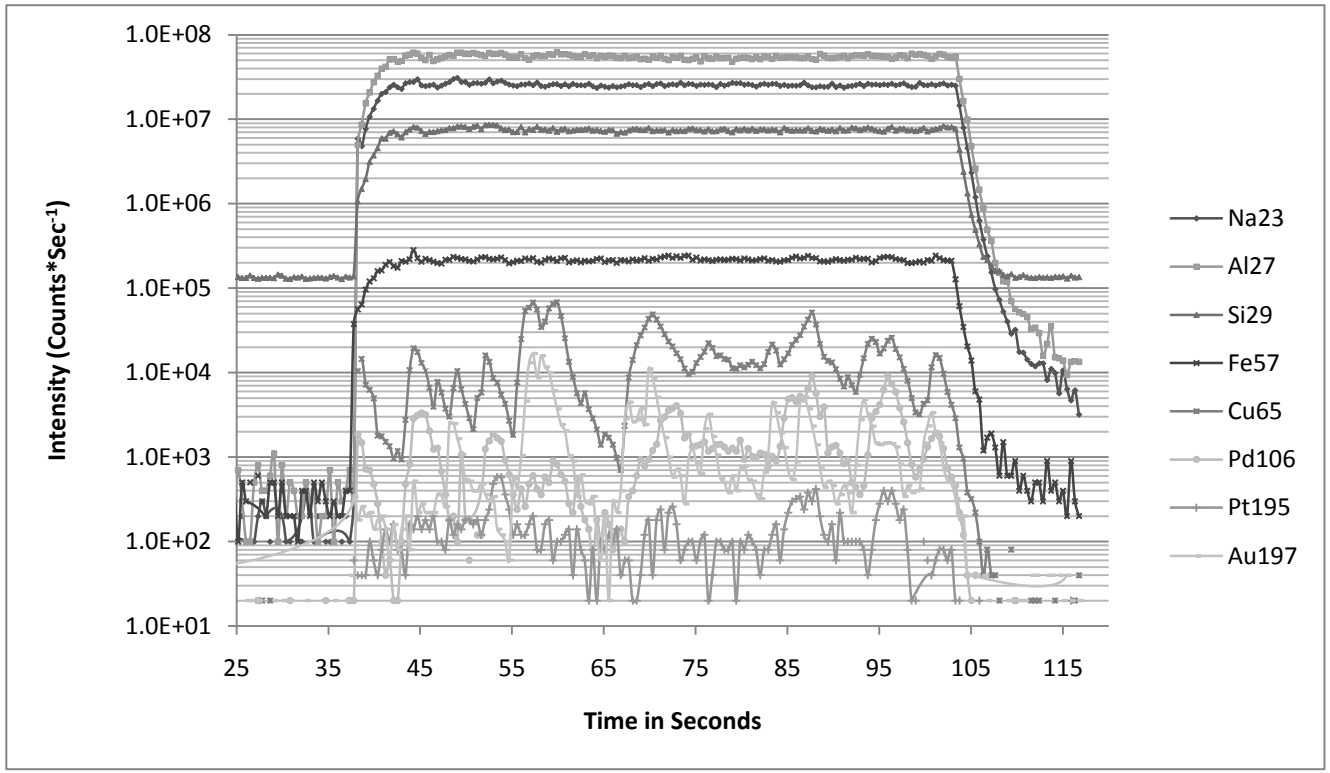

Figure 1 Nano-nugget bearing LA-ICP-MS signal from quenched silicate melt. Note the congruency of Cu, Au and Pd signals; additionally note the homogenous Fe signal. The homogenous nature of the Fe signal suggests that the nano- nuggets observed in the signal are not an artifact induced by small scale crystalline sulfide inclusions, but are in fact nano-nuggets analogous to those observed in other experimental studies.

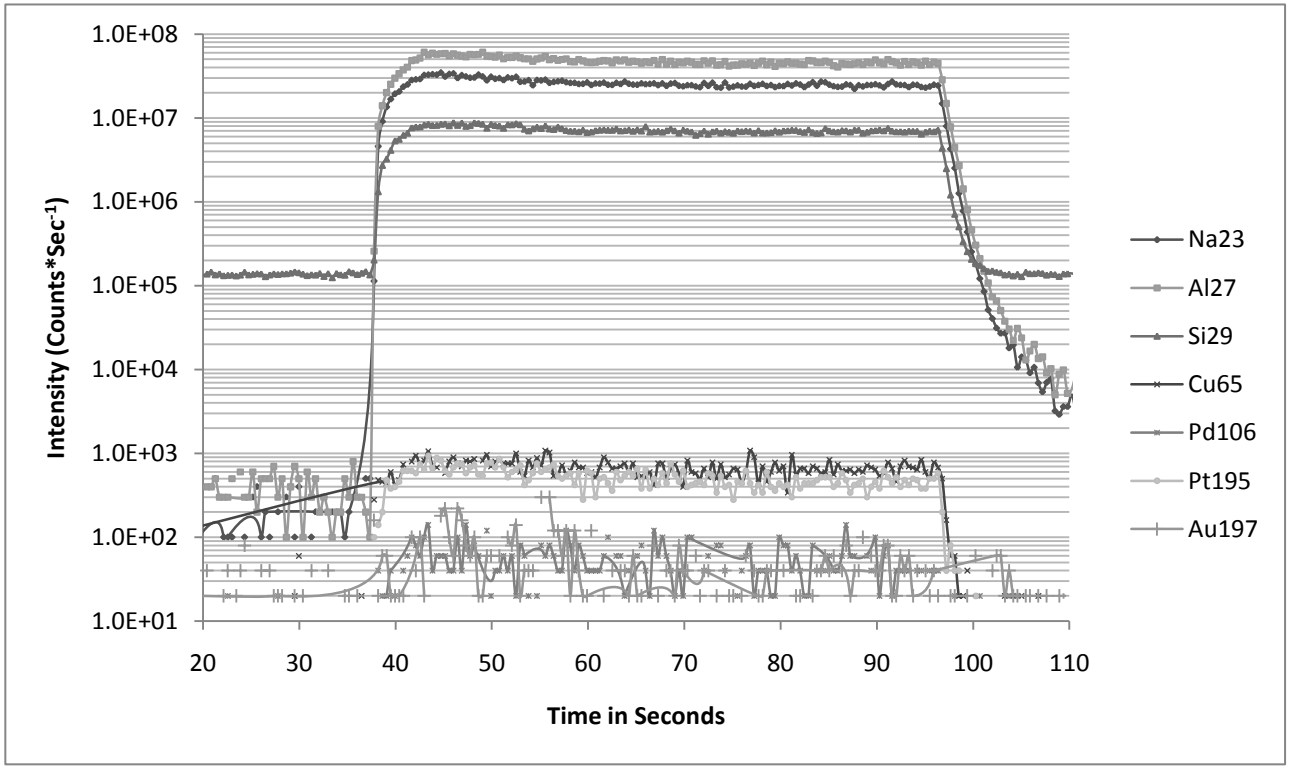

Figure 2 Nano-nugget "free" LA-ICP-MS signal from quenched silicate melt. All metal signals display some small degree of heterogeneity, however these signals are comparatively homogenous with respect to the signal in Figure 1.

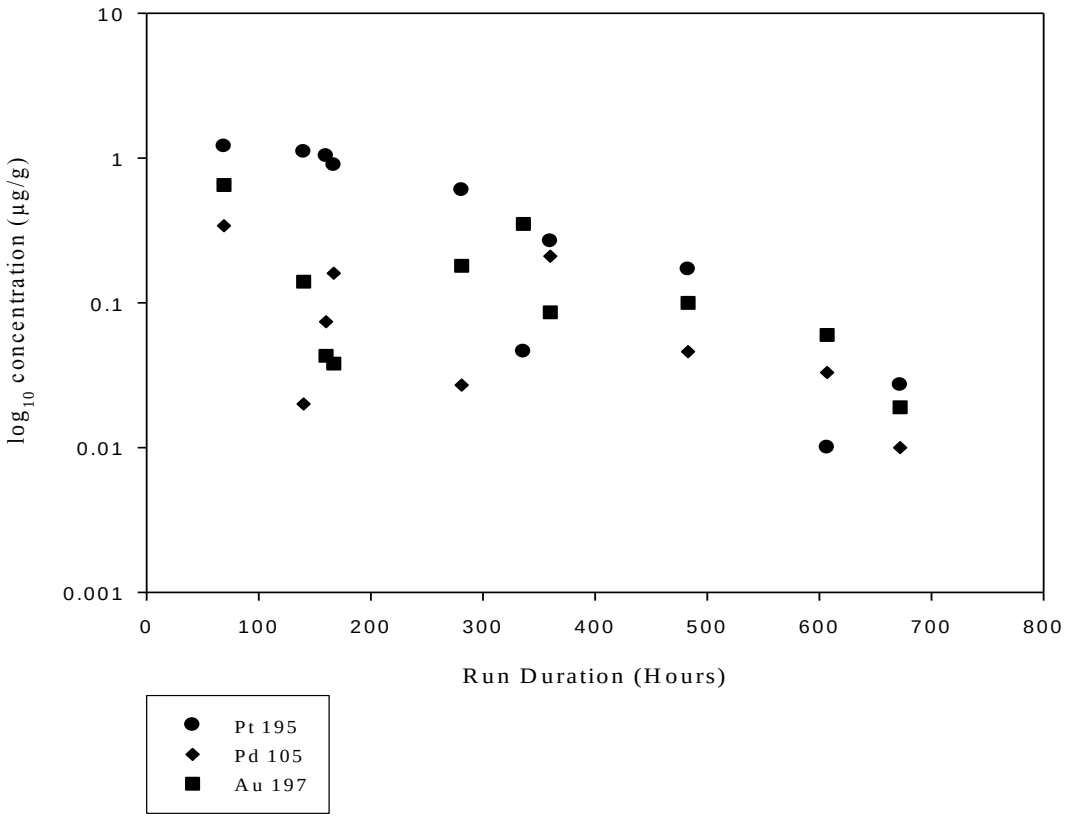

Figure 3. The concentration of Pt, Pd and Au in the silicate melt as a function of run duration. The uncertainties on each datum are smaller than the symbol size. Note the general decrease in metal solubility as experimental run duration increases.

Table 5.The mean EPMA determined composition of the recovered monosulfide solid solution.

Run #	Fe	S	Cu	Ni	Pd	Pt	Au	Total
12	55.08 (0.87)	40.18 (0.38)	2.16 (0.71)	0.05 (0.007)	2.38 (0.50)	< DL	< DL	100.69 (0.3)
13	53.17 (0.23)	38.9 (0.51)	4.83 (0.77)	0.05 (0.004)	2.44 (1.73)	< DL	< DL	99.54 (0.7)
15	49.71 (1.6)	39.69 (0.36)	2.77 (NA)	5.3 (0.36)	2.33 (0.69)	0.33 (0.18)	< DL	100.07 (0.7)
46	55.08 (1.2)	38.9 (0.22)	4.14 (1.09)	0.14 (0.05)	0.90 (0.42)	< DL	< DL	100.28 (0.5)
47	53.5 (1.1)	38.91 (0.55)	5.01 (2.62)	0.43 (0.17)	1.31 (0.26)	0.06	< DL	100.35 (0.3)
48	53.42 (1.9)	38.63 (0.7)	5.41 (2.67)	0.51 (0.07)	1.18 (0.56)	0.18 (0.04)	< DL	100.31 (0.5)
50	53.31 (1.4)	38.98 (0.48)	5.10 (2.06)	0.32 (0.02)	1.79 (0.25)	0.22 (0.02)	< DL	100.53 (0.5)
34	58.78 (0.46)	37.32 (0.23)	4.10 (0.61)	< DL	< DL	< DL	< DL	100.37 (0.2)

All values are defined as wt. %; the 1σ standard deviation is reported in parentheses.

Table 6. The mean LA-ICP-MS determined Pd, Pt and Au concentrations.

Run #	Pd (Sulfide)	Pd (NBS-610)	Pt (Sulfide)	Pt (NBS-610)	Au (NBS-610)
12	2.87 (0.15)	3.3 (0.18)	24 (1.3)	13 (.79)	131 (79)
13	NA	NA	NA	NA	NA
15	2.31 (0.06)	2.54 (0.1)	470 (40)	1789 (170)	230
46	NA	0.5 (0.13)	NA	108 (52)	108
47	NA	1.2 (0.1)	NA	236 (40)	136
48	NA	1.41 (0.02)	NA	561 (24)	286 (68)
50	NA	1.9 (0.08)	NA	910 (195)	134 (24)
34	NA	NA	NA	NA	9.1 (5.3)

The LA-ICP-MS spectra for Pd and Pt were reduced using both a synthetic Pt-Pd-bearing sulfide standard and also NBS-610; the different reduction methods are denoted as sulfide and NBS-610, respectively. 1σ standard deviations are reported in parentheses.

Table 7. The mean EPMA quantified compositions of recovered intermediate solid solution.
All values are given as wt. % with 1σ standard deviations reported in parentheses.

Run #	Fe	S	Cu	Ni	Pd	Pt	Au	Total
12	37.23 (0.91)	35.28 (0.28)	27.24 (1.01)	<DL	<DL	<DL	2100 (2500)	100.17 (0.4)
13	38.54 (0.19)	34.98 (0.25)	26.43 (0.04)	<DL	<DL	<DL	3080 (490)	100.29 (0.4)
15	38.03 (0.11)	34.74 (0.15)	27.64 (0.07)	<DL	<DL	<DL	<DL	100.51 (0.1)
46	35.48 (1.3)	35.13 (0.38)	28.19 (0.71)	<DL	<DL	<DL	<DL	99.14 (0.7)
47	37.85 (0.15)	34.82 (0.35)	26.96 (0.40)	<DL	<DL	<DL	<DL	99.76 (0.1)
48	38.75 (0.15)	34.83 (0.13)	25.82 (0.17)	0.12 (0.01)	<DL	<DL	NA	99.73 (0.2)
49	37.39 (0.35)	35.45 (0.15)	26.78 (0.38)	0.08 (0.01)	<DL	<DL	1400 (1400)	100.24 (0.2)
50	37.62 (0.44)	35.2 (0.22)	26.97 (0.33)	<DL	<DL	<DL	1100 (2400)	100.02 (0.4)

Table 8. The mean LA-ICP-MS quantified concentrations of Au, Pt, and Pd. The LA-ICP-MS spectra for Pd and Ptwere reduced using both a synthetic Pt-, Pd-bearing sulfide standard and also NBS-610; denoted as EPMA and LA-ICP-MS, respectively. The 1σ standard deviations are reported in parentheses.

Run #	**Pd (Sulfide)**	**Pd (NBS-610)**	**Pt (Sulfide)**	**Pt (NBS-610)**	**Au (NBS-610)**
12	NA	311 (387)	NA	0.62 (0.5)	5585 (14)
13	NA	64 (76)	NA	7.1 (1.9)	7220 (1256)
15	NA	1541 (94)	NA	862 (16)	107 (55)
46	NA	93 (46)	NA	4.3 (0.8)	3706 (1483)
47	NA	114 (49)	NA	19 (29)	4404 (1153)
48	NA	NA	NA	NA	NA
49	NA	172 (196)	NA	1.99 (0.4)	6771 (1895)
50	NA	276 (183)	NA	62 (117)	5693 (1739)

Table 9. Individual EPMA point analyses of quenched sulfide liquid for Run 32, 33, and 34. Note the heterogeneous distribution of Au. Each point analysis was performed using a broad, 40 micron beam in an attempt to re-integrate the composition of the sulfide liquid to that of run conditions.

	Fe	S	Ni	Pd	Pt	Au	Cu	Total
				Run 32 quenched sulfide				
	20.6	30.21	0.09	<DL	<DL	0.04	49.3	100.31
	18.4	29.05	0.08	0.04	<DL	1.5	51.38	100.5
	22.27	30.95	0.13	0.12	<DL	6.41	41.63	101.54
	18.62	29.28	0.05	<DL	<DL	0.07	53.02	101.06
	21.76	30.63	0.1	<DL	<DL	1.33	45.81	99.64
	20.97	30.24	0.06	<DL	<DL	0.15	48.63	100.09
	22.44	31.1	0.12	0.13	<DL	4.71	42.77	101.28
	19.87	29.7	0.15	0.02	<DL	0.92	48.52	99.2
	23.53	30.81	0.11	0.02	<DL	1.49	42.98	98.97
	18.92	28.64	0.07	0.05	<DL	2.44	50.53	100.67
Mean	**20.74**	**30.06**	**0.10**	**0.06**	**NA**	**1.91**	**47.46**	**100.33**
1 σ	**1.77**	**0.86**	**0.03**	**0.05**	**NA**	**2.11**	**3.95**	**0.86**
				Run 33 quenched sulfide				
	26.96	30.8	<DL	<DL	<DL	<DL	41.81	99.6
	26.44	30.29	<DL	0.05	<DL	<DL	43.2	100.01
	26.61	30.25	<DL	<DL	<DL	0.02	43.13	100.05
	27.59	31.86	<DL	0.02	<DL	0.16	41.12	100.78
	26.44	30.85	<DL	<DL	<DL	0.03	42.83	100.19
	26.91	30.93	<DL	0.04	<DL	0.57	42.24	100.72
	26.43	29.83	<DL	0.05	<DL	0.09	44.41	100.85
	26.58	30.09	<DL	0.04	<DL	0.1	44.34	101.18
Mean	**26.75**	**30.61**	**NA**	**0.04**	**NA**	**0.16**	**42.89**	**100.42**
1 σ	**0.40**	**0.64**	**NA**	**0.01**	**NA**	**0.21**	**1.15**	**0.54**

				Run 34 quenched sulfide				
	23.56	28.65	<DL	0.02	<DL	0.17	47.84	100.26
	33.03	30.73	<DL	0.3	<DL	0.41	35.13	99.62
	35.87	31.46	<DL	0.24	<DL	0.19	30.72	98.51
	19.44	27.41	<DL	<DL	<DL	0.07	52.02	98.96
	18.33	26.57	<DL	0.1	<DL	<DL	53.48	98.5
	17.95	26.66	<DL	<DL	<DL	0.14	54.3	99.05
	28.75	29.63	<DL	<DL	<DL	0.06	42.27	100.72
	32.33	30.41	<DL	0.38	<DL	0.05	37.95	101.13
	19.81	27.34	<DL	0.02	<DL	<DL	53.08	100.26
	22.64	28.22	<DL	<DL	<DL	0.17	49.67	100.73
	18.17	26.99	<DL	<DL	<DL	0.11	54.31	99.59
Mean	**24.53**	**28.55**	**NA**	**0.18**	**NA**	**0.15**	**46.43**	**99.76**
1 σ	**6.74**	**1.75**	**NA**	**0.15**	**NA**	**0.11**	**8.52**	**0.93**

Table 10. Calculated sulfur fugacity for all experimental runs.

Run #	Duration (Hrs)	S in glass (µg/g)	log fS_2[1] (bar)	log fS_2[2] (bar)
12	69	152 (39)	-1.05	0.07
13	167	233 (48)	0.02	-0.52
15	360	245 (24)	0.15	-0.14
46	160	152 (49)	-1.05	-0.92
47	336	227 (49)	-0.03	-0.87
48	483	185 (34)	-0.56	-0.86
49	607	153 (14)	-1.02	-0.90
50	672	143 (10)	-1.19	-0.76
32	140	151 (19)	-1.06	NR*
33	231	87 (20)	-3.21	NR*
34	281.5	73 (17)	-3.64	-5.16

* NR indicates that mss was not recovered from the charge

1. Sulfur fugacity calculated by using the Clemente et al. (2004) empirical algorithm.

2. Sulfur fugacity calculated by using the Toulmin and Barton (1964) algorithm

**The 1σ standard deviation for EPMA sulfur analysis is reported in parentheses.

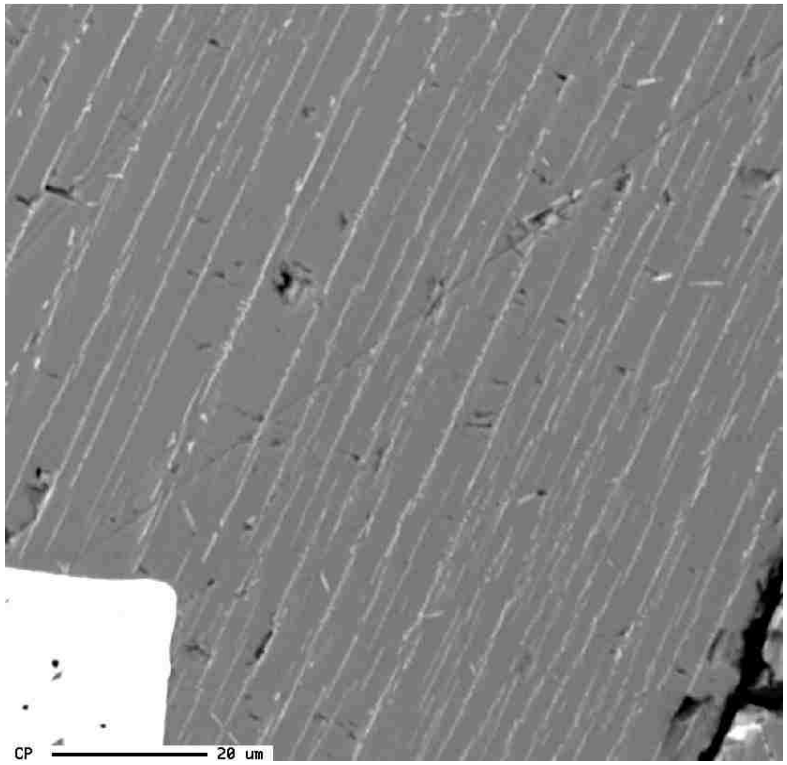

Figure 4. BSE image of fine scale exsolution textures in mss; exsolution features are a Pd-Ni-Cu rich sulfide. The high Z# phase in the lower left hand corner is metallic Au. The scale bar is 20 μm.

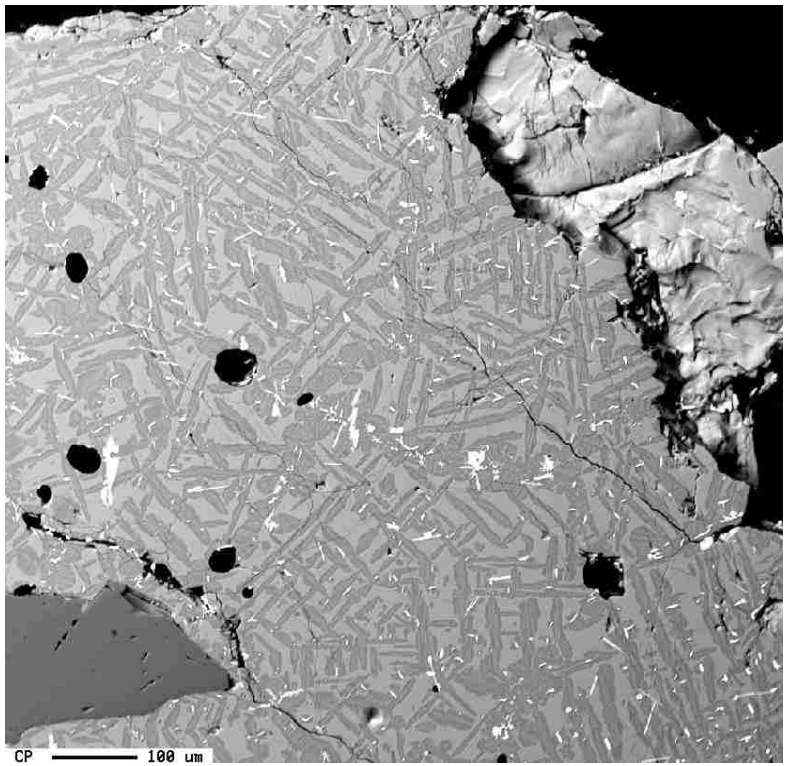

Figure 5. BSE image of a sulfide entity interpreted to be a re-crystallized sulfide liquid. Dark and light grey intergrowths are iss and bn. The scale bar is 100 μm. The dark grey crystal at lower left is magnetite which coexisted with the sulfide liquid at run conditions.

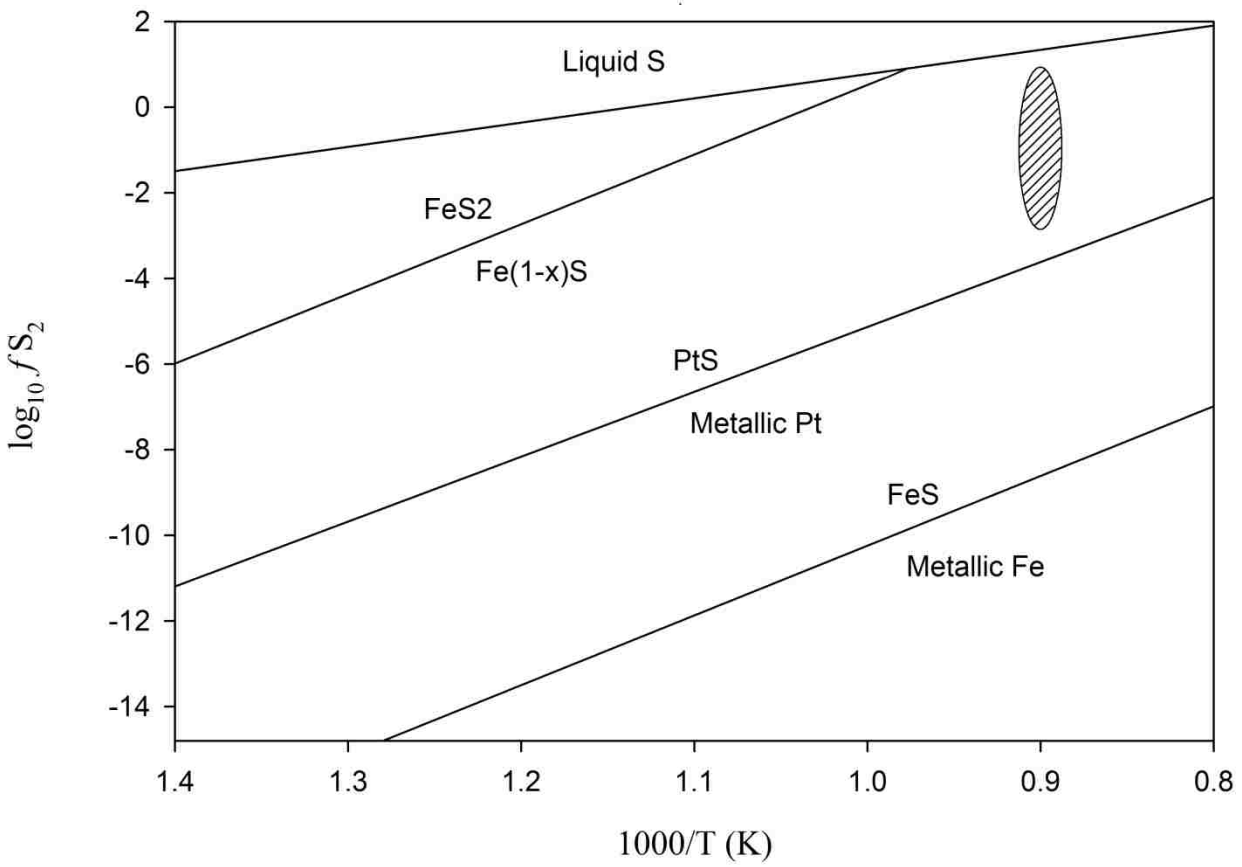

Figure 6. Plot of fS_2 buffer curves relevant to calculated experimental sulfur fugacity values. Experimental fS_2 values are schematically represented by the stippled ellipse. Buffer curves modified after Fleet et al. 1999.

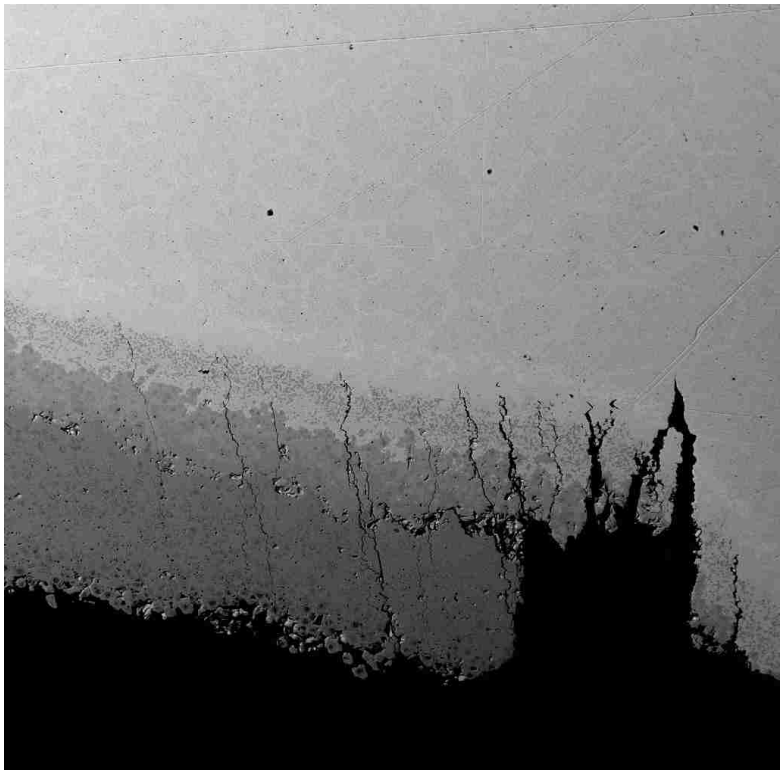

Figure 7. An advancing sulfidation front in Pt foil chip in run of 360 hours. Outer rim becomes (Pt,Pd,Fe)S in composition, where as the inner portion of the sulfidation front is nearly pure PtS grading into metallic Pt.

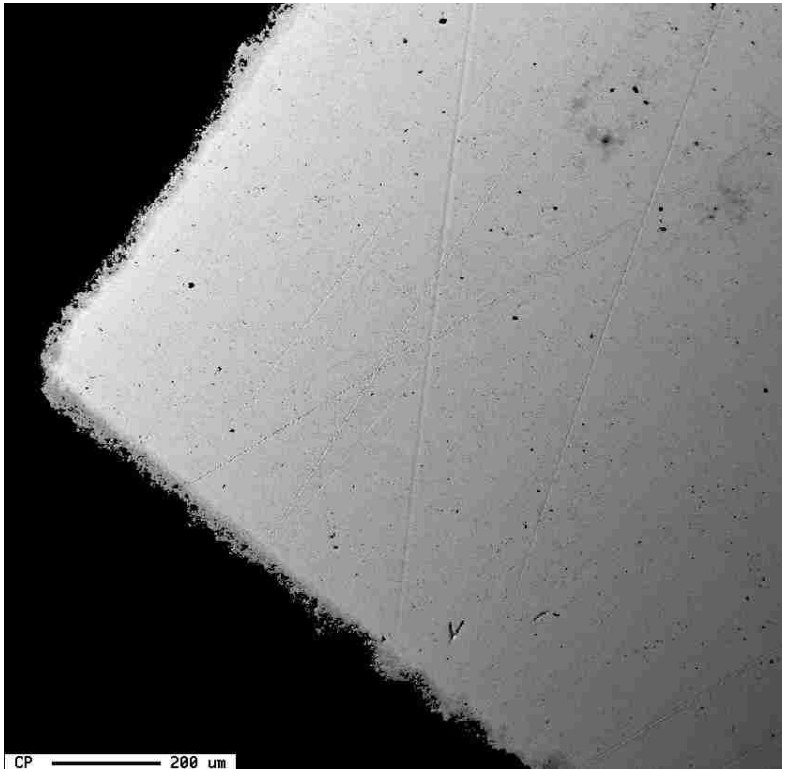

Figure 8. Thin sulfidation rim (dark gray rimming the light grey) on a Pt foil chip in run of 67 hours.

CHAPTER THREE

Au SOLUBILITY IN Cl-BEARING, HYDROUS BASALTIC MELTS AT VARIABLE fO_2

Abstract

We have performed experiments to evaluate Au solubility in natural, Cl- and S-bearing basaltic melts. Experiments were carried out 1000ºC and 200 MPa, and oxygen fugacity was controlled at the fayalite-magnetite-quartz (FMQ) oxygen fugacity buffer and FMQ + 4.5. All experiments were saturated with a metal-chloride aqueous solution, loaded initially as a 10 wt% NaCl eq. fluid. The stable phase assemblage at FMQ consists of basalt melt, olivine, clinopyroxene, a single-phase aqueous fluid, and metallic Au. The stable phase assemblage at FMQ + 4.5 consists of basalt melt, clinopyroxene, magnetite-spinel solid solution, a single-phase aqueous fluid, and metallic Au. Silicate glasses (i.e., quenched melt) and their contained crystalline material were analyzed by using both electron probe microanalysis (EPMA) and laser ablation inductively coupled plasma mass spectrometry (LA-ICP-MS). Measured Au concentrations in the quenched melt range from 4.8 μg g^{-1} to 0.68 μg g^{-1} at FMQ + 4.5 and 0.54 μg g^{-1} to 0.1 μg g^{-1} at FMQ. The measured solubility of Au in olivine and clinopyroxene was consistently below the LA-ICP-MS limit of detection (i.e., 0.1 μg g^{-1}). The melt solubility data place limitations on the maximum dissolved Au content of hydrous basaltic liquids at geologically relevant fO_2 values, and are consistent with the behavior of Au being not entirely controlled by fO_2 in Cl- and S- bearing silicate liquid at low oxidation states below ~ QFM + 1.

Introduction

The geochemical behavior of Au as a trace component dissolved in silicate liquids, common magmatic silicate minerals, and oxide minerals has implications for processes ranging from the genesis of magmatic-hydrothermal ore deposits (i.e., porphyry-, high-sulfidation epithermal-, and layered-mafic intrusion-hosted deposits) (Audétat et al., 1998; Bell et al., 2009; Hedenquist and Lowenstern, 1994; Naldrett and Duke, 1980; Frank et al., 2002; Simon et al., 2005) to core formation and the chemical differentiation of the early bulk earth (Cottrell and Walker, 2006; O'Neill et al., 1995; Righter et al., 2008; Ringwood, 1966). Two possible origins for metallically-fertile, siderophile-element-enriched silicate melt are: 1) the low degree partial melting of oxidized, sulfide-free asthenospheric mantle (Mungall, 2002); and, 2) the non-mutually exclusive process of siderophile element enrichment in residual liquids, driven by the crystallization and differentiation of sulfide-free basaltic magmas (Mustard et al., 2006). Mantle derived silicate liquids are widely accepted as the primary agent of chemical mass transfer for Au and other siderophile elements from mantle to crustal reservoirs. Therefore, it is essential to understand the thermodynamic and compositional variables that exert influence on the capacity of mantle derived basaltic liquids to dissolve and potentially fractionate Au and other siderophile elements. Solubility data defining the maximum Au capacity of silicate liquids in equilibrium with metallic alloys or sulfide phases are essential for the purpose of modeling Au delivery into crustal magmatic systems that source ore-forming magmatic-hydrothermal systems.

Extant experimental studies have demonstrated the importance of oxygen fugacity (fO_2) and to a more limited extent, the effects of pressure and bulk composition, on the

solubility of many siderophile elements in silicate liquid. Several experimental studies have concluded that the variation of the fO_2 imposed on select silicate liquids alters, by orders of magnitude, the solubility of many siderophile elements in the silicate liquid (Blaine et al., 2005; Borisov and Palme, 1996, 2000; Brenan et al., 2005; Ertel et al., 1999). Experiments with anorthite-diopside eutectic liquids demonstrate that the solubility of most siderophile elements decreases linearly with the decreasing oxidation state of the liquid, following a slope defined by the oxidation state of the stable metallic oxide species in the melt. Additionally, the small, yet variable, effect of pressure on the measured solubility of Ni, Pt, and Pd in silicate melt is also an important factor (Ertel et al., 2006; Righter et al., 2008). Most recently, Botcharnikov et al. (2010) quantified the effects of dissolved Cl and S on Au solubility in andesitic and dacitic liquids at fO_2 ~ NNO. Their data indicate that the presence of both Cl and S in the silicate melt are correlated with an increase in the solubility of Au in the melt.

The aforementioned studies have advanced significantly our understanding of the solubility behavior of select siderophile metals in silicate melt. However, there are few experimental data that constrain the solubility behavior of siderophile metals in natural H_2O-, Cl-, and S-bearing basaltic liquids and crystalline silicate and oxide phases. In this study, we performed experiments to elucidate the influence of fO_2 on Au solubility in H_2O-saturated, Cl-, and S-bearing basaltic silicate liquids. Further, the experimental runs were designed to quantify the solubility of Au in clinopyroxene and olivine in equilibrium with the experimental melt to better understand the effects of simple crystal fractionation on the Au content of basaltic melts during crystallization along liquid lines of decent.

Experimental Design and Rationale

Experimental Techniques

Experiments were performed in near-horizontal (i.e., the vessel and furnace are both at a positive angle of 10^{o} relative to the horizontal lab bench), rapid quench titanium-zirconium-molybdenum (TZM) pressure vessels at the University of Nevada, Las Vegas. Additional experiments were performed in a Shaw-membrane-equipped, internally heated gas pressure vessel (IHPV) at the American Museum of Natural History. All experiments were carried out in either Ar ± H_2 or Ar-CH_4-H_2 mixed gas pressure media at 1000°C and nominal pressures ranging from 190 to 200 MPa. Measured temperature gradients imply that the temperature uncertainty in the TZM runs at any position within the charge is ± 12°C from the reported run temperature. Temperatures in the IHPV experiments, including the effect of thermal gradient, are constrained to ± 5°C from the reported run temperatures. Pressure was monitored by using a bourdon tube strain gauge with a precision of ± 5 MPa in both the IHPV and TZM experiments.

Starting Materials

Starting materials consisted of a tungsten carbide milled (<5 μm final grain size) dolerite powder from the lower chilled margin of the Ferrar Dolerite, McMurdo Dry Valleys, Antarctica, and a NaCl-KCl-HCl aqueous solution. The mineralogy of the starting dolerite consisted primarily of orthopyroxene, plagioclase, augite, and minor oxide phases (Boudreau and Simon, 2007); this phase assemblage was confirmed with the SEM and EDS analysis. The chemical composition of the starting dolerite was determined by using inductively coupled plasma mass spectrometry and is presented in Table 11. The starting aqueous solution was prepared to a total salinity of 10 wt. % NaCl

eq. The molar ratios of NaCl:HCl and NaCl:KCl in the aqueous solution were set to unity with a ∑Cl concentration of 0.17 molar. All experiments were contained in Au capsules, fixing the Au activity of the experimental system at unity. Starting assemblages, run durations, P, T and fO_2 values are listed in Table 12. Some experiments also contained a pre-fractured cylindrical (2 mm OD x 5 mm length), inclusion-free chip of quartz in an unsuccessful attempt to trap the aqueous phase as synthetic fluid inclusions.

Capsule Configuration

The experimental capsule configuration (Figure 9) consisted of a small length of Au tubing (1 mm ID, 1.2 mm OD x 10 mm length) welded at the base and loaded with approximately 10-13 mg of powdered dolerite which was compressed into the bottom of the tube. The top of this capsule was mechanically crimped, but not welded. This smaller capsule containing the dolerite was then loaded into a larger Au capsule (4.8 mm ID with a 5 mm OD x 20 mm length) along with 30 µL of starting aqueous solution that was pipetted into the base of the outer capsule. This capsule configuration was designed to allow us to recover the silicate melt as a cylindrical aliquot of glass (i.e., quenched melt) + crystalline material that preserves the geometry of the fluid-melt interface. The outer capsule was triple crimped and welded shut. Masses of the capsules were monitored both before and after welding to ensure that the solution was not lost during welding. The volume of solution loaded was carefully selected to ensure that the calculated volume of the aqueous phase at the P-T conditions of the experiment (approximated using the density predicted by the EOS of Driesner and Heinrich, 2007) would not exceed the total available volume of the experimental capsules. Based on the analog phase relations for

the NaCl-H_2O system (Driesner and Heinrich, 2007), the aqueous fluid in the experiments is a single phase supercritical aqueous fluid at run conditions.

Control and Estimation of Experimental fO_2 values

Oxygen fugacity of the experiments was fixed at either ~FMQ + 4.5 or ~FMQ. Low fO_2 values were achieved through the addition of CH_4 and H_2 to the Ar pressure medium in the TZM and IHPV experiments, respectively. Oxidizing experiments were run at the intrinsic fO_2 of the TZM and IHPV pressure vessels. Several experimental studies have utilized pure-Ar as a pressure medium in TZM and IHPV apparatuses along with Ni-Pd or hydrogen redox sensors to measure fO_2 (Berndt et al., 2005; Matthews et al., 2003; Popp et al., 1984). These studies demonstrate that relatively oxidizing conditions ranging from FMQ + 4 to FMQ + 4.5 prevail as "intrinsic" fO_2 values. Based on these studies, we assumed an oxidation state of approximately FMQ + 4.5 for all experiments performed at the intrinsic oxidation state of the TZM pressure vessels. Reducing experiments in the TZM vessels were performed with a fixed partial pressure of 6.5 bars of CH_4 that was pre-charged into the pressure vessel at ambient conditions. Using the equilibrium constant for the CH_4 dissociation reaction and tabulated hydrogen and methane fugacity coefficients, it is possible to estimate the fH_2 of the pressure medium allowing us to calculate the approximate fO_2 of the experiment at run conditions. Calculated fO_2 values of the reducing experiments are approximately FMQ ± 0.5 log units. Additionally, in all reducing TZM runs, sealed Pt capsules containing Ni-NiO powder mixtures and H_2O were run behind the experimental charges (Figure 1). In all of these low fO_2 experiments, the NiO was reduced and recovered entirely as metallic Ni. Hydrogen fugacity in the

IHPV experiments was fixed by using a Shaw membrane and continuously monitored with a pressure transducer.

All experimental charges were saturated with a supercritical aqueous phase in the $MeCl_n$-H_2O (where n is proportional to the charge of the metal) system. Reduction of water activity in the experimental charge was calculated for the H_2O-NaCl system by using the equation of Aranovich and Newton (1996). Calculated aH_2O values are 0.96 for the aqueous phase at experimental P-T conditions. The effect of aH_2O values less than unity on the calculated fO_2 values of an experiment is shown in Figure 10. Reduction of the aH_2O in the loaded aqueous solution at our experimental P-T conditions did not significantly decrease the estimated fO_2 values.

Analytical Methods

Electron Microprobe Analysis

The glass cylinders and glass-hosted crystals (i.e., cpx and ol at FMQ, and cpx and mt-sp at FMQ+4.5) recovered from each run were mounted in epoxy and polished for electron probe microanalysis (EPMA). Phase identification and textural relationships were documented by using energy dispersive spectrometry (EDS) and back-scattered electron (BSE) imaging. Silicate glass, clinopyroxene, and olivine were analyzed for major elements by using a four spectrometer JEOL 8900 SuperProbe at the University of Nevada, Las Vegas to perform wavelength dispersive spectrometry (WDS). Analysis of the silicate glasses employed a 15 kV accelerating potential and a 3 nA beam current used in conjunction with a de-focused 10 μm beam in order to minimize alkali diffusion (Morgan and London, 2005). Analysis of pyroxene and olivine utilized a 10 nA beam

current with a 2 μm beam diameter. A ZAF matrix correction algorithm was applied to calculate element concentrations. Natural glass and crystal standards were used for all analyzed elements. Standards for glass analyses included: VG568 rhyolite glass for Si, Na, and K; sillimanite for Al; hornblende for Ca; VG-A99 basaltic glass for Fe and Ti; kaersutite for Mg; scapolite for Cl; and rhodonite for Mn. The basaltic glass standards VG-A99 and VG-2 were analyzed periodically as blind standards to monitor the accuracy of the glass analytical routine. The concentration of H_2O in the glass was determined by EPMA difference and should be considered semi-quantitative.

LA-ICP-MS Analysis

Laser ablation inductively coupled plasma mass spectrometry (LA-ICP-MS) analyses were performed on the glass and crystalline silicate phases at the Institute for Isotopengeologie and Mineral Rohstoffe at the ETH in Zurich, Switzerland. All analyses utilized a homogenized Eximer ArF laser (λ=193 nm) coupled with a Perkin-Elmer 6100 DRC quadrupole ICP mass spectrometer. A carrier gas mixture consisting of He (1.15 L min^{-1}) and H_2 (5 ml min^{-1}) was employed to increase sensitivity and lower the limits of detection for all elements analyzed (Guillong and Heinrich, 2007). Ablation crater size was varied from 40 μm for glass to 20 μm for clinopyroxene crystals. The repetition rate for the ablation was fixed at 10 Hz with energy densities ranging from 10-14 J cm^{-1}. The SILLS software package (Guillong et al., 2008) and NBS-610 glass standard were utilized for all data processing and reduction. Internal standards of Al and Si (quantified by using EPMA as described above) were utilized in data reduction for homogenous glasses (i.e., long duration experiments). Compositionally, inhomogeneous short-duration experiments were reduced via normalization of the oxide components. Data reduction by

both methods yields statistically identical concentrations of Au and other trace components. The basaltic glass standard VG-A99 was analyzed intermittently as a monitor of analytical accuracy. Additionally, the Au/Ca count-rate ratios for NIST-610 were carefully evaluated for each standard analysis in order to ensure that a potentially inhomogeneous distribution of Au in the NIST-610 glass standard did not manifest as variability in the calculated Au concentrations of the experimental glasses. No systematic error due to a potentially inhomogeneous Au distribution in the NIST 610 standard was found in any of the analytical blocks; thus, the apparent variability in the analyzed Au concentrations, discussed in detail below, represents accurately the actual, subtle variability in the Au content of the experimental glasses.

Results and Data

Spatial Relationships: Analytical Transects and Phase Distributions

Recovered cylinders of glass, and the glass-hosted crystalline material, were mounted horizontally in epoxy wafers such that the full length of the of the glass cylinder exposed and available for analysis. This orientation preserved the original fluid melt interface geometry and allowed us to perform EPMA and LA-ICP-MS analytical transects along the full height of the original melt column. Crystalline material was homogenously distributed throughout the volume of quenched melt in the short duration experiments. The majority of crystalline material in some longer duration runs was confined to the portion of the liquid column opposite the fluid melt interface. Figure 14 is a back-scattered electron (BSE) image of a recovered glass (i.e., quenched melt) cylinder and illustrates differences in the spatial distribution of crystalline material. We interpret the

observed texture to represent density-driven crystal settling in long duration runs. Clinopyroxene and olivine crystals were analyzed throughout the entire volume of melt when possible.

Stable Phase Assemblages

The stable phase assemblage varied with the fO_2 imposed on the run. Phase assemblages from experiments performed at FMQ+4.5 contained silicate liquid, clinopyroxene, magnetite-spinel solid solution, and supercritical aqueous fluid. Phase assemblages recovered from experiments performed at FMQ contained silicate liquid, clinopyroxene, olivine, and supercritical aqueous fluid. The modal abundance of crystalline material was estimated visually to be 30-35%, with clinopyroxene being the most abundant crystalline phase at both oxidizing and reducing conditions. Olivine abundance in reducing experiments is low relative to the total abundance of clinopyroxene with ratios of clinopyroxene/olivine that are approximately 20:1. The grain size of the crystalline material was observed to coarsen with increasing run duration.

Major Element Compositions of the Quenched Melt

Table 13 presents the average melt composition for all EPMA analytical transects from a given experiment. The glasses recovered from the long-duration runs are chemically homogeneous. EPMA data from an analytical transect of the compositionally homogenous melt from IHPV1-2 are presented in Table 14. We observe some variability in the chemical composition of the silicate liquid in short duration experiments. The observed compositional variability of the melt in short-duration runs is manifested in the following elements: Na, K, Cl, Si, Al, Fe, and Mg. Compositional data from an EPMA analytical transect, set orthogonal to the fluid-melt interface in short-duration run TZM

11, are presented in Table 15. These data illustrate the tenor and magnitude of the observed compositional variability in the short duration experiments. Concentrations of Na, K and Cl generally increase monotonically approaching the exchange interface from the base of the melt column. The SiO_2 content of the melt also increases approaching the fluid melt interface, however this increase is generally more restricted and confined to the 100-200 microns of melt immediately adjacent to the fluid-melt interface. The increasing concentrations of Na, K, Cl, and Si in the melt are interpreted to reflect the diffusion of Na, K, Cl, and Si into the portions of the liquid that are under-saturated (i.e., reflective of disequilibrium with the aqueous phase) with respect to these components. The volumetric extent to which these fluid components have interacted with the melt is controlled by the relative differences in the diffusivities of each component; thus, we observed that the network modifying cations Na^{1+} and K^{1+} have diffused into the melt to a much greater volumetric extent than has the network forming cation $^{IV}Si^{4+}$.

The measured concentrations of Al, Mg, Ca, and Fe generally decrease from the base of the melt column to the fluid melt interface only in the short duration runs. The measured elemental concentration gradients in these runs may reflect simple dilution of the melt from the addition of 5-8 wt% SiO_2 via introduction as a soluble component from the aqueous phase. The depletion of Al, Mg, Ca, and Fe near the fluid melt interface may alternatively reflect the leaching of these components into the chloride bearing aqueous solution. The exact nature and origin of the compositional gradient in the melt are not specifically relevant to Au solubility and will be discussed in detail in a separate publication. We highlight here that the measured Au concentrations along the entire

height of the melt column remain relatively consistent except for two short-durations which are discussed below.

Solubility of Au in Quenched Basalt Melt

The measured Au concentrations in silicate glass are presented in Table 12 and plotted as a function of fO_2 and experimental run duration in Figures 12 and 13, respectively. Table 12 also contains calculated analytical error, number of analyses, and the range of Au concentrations observed within each experiment. The measured concentrations of Au in the silicate liquid are consistent between runs of the same oxidation state. The concentrations of Au in the melt from experiments at ~FMQ + 4.5 range from a high of 4.8 μg g^{-1} to a low of 0.68 μg g^{-1}, with a mean (±1σ) of 1.98 μg g^{-1} ± 1.45 μg g^{-1}. The concentrations of Au in the melt from experiments at ~FMQ have a much more restricted range from 0.54 μg g^{-1} to 0.1 μg g^{-1}, with a mean (±1σ) of 0.35 μg g^{-1} ± 0.18 μg g^{-1}. The reported solubility values represent between 7 and 13 separate LA-ICP-MS analyses along the entire length and width of the recovered glass cylinder. The Au solubility data will be discussed in detail below.

Solubility of Au in Clinopyroxene and Olivine

Quantifying the concentration of Au, by using LA-ICP-MS, in the equilibrium crystalline phases proved to be extremely difficult owing to the relatively small size (i.e., 5μm-35μm) of clinopyroxene and olivine crystals recovered from most experiments. Furthermore, analyses of small diameter crystalline material would inadvertently include some volume of quenched liquid, yielding a mixed LA-ICP-MS signal that required deconvolution of the contribution from the crystal and the quenched melt. An additional analytical complication was that clinopyroxene and olivine crystals were often

intergrown with Au particles, as displayed in Figure 14, rendering an analysis contaminated with a large mass of metallic Au. Utilizing the fact that the Sc concentration in the clinopyroxene was a factor of 4-5 greater than that of the melt, the count rate of ^{45}Sc was monitored in order to delimit the "crystal only" portion of the signal from the mixed crystal-melt portions of the signals. The study of Brenan et al. (2005) indicates that crystalline olivine may be incredibly sluggish, even at high temperatures, to equilibrate with the siderophile element content of silicate melts. In light of this observation, the Au concentrations that we measured in crystalline material from the short duration runs may be out of equilibrium with the Au content of the early silicate liquids. Despite our best attempts to reduce the LA-ICP-MS limits of detection for Au by employing H_2 in the carrier gas (cf., Guillong and Heinrich, 2007) and utilizing the largest possible beam diameter for analyzing the crystalline material, the measured Au concentrations were consistently below the limit of detection. The limits of detection for the analyses of both olivine and clinopyroxene ranged from 0.1 to 0.05 μg g^{-1}. We suggest that these data constrain the Au solubility of both clinopyroxene and olivine to <0.1 μg g^{-1}.

Discussion

Insights from LA-ICP-MS Signal Processing snd Equilibrium Metallic Micronuggets

LA-ICP-MS analysis of quenched silicate melt affords unique insights into the spatial distribution of Au in the melt, beyond facilitating the simple exclusion of Au particles and micronuggests from signals. The presence, and treatment during signal processing, of

metal micronuggets in silicate glass has been discussed in a number of studies (e.g., Cottrell and Walker, 2006, Simon et al., 2008) with no consensus on whether the observed micronuggets should be included or filtered (i.e., removed) from LA-ICP-MS transient signals during signal processing. In the current study, we observed the presence of both large gold nuggets, visible in BSE (Figure 14), and small nuggets which were unresolveable with BSE. We interpret the BSE-observable Au nuggets as equilibrium metallic phases that coexisted with the melt and not as metal nuggets which nucleated and grew during quench. These observed large Au particles, often associated with vesicles, were generally visible and easily avoided during LA-ICP-MS analysis.

A second type of nugget was identified only during LA-ICP-MS signal processing of experimental silicate glasses with low Au concentrations that generally displayed inhomogeneous Au count rates even in the areas of melt where we observed no metal nuggets. The results from previous studies of the solubility of metals in silicate melts suggest that similar heterogeneities observed in nominally nugget-free portions of LA-ICP-MS signals may represent micronuggets that cannot be spatially resolved and, thus, cannot be removed during signal processing (Ertel et al., 1999). Such cryptic nano-particles would contaminate the signal with excess metallic Au, yielding concentrations that are not representative of the dissolved metal content of the quenched liquid. To explore whether or not the small-scale Au perturbations in the transient signal are in fact nuggets that require filtering during signal processing, we compared the transient signal for Au to other elements which should exist only as fully dissolved components in the melt.

Comparisons of the raw count-rate of ^{197}Au with the raw count-rates of ^{173}Yb, ^{238}U, and ^{208}Pb for an individual LA-ICP-MS signal reveal a striking similarity with respect to the lack of count-rate homogeneity. The measured isotopes ^{173}Yb, ^{238}U, ^{232}Th were chosen for the comparison because the measured concentrations of these elements overlap with that of the measured Au concentrations. For example, the mean count rate for ^{197}Au from one analysis of glass in experiment IHPV1-1 is 339 counts*sec^{-1}, with a 1σ standard deviation of 111 counts*sec^{-1} (32%). Mean count rates and standard deviations at the 1σ level for the same analysis for ^{173}Yb, ^{238}U, and ^{232}Th are 392 ± 240 (59%), 971 ± 359 (22%), and 3417 ± 1012 (29%) respectively. Based on the comparison of the standard deviations from the mean count rates, Au concentrations appear no less inhomogeneous than the concentrations of other trace elements endemic to the composition of the starting material. Figure 15 contains the raw LA-ICP-MS signal used for the comparison. The origin of the heterogeneous nature of the signals is unclear; however, invoking a cause and effect relationship between the signal and Au particles is inconsistent with the observation of similar variability in the signals of elements with no such known "nuggetting" behavior. The exact interpretation of the link between LA-ICP-MS signals and the physical state of the analaytes remains speculative at best. We suggest that the small-scale inhomogeneous nature of the Au signals may be related in some capacity to the application of the LA-ICP-MS analytical technique and that the observed small-scale perturbations in the Au transient signal should be included during signal processing. To filter these perturbations results in an artificially lower metal solubility in the silicate liquid.

Au Solubility in Basaltic Melts

Previous studies of Au solubility in hydrous and dry basaltic liquids over a range of pressures and temperatures have reported Au solubility values ranging from <1 μg g^{-1} to 60 μg g^{-1} (Bell et al., 2009; Borisov and Palme, 1996; Brenan et al., 2005; Frank et al., 2002; Jugo et al., 1999; Simon et al., 2005; Simon et al., 2003) The general conclusion from these studies is that Au solubility displays a first order dependence on oxygen fugacity values greater than $fO_2 = 10^{-6}$ bar and, therefore, must be present in the melt as an oxide species. Dissolution of Au into silicate liquids as a monovalent oxide species was proposed by Borisov and Palme (1996) in following the form:

Eq. 17 $$Au + \frac{n}{4} O_2 = AuO_{n/2}^{melt}$$

Rearranging the equilibrium constant for the above reaction in logarithmic form yields:

Eq. 18 $$\log_{10} AuO_{0.5} = \tfrac{1}{4} \log_{10} fO_2 + K_{17}$$

The Au concentrations measured in the experimental melts in this study do not strictly adhere to the anticipated slope predicted by the linear relationship between Au solubility as a monovalent oxide species and the imposed experimental fO_2 value. Despite the scatter in the data and the difference in slope, the measured Au concentrations from experiments at ~FMQ are consistently lower than the measured Au concentrations from the experiments at FMQ+4.5. The deviation of the Au concentrations in the reducing experiments from the values predicted by the relationship in Equation 2 may reflect the changing speciation of Au in silicate liquids with decreasing fO_2. For example, we calculate a predicted Au solubility value of 0.18 μg g^{-1} at FMQ for Au as an oxide species. This value is a factor of two lower than the measured value of 0.35 μg g^{-1}. We speculate that the elevated Au concentrations at low fO_2 values are caused by the

formation and increasing abundance of either Au-Cl or Au-S, or both, complexes in the melt. Furthermore, the possibility of a stable Au-silicide species, as suggested by Borisov and Palme (1996), cannot be excluded from consideration. The exclusion of the high Au solubility values in the 24 hour TZM runs, perhaps caused by fO_2 values higher than FMQ+4.5 during attainment of the imposed fO_2 during (see below for explanation), further decreases the slope of the observed Au-fO_2 relationship, strengthening the evidence for alternative Au species. The potential existence of a chloride species, however, seems most plausible given the high chlorine activity in the experimental melt. The probability of the existence of an Au-sulfide species is limited in melts at FMQ+4.5 because of the very low abundance of dissolved sulfide in the melt at this redox condition (Jugo et al., 2005; Mavrogenes and O'Neill, 1999). Botcharnikov et al. (2010) observed a linear correlation between Au concentration and Cl activity in andesitic melts at fO_2 values of approximately NNO and proposed the existence of a Au-Cl species in the melt. We suggest that $AuO_{0.5}$ is the most prominent Au species in chloride bearing silicate melts at the high oxidation states prevalent in the initial hours of the experiments over the first several hours at run temperature. Thus, fO_2 is the primary variable controlling Au solubility in the early experimental liquids. As fO_2 values inside the charge adjust to the imposed fO_2, the dominant Au speciation may shift to either Au-Cl or Au-S complexes, muting the effect of fO_2 while emphasizing the effects of the chlorine and sulfur activities of the melt. This finding is consistent with the results from Botcharnikov et al. (2010).

Interestingly, no consistent relationship between the composition of the melt and Au content is observed. In experiments TZM 20 and TZM 21 the concentration of Au increases subtly by a factor of 1.5- 2.0 (e.g., an absolute increase of 1 μg g^{-1} to 1.8 μg g^{-1})

in the volume of melt adjacent the fluid-melt interface. The origin of this Au concentration gradient appears to be correlated with the total alkali, Cl, and Si content of the liquid such that portions of the melt richer in alkalis, Cl, and Si contain higher concentrations of Au. This relationship is not observed in all experiments and awaits future study.

The apparent temporal evolution of the Au contents of the melts is significant for the experiments run at FMQ+4.5. The temporal variation of Au solubility in the melt is plotted in Figure 13. The highest measured Au concentrations in silicate glass are for the experiments of 24 hours duration. The measured concentrations of Au in silicate glass subsequently decrease with increasing run time. We suggest that the temporally increasing Au concentrations are caused by the initially highly oxidizing conditions of the charge present before internal redox equilibrium is attained. In contrast, experiments at reducing conditions have high fH_2 values such that the osmotic equilibrium of H_2 between the pressure vessel and the charge attains redox equilibrium more quickly relative to the experiments at intrinsic oxygen fugacity values (cf., Gaillard et al., 2002). Temporal variability in Au content is not observed in the experiments at ~FMQ. Inadvertent, subtle variations in the ratio of atmospheric gas to aqueous solution loaded into the charges may also affect the initial oxidation state of the charge, causing Au to dissolve readily into the melt as an oxide species during the initial hours of the experiment.

Au concentration in Clinopyroxene and Olivine

Data from the long duration experiments for Au solubility in olivine are consistent with data from Brenan et al. (2005). They report maximum Au concentrations in olivine

ranging from 0.1-μg g^{-1} to 0.005 μg g^{-1}. The highly incompatible nature of Au in the lattice of both clinopyroxene and olivine phases is not unexpected considering the relatively large ionic radius and the probable 1^+ oxidation state of Au. As a monovalent cation, the diadochy of Au in the olivine lattice appears to be extremely limited. Data from the current study suggest that Au compatibility on the clinopyroxene lattice appears similar in magnitude to that of olivine, but the relatively high LA-ICP-MS limits of detection prohibit making more than semi-quantitative comparisons.

Potential coupled substitution mechanisms involving Au^{1+} in the M2 site accompanied by Fe^{3+} or Al in the M1 site, or alternatively the presence of ^{IV}Al may enhance Au compatibility in clinopyroxene. It seems unlikely that coupled substitutions involving Au^{1+} would greatly enhance the capacity of clinopyroxene to sequester significant quantities of Au. The extremely low activities of Au in the melt are likely the dominant factor dictating the Au content of the crystalline material, even considering potential coupled substitution mechanisms. However, compositionally controlled enhancement of partition coefficient values for Au between pyroxenes and melt warrants further experimental investigation.

Conclusions

The new experimentally determined Au solubility data place important constraints on the maximum Au capacity of hydrous, Cl-, and S-bearing basalt liquid. The sum of the available data for Au solubility in silicate melts, including data from this study and other published data, is summarized as follows:

1. The precise nature of siderophile element speciation in silicate liquids at low fO_2 values remains enigmatic. Magmatic volatiles such as Cl and S may act as complexing anions that enhance the overall Au solubility in the melt, as well as altering Au speciation at low, geologically relevant oxygen fugacity values. From comparisons of Au solubility data in both hydrous and anhydrous studies, water seems to have little effect on the Au content of silicate melts. The existence of prominent Au species in silicate melts other than simple oxides has not yet been confirmed by spectroscopic techniques. Evidence for the existence of such species relies on a limited amount of experimental data that merely imply the existence of such species. The relative abundances of Au species in silicate melts where Cl, S, and O are all present remain unconstrained. The effect of pressure on the Au capacity of Cl and S bearing melts is not yet explored; high pressures may further promote the formation of Au-chloride and/or Au-sulfide species in the melt. Oxygen fugacity may not be the dominant factor controlling the behavior of Au in volatile bearing silicate magmas at geologically relevant redox conditions. The studies of Au (and other metal) solubility in mafic silicate liquids indicate that Au speciation and solubility mechanisms require significant future study.
2. The effects of bulk composition on the Au capacity of silicate melts remain fully unconstrained. Direct comparison of Au solubility values from studies in haplogranite systems to values from studies in basaltic and haplobasaltic systems cannot isolate the effects of bulk composition because of the large range of temperatures at which the studies were performed. Two experiments from this study indicate that increasing melt alkalinity and Cl content may enhance Au

solubility in the melt. Future studies are planned to explore the effect of melt composition at unique PT conditions.

3. Au solubilities in clinopyroxene and olivine, common silicate phases present in basaltic magmatic systems and their upper mantle sources, are likely very low (<0.1 μg g^{-1}). If coupled substitution mechanisms affect Au compatibility on the pyroxene lattice, static partition coefficients may not accurately reflect the partitioning behavior of Au in pyroxene fractionating magmatic systems. In light of this study, Au should be strongly enriched in liquids fractionating both clinopyroxene and olivine.

Au solubility in silicate liquids is a complex function of oxygen fugacity, the fugacities of other volatile components of the melt, and perhaps even the bulk composition of the liquid. These complexities challenge our ability to model siderophile element behavior in naturally fractionating, volatile bearing basaltic liquids. More experimental work is required before a quantitative model of the Au capacity of silicate melts can be fully developed. Specifically, the nature and effects of Au speciation in volatile bearing melts at low oxygen fugacity is required to fully predict the behavior of Au in magmatic systems. Finally, simple fractionation models utilizing static partition coefficient values for Au between common silicate phases and liquid will be complicated by the evolving bulk composition and volatile contents of the residual liquids as well as the potentially compositionally controlled Au contents of the pyroxenes crystallized from the melt.

Table 11. Major element composition of starting dolerite powder

SiO_2	53.61
Al_2O_3	14.55
FeO^{total}	9.1
MgO	6.55
CaO	10.59
Na_2O	1.77
K_2O	0.79
TiO_2	0.63
P_2O_5	0.1
MnO	0.18
Total	***98.72***

Table 12. Run conditions for all experiments.

Run	Duration (Hrs)	fO_2	Pressure	Temperature	Au ± 1σ (µg g-1)	2σ analytical error	Range* (µg g^{-1})	Au Gradient
TZM 11	7	FMQ + 4.5 ± 0.5	1.95 Kb ± 0.1	990 ± 12	1.46 ± 0.11	0.22	0.64 (n=12)	N
TZM 12	24	FMQ + 4.5 ± 0.5	1.95 Kb ± 0.1	990 ± 12	4.90 ± 0.21	0.36	1.2 (n=8)	N
TZM 20	18.5	FMQ + 4.5 ± 0.5	1.95 Kb ± 0.1	990 ± 12	1.10 ± 0.35	0.12	1.19 (n=13)	Y
TZM 21	25	FMQ + 4.5 ± 0.5	1.95 Kb ± 0.1	990 ± 12	2.90 ± 0.69	0.24	1.39 (n=12)	Y
IHPV 1-1	172	FMQ + 4.5 ± 0.5	2.00 Kb ± 0.05	1000 ± 5	0.64 ± .03	0.1	0.08 (n=9)	N
IHPV 1-2	144	FMQ + 4.5 ± 0.5	2.00 Kb ± 0.05	1000 ± 5	1.05 ± 0.03	0.16	0.07 (n=8)	N
TZM 23	6	FMQ ± 0.5	1.95 Kb ± 0.1	990 ± 12	0.35 ± 0.12	0.1	0.3 (n=12)	N
TZM 30	12	FMQ ± 0.5	1.95 Kb ± 0.1	990 ± 12	0.09 ± 0.01	0.04	0.06 (n=7)	N
TZM 31	24	FMQ ± 0.5	1.95 Kb ± 0.1	990 ± 12	0.26 ± 0.10	0.08	0.23 (n=10)	N
IHPV 1	192	FMQ ± 0.1	2.00 Kb ± 0.05	1000 ± 5	0.55 ± 0.05	0.12	0.15 (n=10)	N

*Range is reported as the difference between the minimum and maximum values obtained for a given experiment.

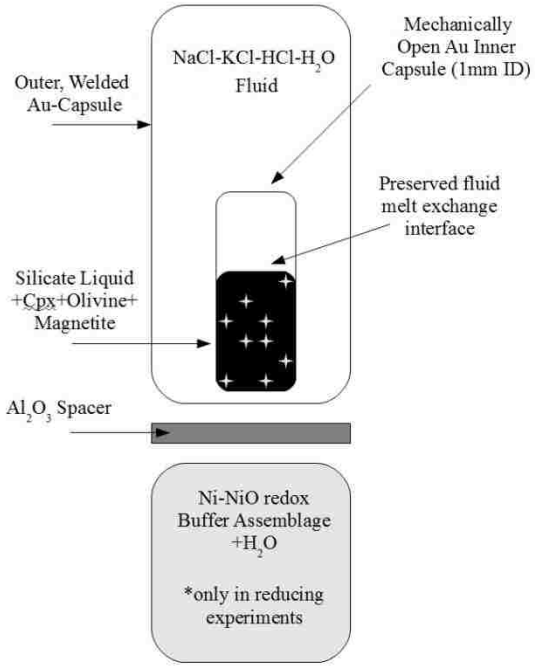

Figure 9. Schematic diagram of the experimental capsule configuration

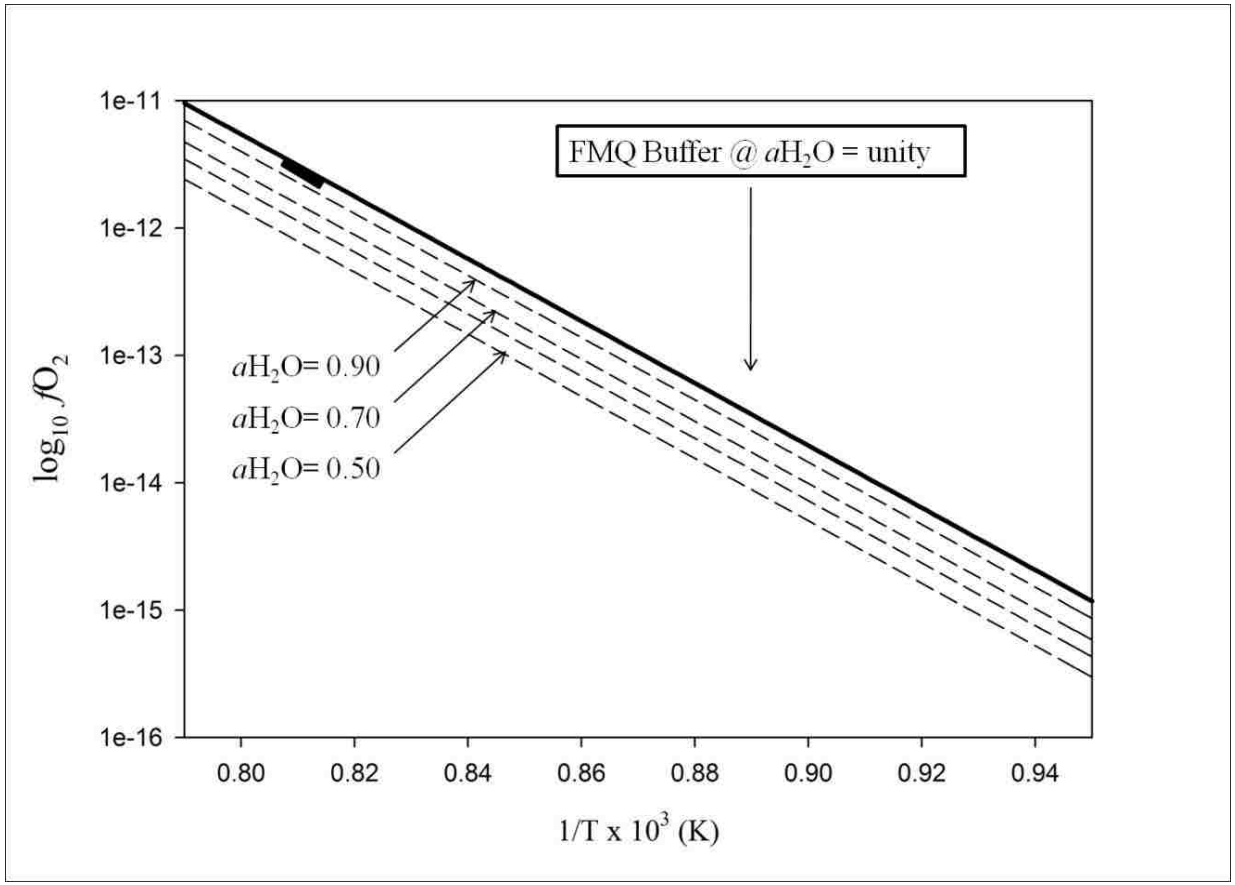

Figure 10. The displacement of the FMQ buffer at reduced water activities. Actual experimental water activities and oxygen fugacity values are marked with the heavy black rectangle.

Table 13. Average composition of the quenched melt. The 1σ standard deviation for the average is contained within parentheses to the right of the average value. The # Analyses indicates the total number of replicate analyses per glass.

Run ID	SiO_2	FeO	K_2O	Na_2O	Al_2O_3	Cl	MgO	TiO_2	CaO	Total	# Analyses
TZM 11	55.4 (2.07)	4.28 (0.59)	2.16 (0.70)	2.45 (0.14)	15.82 (0.72)	1.50 (0.17)	3.74 (0.49)	0.65 (0.08)	7.53 (1.0)	92.88 (0.29)	14
TZM 12	53.88 (0.80)	3.61 (0.22)	2.50 (0.21)	2.20 (0.10)	15.30 (1.10)	1.78 (0.08)	3.70 (0.24)	0.49 (0.08)	7.63 (0.71)	91.90 (0.64)	10
TZM 20	53.85 (2.24)	5.25 (1.04)	2.32 (0.48)	2.56 (0.21)	15.57 (0.67)	1.20 (0.09)	4.03 (0.43)	0.64 (0.10)	7.38 (0.86)	92.65 (0.30)	13
TZM 21	54.65 (0.68)	4.12 (0.09)	2.01 (0.35)	2.47 (0.13)	15.80 (0.56)	1.33 (0.18)	3.94 (0.16)	0.64 (0.08)	7.90 (0.56)	92.76 (0.42)	19
TZM 23	54.95 (3.70)	5.70 (2.39)	2.19 (0.98)	2.42 (0.26)	14.77 (0.77)	1.27 (0.15)	3.93 (0.57)	0.62 (0.09)	7.59 (1.59)	93.32 (0.60)	13
TZM 30	54.13 (0.61)	5.32 (0.50)	2.50 (0.18)	2.34 (0.08)	16.54 (0.17)	1.29 (0.09)	3.16 (0.11)	0.77 (0.11)	7.10 (0.26)	92.98 (0.48)	14
TZM 31	55.30 (4.33)	5.16 (2.36)	2.34 (0.89)	2.34 (0.33)	14.65 (0.99)	1.24 (0.24)	3.70 (0.71)	0.65 (0.13)	7.35 (1.73)	92.71 (0.53)	13
IHPV 1	51.64 (0.33)	3.70 (0.12)	2.66 (0.08)	2.86 (0.12)	17.36 (0.13)	1.93 (0.07)	3.91 (0.10)	0.68 (0.05)	8.32 (0.11)	92.81 (0.51)	16
IHPV 1-1	51.10 (0.27)	4.41 (0.11)	2.64 (0.05)	2.65 (0.09)	17.30 (0.15)	2.12 (0.10)	3.99 (0.12)	0.67 (0.08)	8.44 (0.08)	93.58 (0.39)	14
IHPV 1-2	51.52 (0.22)	4.27 (0.11)	2.55 (0.05)	2.51 (0.10)	17.04 (0.10)	1.98 (0.09)	4.10 (0.09)	0.66 (0.11)	8.50 (0.13)	92.92 (0.30)	15

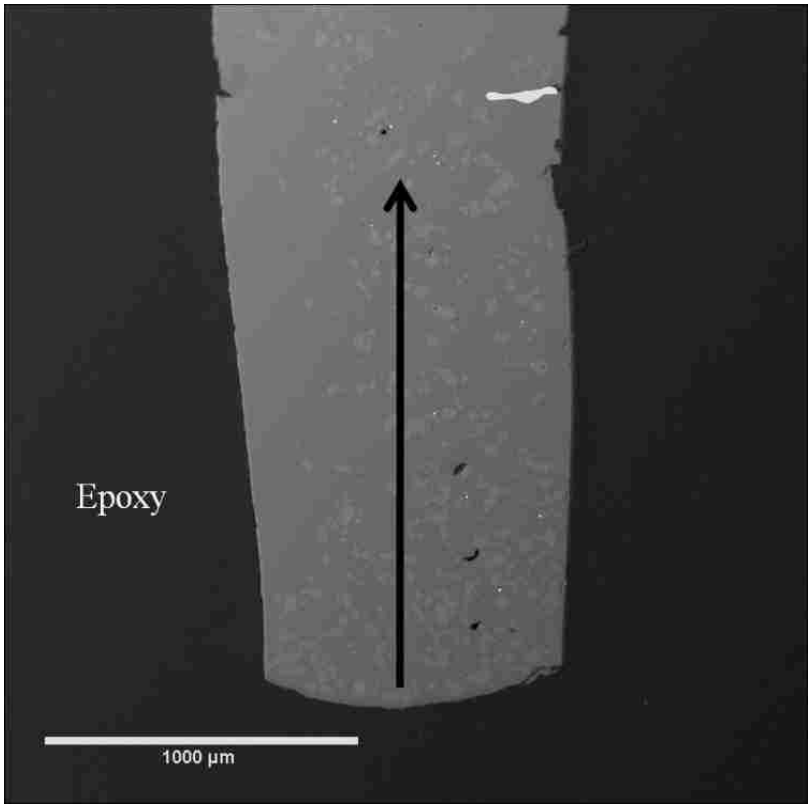

Figure 11. Backscattered electron image of experimental glass cylinder recovered from IHPV1-1. The arrow represents the typical EPMA transect from the base of the melt column to the fluid-melt interface, the latter is not visible in this photomicrograph. The bright spots represent the large metallic nuggets discussed in the text.

Table 14. EPMA analytical transect for IHPV1-2. The run time was 142 hours.

SiO_2	FeO	K_2O	Na_2O	Al_2O_3	Cl	MgO	TiO_2	CaO	Total
51.64	4.40	2.68	2.73	17.08	1.93	3.96	0.77	8.52	93.33
51.48	4.40	2.60	2.80	17.10	1.93	4.13	0.85	8.41	93.35
51.86	4.42	2.68	2.59	17.25	1.81	4.13	0.59	8.23	93.38
51.27	4.44	2.67	2.85	17.03	2.02	4.23	0.64	8.32	93.13
51.34	4.25	2.66	2.63	17.03	2.02	4.29	0.66	8.58	93.16
51.61	4.25	2.57	2.59	16.99	1.96	4.14	0.71	8.55	93.14
51.14	4.25	2.60	2.56	16.88	1.88	4.15	0.77	8.78	92.63
51.48	4.06	2.56	2.64	17.12	2.12	4.05	0.65	8.41	92.76
51.73	4.23	2.53	2.57	17.10	2.03	3.94	0.65	8.61	93.03
51.43	4.09	2.52	2.70	17.11	2.04	4.10	0.61	8.60	92.90
51.40	4.27	2.64	2.49	16.93	1.97	4.16	0.66	8.51	92.74
51.49	**4.28**	**2.61**	**2.65**	**17.06**	**1.97**	**4.12**	**0.69**	**8.50**	**93.05**
0.21	**0.13**	**0.06**	**0.11**	**0.10**	**0.09**	**0.10**	**0.08**	**0.15**	**0.26**

Table 15. EPMA analytical transect for TZM 21. The run time was 25 hours.

SiO_2	FeO	K_2O	Na_2O	Al_2O_3	Cl	MgO	TiO_2	CaO	Total
53.62	4.65	1.58	2.44	16.01	1.49	4.03	0.75	8.16	92.54
54.02	4.41	1.73	2.39	16.23	1.48	4.08	0.55	8.07	92.85
53.40	4.73	1.60	2.26	16.56	1.41	4.13	0.49	8.43	92.89
53.86	4.58	2.14	2.40	16.29	1.59	4.11	0.61	7.72	93.11
53.36	4.67	1.67	2.47	16.45	1.58	4.02	0.57	8.19	92.76
53.32	4.53	1.70	2.30	16.64	1.57	3.93	0.75	8.31	92.87
56.31	4.21	2.63	2.56	15.03	1.15	3.39	0.67	6.76	92.60
57.22	3.66	3.00	2.52	15.42	1.32	3.24	0.61	6.47	93.26
57.59	3.68	3.04	2.43	15.17	1.49	3.20	0.69	6.19	93.15
58.51	2.76	3.53	2.62	14.57	1.45	2.78	0.62	5.65	92.20
59.32	2.45	3.58	2.74	14.19	1.47	2.91	0.59	5.39	92.37
55.50	**4.03**	**2.38**	**2.47**	**15.69**	**1.45**	**3.62**	**0.63**	**7.21**	**92.78**
2.32	**0.80**	**0.80**	**0.14**	**0.85**	**0.13**	**0.52**	**0.08**	**1.14**	**0.33**

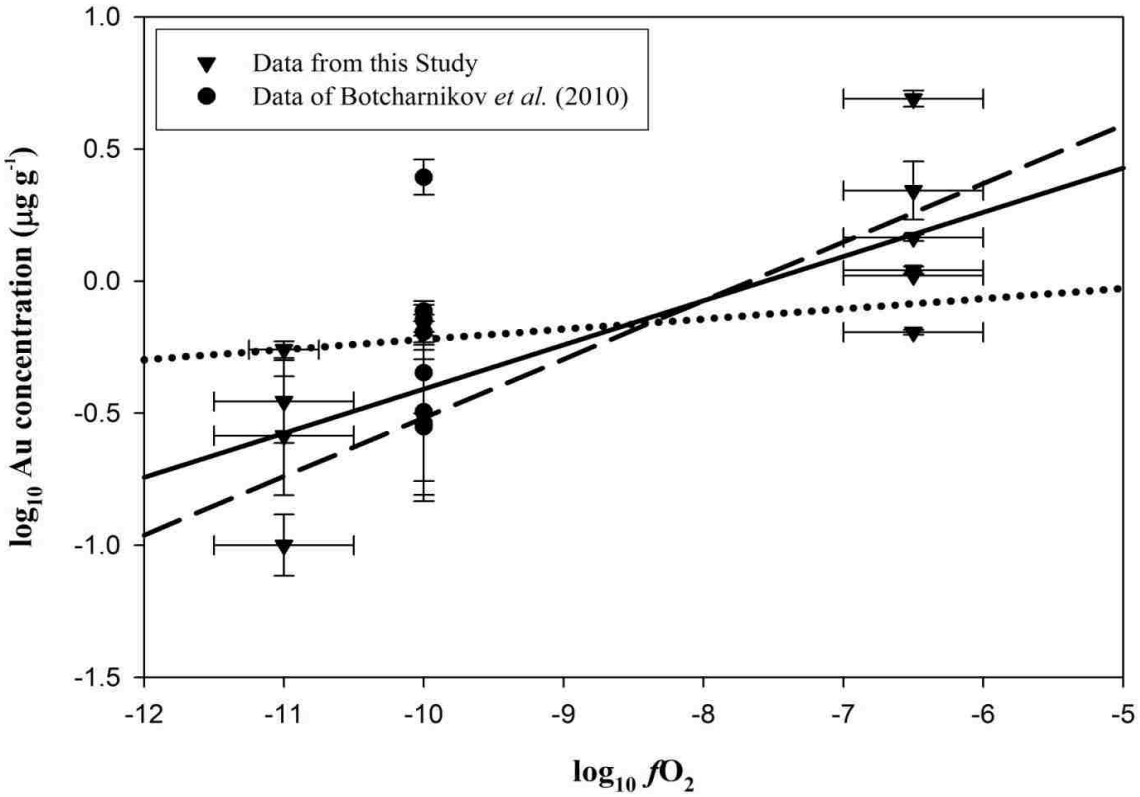

Figure 12. Au concentration as a function of oxygen fugacity. Heavy dashed line represents the theoretical Au solubility slope of 0.25; solid line is the linear regression (m = 0.17) from all of the data in the current study; the light dashed line is the linear regression of the three long duration experiments (m=0.12) The filled circles are all of the Au solubility data from Botcharnikov et al. (in press) who report that the increasing Au concentration in their study corresponds to increasing chlorine and sulfur activities in the melt.

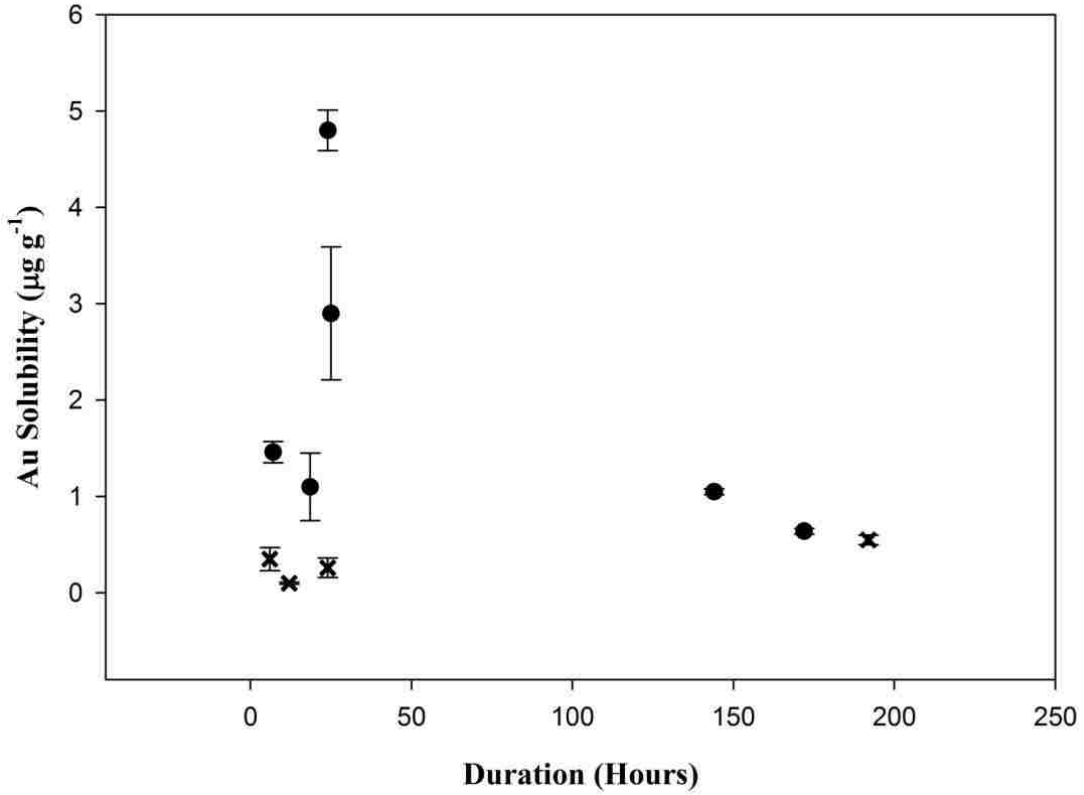

Figure 13. Au concentration as a function of run duration. High Au concentrations in the short duration experiments may reflect the higher Au solubility in relatively oxidizing conditions in the first few hours of the experiments run at the intrinsic oxidation state (i.e., FMQ +4.5). The "x's" represent reducing runs and the "circles" represent oxidizing runs.

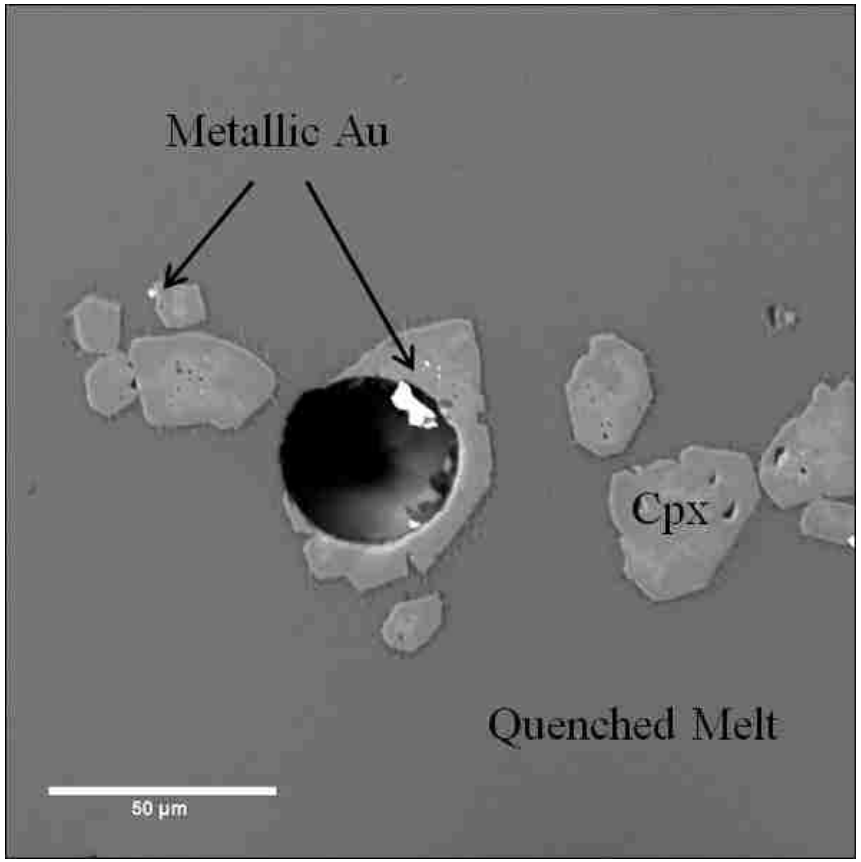

Figure 14. Backscattered electron image of a LA-ICP-MS crater which contains a large metallic Au particle and a second glass-hosted gold nugget at the interface between melt and cpx.

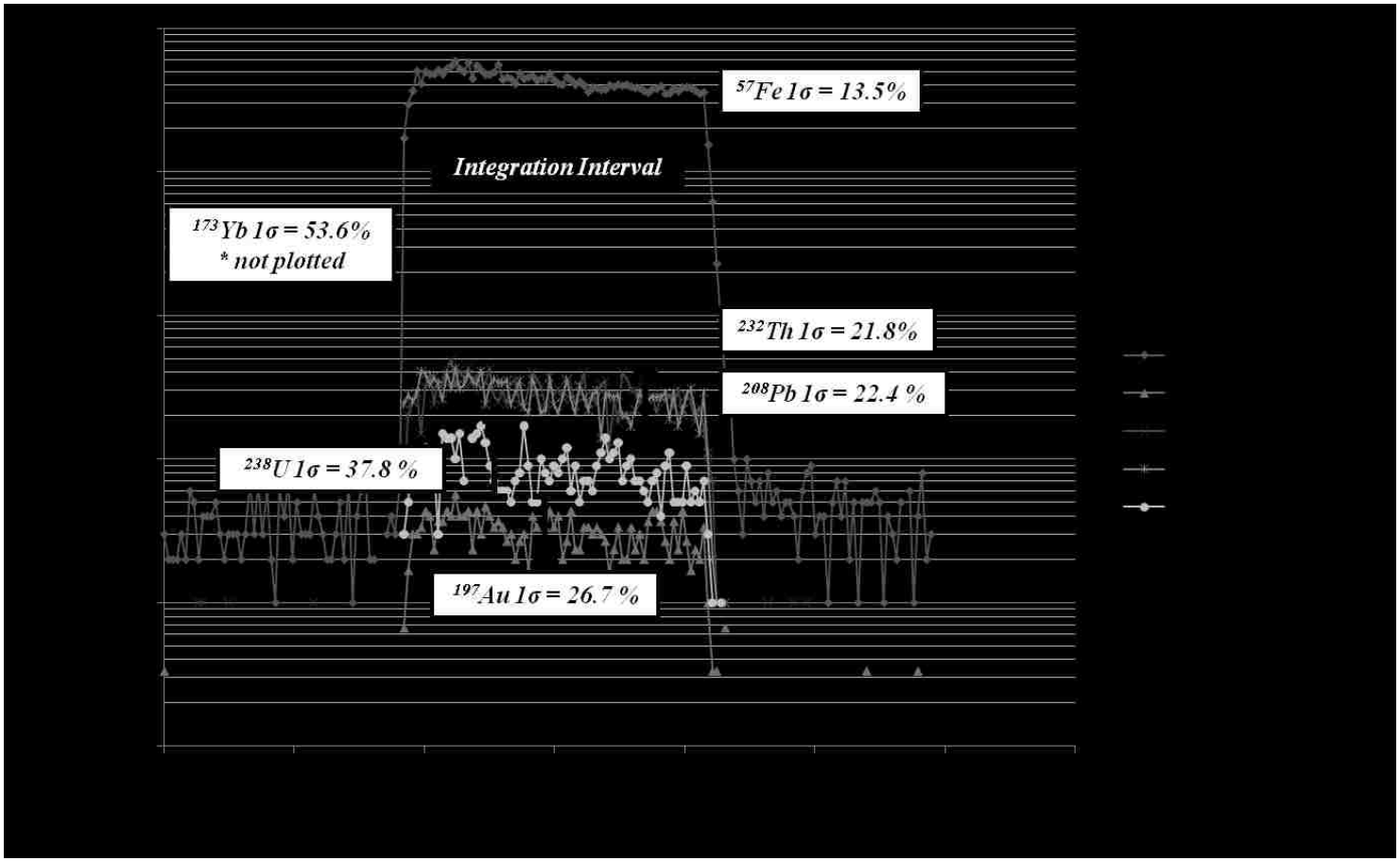

Figure 15. LA-ICP-MS signal from IHPV1-1. Note the similarity in the one- sigma standard deviations for the count rates of Au, Th, Pb, and U.

CHAPTER FOUR

EXPERIMENTAL EVIDENCE FOR THE ALTERATION OF THE $Fe^{3+}/\sum Fe$ OF MAFIC MASMAS BY THE DEGASSING OF CHLORIDE RICH VOLATILES

Abstract

The temporal evolution of the redox conditions experienced by degassing magmas in the shallow subsurface has important petrologic implications for magmatic phase equilibria. We present new experimental data that suggest that a chloride-bearing magmatic aqueous volatile phase may affect the concentration and activity of ferrous iron in silicate liquids via the preferential dissolution of ferrous iron into an aqueous fluid. The data are consistent with a model wherein the exsolution of a chlorine-bearing, aqueous fluid from the melt may be expected to modify the MgO to FeO ratio of the residual degassed melt. Degassing-induced alteration of the melt composition may cryptically affect the identity and compositions of late crystallizing silicate and oxide phases. The overall magnitude of the reduction in the ferrous iron content of the residual melt is controlled by the fluid to melt ratio. As such, passive degassing over geologically plausible, protracted periods of time has the potential to extract significant quantities of divalent iron, hence resulting in a residual melt depleted in FeO relative to Fe_2O_3. Evidence for increased $Fe^{3}+/\sum Fe$ ratios in chloride-degassed magmas should be manifested in the compositions of phases sensitive to the FeO content and fO_2 of the melt. Additionally, the experimentally determined aqueous fluid-melt partition coefficients for the bulk iron content of the melt (expressed as Fe^{total}) range from D = 0.54 to D = 0.39.

Introduction

The oxidation states of most natural basaltic and andesitic liquids range from ΔFMQ-1 to ΔFMQ+4 (Carmichael, 1991). Prevailing redox conditions in magmatic systems exert a strong influence on magmatic phase equilibria, liquid lines of decent, and the speciation of redox sensitive volatiles (Berndt et al., 2005; Gaillard and Scaillet, 2009; Mavrogenes and O'Neill, 1999; Scaillet and Evans, 1999; Scaillet and Macdonald, 2006; Scaillet and Pichavant, 2004). Additionally, the relative proportion of ferric and ferrous iron and their respective coordination states profoundly affect melt density and viscosity (Dingwell and Virgo, 1988; Lange and Carmichael, 1987). Recent numerical modeling efforts suggest that the oxygen fugacity (fO_2) of silicate magmas is not static, but rather may evolve rapidly in shallow-level degassing volcanic systems (Burgisser and Scaillet, 2007). Dynamic changes in magma redox conditions have important implications for modeling volcanic processes, as well as the correct petrologic interpretation of iron bearing phases crystallizing during volatile exsolution.

The previously proposed mechanisms for degassing-induced magma oxidation rely upon the removal of hydrogen from the melt as either H_2S or HCl (Burgisser and Scaillet, 2007; Candela, 1986). In the current study we present a new, geologically plausible oxidation mechanism for the late stage degassing of mafic magmas. The exsolution of a chloride-rich aqueous fluid from the melt may alter the $Fe^{3+}/\sum Fe$ ratio of the silicate melt by preferentially scavenging divalent iron from the melt. This behavior is expected to cause a precipitous decrease in the concentration and activity of FeO in the melt, while simultaneously altering the equilibrium composition of Fe-bearing phases (e.g., orthopyroxene, clinopyroxene, and olivine) crystallizing from the residual liquid.

Moreover, the new data indicate that Cl-bearing magmatic-hydrothermal fluids have the capacity to contain and transport significant quantities of dissolved iron sourced from silicate melts. This conclusion is consistent with the results from earlier studies of chlorine-rich, iron-bearing aqueous-fluid inclusions from natural magmatic hydrothermal systems as well as thermodynamic modeling efforts concentrated on silicate-fluid mass transfer processes (Dolejš and Wagner, 2007; Koděr et al., 1998; Kodera et al., 2003; Whitney et al., 1985). The mechanism of preferential dissolution of ferrous iron into a magmatic volatile phase(s) is proposed not as a mutually exclusive alternative to hydrogen based auto-oxidation processes, but rather as a complimentary process that may enhance the efficiency of magma oxidation as well as decreasing the total iron content of the residual silicate melt.

Experimental and Analytical Techniques

Experiments were performed at 200 ± 0.05 MPa and 1000 ±10 °C in a titanium-zirconium-molybdenum (TZM) pressure vessel at the University of Nevada, Las Vegas or an H_2 membrane equipped internally heated pressure vessel (IHPV) at the American Museum of Natural History. Experimental fO_2 values were varied at two oxidation states: FMQ+0 (±0.5) to FMQ+4.5 (±0.5). Starting materials consisted of a milled dolerite powder from the lower chilled margin of the Ferrar Dolerite, McMurdo Dry Valleys, Antarctica (Boudreau and Simon, 2007) and an equimolar NaCl-KCl-HCl aqueous solution with a total molar chlorine concentration of 0.17. The phase assemblage contained in the chilled margin dolerite has been investigated petrographically by Hersum et al. (2007) and contains orthopyroxene, clinopyroxene, plagioclase, and a

quantity of Fe-Ti oxide phases; the starting material free was of olivine. The mass ratio of solution to dolerite powder was fixed at 3:1, in order to impart a maximum compositional change in the silicate material. Phase relations predicted from the equations of Driesner and Heinrich (2007) for analog H_2O-NaCl fluids indicate that a single-phase, supercritical fluid is stable at run conditions. Experiments were run in a double-capsule configuration where a mechanically open inner capsule was packed with dolerite powder and loaded into a larger outer capsule containing the solution. This experimental design limited the interaction of the aqueous fluid with the silicate material to the top surface of the melt column; i.e., at a single fluid melt interface at the top of the melt column. Thus, crystalline material contained in the interior of the melt did not interact directly with the fluid phase.

Experimental details, including run duration, run fO_2, are provided in Table 16 along with a list of recovered solid experimental run products which consisted of quenched melt (i.e., glass), clinopyroxene, olivine, and magnetite. All glasses and crystalline material were analyzed by using wavelength dispersive spectrometry (WDS) with a four spectrometer JEOL 8900 electron microprobe at the University of Nevada, Las Vegas. Qualitative phase identification and the documentation of textural relationships were accomplished by using backscattered electron imaging (BSE) and energy dispersive spectrometry (EDS). Laser ablation inductively coupled plasma mass spectrometry (LA-ICP-MS) analyses were performed on the glass and crystalline silicate phases at the Institute for Isotopengeologie and Mineral Rohstoffe at ETH in Zurich, Switzerland.

Mass balance calculations utilizing LA-ICP-MS trace element data were employed to determine the mass ratios of melt to crystalline material, and to determine the

composition of the aqueous phase in the long duration (steady state) experiments. Iron loss to Au capsules has been demonstrated to be negligible for basaltic liquids at fO_2 values of FMQ (Botcharnikov et al, 2007).

Stable Phase Assemblages, Phase Compositions and Their Temporal Evolution

The phase assemblages observed in the quenched run products were observed to change as a function of both the experimentally imposed fO_2 and the run duration. Experiments conducted at ΔFMQ+4.5 contain a phase assemblage consisting of hydrous silicate melt, clinopyroxene, ± magnetite, ± olivine, ± plagioclase, and a supercritical aqueous fluid. Experiments less than 24 hours in duration contained magnetite in the absence of olivine, whereas long duration experiments of 172 and 144 hours contained olivine ranging in composition from Fo_{92} to Fo_{95}, but no magnetite.

Experiments conducted at reducing fO_2 values of ΔFMQ+0 (±0.5 log units) contained a phase assemblage consisting of hydrous silicate melt, clinopyroxene, olivine, and supercritical aqueous fluid. The composition of olivine in these experiments evolved substantially with increasing run time, from Fo_{77} at 24 hours to Fo_{92} at 172 hours. Figure 16 contains annotated BSE images illustrating the different phase assemblages.

The ferrous iron content of the experimental melts was calculated by using the algorithm of Kress and Carmichael (1992) in conjunction with the EPMA determined bulk iron concentration of the melt. The calculated FeO content was then used to calculate the Mg-Fe partition coefficients of olivine-melt pairs. Calculated partition coefficient values for olivine-melt pairs from short duration experiments range from K_d =

0.29 to 0.32 at fO_2 = ΔFMQ+0. The experimentally determined equilibrium K_d value is calculated to be 0.30 for our experimental conditions. Thus, the K_d values calculated from our experimental data indicate that the composition of the early olivine (Fo_{77}) is in equilibrium with respect to the melt composition in these experiments. The slight positive deviation of the calculated K_d value in some olivine-melt pairs may arise from small errors in the calculated FeO concentrations of the melt. Olivine compositions are generally homogenous within a single grain, but display considerable intra-grain variability in all long duration of experiments.

Clinopyroxene recovered from all runs displays subtle core to rim zoning with respect to Mg, Fe, Ca, and Al. Zoning patterns observed in the pyroxenes are defined by Fe- and Al-rich cores which are rimmed with Ca- and Mg-rich overgrowths (Figure 17). The cores of zoned clinopyroxene crystals in the oxidizing experiments often contain magnetite inclusions, even in long duration, high fO_2 experiments where magnetite no longer exists as a stable liquidus phase. The size of all crystalline material coarsens with increasing run time. The euhedral morphology observed in all crystalline material indicates that no significant crystallization occurred on quench.

Interpretation and Discussion of Experimental Results

Mass balance calculations indicate that a substantial quantity of iron was lost from the melt to the fluid during both the both oxidizing and reducing experiments. The mass transfer of iron from the melt to the fluid is facilitated by the presence of chlorine and the stability of iron-chloride in the aqueous fluid. Iron loss from the melt to the fluid phase is manifested in three distinct ways: 1) the time dependent resorption of magnetite into the

melt coupled with the stabilization of olivine in experiments at fO_2 = QFM+4.5; 2) the time dependent MgO enrichment of olivine in experiments at fO_2 = QFM+0; and 3) the Mg-Fe compositional zoning preserved in the clinopyroxene of long duration experiments.

The effects of iron loss to the fluid in the oxidizing experiments are twofold: magnetite is destabilized as a liquidus phase, and conversely MgO rich olivine is stabilized as a liquidus phase. The presence of magnetite in the high fO_2 experiments initially acts to buffer the activities of FeO and Fe_2O_3 in the liquid. Progressive removal of iron from the melt, via scavenging by the fluid, caused the magnetite to dissolve incrementally back into the melt. This process of magnetite resorption fixed the composition of the melt on the magnetite saturation curve, until all of the magnetite was consumed. Upon the exhaustion of available magnetite, the iron content of the melt was no longer buffered by the presence of crystalline Fe_3O_4 and the total iron content of the melt decreased until the aqueous phase fluid became saturated with Fe, as the stable $FeCl_2$ species. The fluid modified MgO/FeO ratio of the melt experiments stabilized Mg-rich olivine as a liquidus phase.

The reduction in the FeO content of the melt is also manifested in the shifting olivine-melt equilibrium observed in the experiments at fO_2 = QFM+0. The composition of the olivine recovered from these experiments serves as a useful sensitive indicator of the activity of FeO in the melt (Berndt et al., 2005; Mysen, 2006; Roeder and Emslie, 1970). Differences between the olivine compositions in short vs. long duration runs, e.g., Fo_{77} and Fo_{92} from runs of 24 and 192 hours, respectively, serve as evidence of the temporal variation in the FeO content of the melt. The large increase in the Mg_2SiO_4

content of the olivine implies that the activity of FeO in the melt decreased relative to the activities of Fe_2O_3 and MgO in the melt. The continuous removal of ferrous iron from the melt to the fluid forced the equilibrium composition of the stable crystalline material to adjust coevally with the evolving melt composition.

The preserved zoning profiles in clinopyroxene (Figure 17) offer additional evidence for the effect of degassing on both the evolving melt composition and the Fe/Mg ratio of ferromagnesian silicates. The relict cores of the clinopyroxene crystals represent an iron-rich pyroxene that crystallized before the fluid could significantly modify the melt composition. The Mg-rich rims overgrowing the Fe-enriched cores chronicle the protracted FeO depletion of the melt; we tacitly assume that Fe^{3+} comprises a negligible contribution to the total Fe content of the pyroxenes. Magnetite inclusions observed in early-nucleated clinopyroxene crystals may continuously supply iron to cores of the crystals during growth of the crystal, thus preserving the zoning profiles well past the point at which diffusive equilibration should have homogenized pyroxene compositions.

We invoke the chloride-bearing fluid as the agent responsible for the decreased FeO content of the melt, hence varying melt composition, and the dynamically changing phase assemblages, i.e., the compositional zoning in clinopyroxene. We propose the following equilibrium to represent the scavenging of ferrous iron by the aqueous fluid from the silicate melt:

Eq. 19 $$2HCl^{fluid} + FeO^{melt} = H_2O^{melt} + FeCl_2$$

The presence of Fe^{2+} as the only valence state of iron is based upon the conclusions from previous studies of iron solubility in chloride-bearing hydrothermal fluids that demonstrate that $FeCl_2$ is the stable iron species across a wide range of sub-solidus to

magmatic conditions (Chou and Eugster, 1977; Simon et al., 2004; Wykes et al., 2008). Mass balance calculations from the new experiments indicate that HCl was the primary fluid species involved in the exchange reactions. The compositional trends of the olivine and resorption of magnetite observed in this study are consistent with the proposed reactions dominantly removing Fe^{2+} from the melt.

If the fugacities of HCl and H_2O are fixed, Eq.19 may be rearranged to express the activity of ferrous iron in the melt as a function of the molality of $FeCl_2$ in the aqueous phase and the equilibrium constant of Eq. 19

Eq. 20 $$a\text{FeO} = m\text{FeCl}_2 * \text{K}_2^{-1}$$

Magmatic fO_2 in the absence of large quantities of other redox sensitive elements is defined by the homogeneous equilibrium:

Eq. 21 $$2\text{FeO}^{\text{melt}} + 0.5\text{O}_2 = \text{Fe}_2\text{O}_3{}^{\text{melt}}$$

which may be rearranged to the form:

Eq. 22 $$fO_2 = \left(\frac{a\text{Fe}_2\text{O}_3}{a\text{FeO}} * \text{K}^{-1}\right)^2$$

Following from the relationships above, the fO_2 of iron-bearing magmas is intrinsically related to the activities of both ferric and ferrous iron in the melt. As such, any reduction in the mole fraction or activity of the ferrous component of the silicate liquid will increase the fO_2 of the magmatic system. Combining Eqns. 20 and 22 yields and expression defining the oxygen fugacity of the melt in the presence of an aqueous fluid at constant fHCl as follows:

Eq. 23 $$fO_2 = \left(\frac{a\text{Fe}_2\text{O}_3 \cdot \text{K}_2}{m\text{FeCl}_2} * \text{K}_4^{-1}\right)^2$$

From this expression we conclude that the fO_2 of the melt is dependent upon the fluid modified FeO activity of the melt. We calculate iron (as $FeCl_2$) concentration in the

aqueous fluids for the long duration experiment at fO_2 = QFM+0 to be 3.5 ± 0.2 wt % and the long duration experiments at fO_2 = QFM+4.5 to be 3.2 ± 0.2 wt %. According to Eq. 21 the strikingly similar $FeCl_2$ concentrations of both the oxidizing and reducing experiments indicate that the activity of FeO in the oxidizing melts displays a significant positive deviation from ideality. This observation is consistent the experimentally determined FeO activity coefficients of Gaillard et al (2004); activity coefficient values from this study intermediate melts at fO_2= FMQ+4 are generally $\gamma > 1.0$ (estimated value of $\gamma = 1.5$). Positive deviations of the aFeO of the melt from ideality suggest that the reaction in Eq. 19 will continue to run, despite the relatively low concentrations of FeO in oxidized melts.

The solubility of Fe in chloride aqueous phases is expected to be a function of fluid density as well as total chloride content of the aqueous magmatic volatile phase. Therefore, the simple Nernst-type partition coefficient for Fe between coexisting aqueous fluid(s) and melt should vary not only as a function of a_{FeO} of the melt, but also as a function of fluid density and chloride concentration of the aqueous fluid. More experimental data are required to fully model the effects of HCl-bearing fluids on the ferrous iron content of silicate melts in P-T space.

Implications for Phase Equilibria in Natural Volcanic Systems

Anomalously Mg-rich olivine phenocrysts (Fo_{96}) have been documented in the basaltic ejecta from Stromboli Volcano, Italy (Cortes et al, 2006). The bulk iron content of these magmas is relatively low for basaltic liquids, ranging from 6-8 wt % FeO. We

hypothesize that passive open-system degassing of a Cl-rich aqueous volatile phase may have contributed to the formation of the Mg-rich olivine by progressively removing ferrous iron from the residual melt. Such a scenario should not only lower the bulk iron content of the melt, but also increase the $Fe^{3+}/\sum Fe$ ratio of the silicate liquid. Cortes et al (2006) concluded that the degassing of reduced sulfur species caused the nearly wholesale oxidation of ferrous iron in the melt to the ferric oxidation state. The mechanism we propose likely works in concert with H_2S degassing to further enhance the oxidizing potential of the fluid phase. However, given the relatively low iron scavenging efficiency of the fluid phase, the oxidizing effects of fluid metasomatism are likely limited to aliquots of magma that encounter large volumes of the oxidizing fluids (i.e., a high fluid/rock ratio). Passively degassing lava lakes, magma foams at upper portions of volcanic conduits, and distal portions of degassing sills (relative to the center) are prime candidates for locations that may experience relatively large fluid to melt ratios. We also caution that the equilibrium constant governing the mass transfer of iron form the melt to the fluid may vary dynamically with density and composition of the fluid phase; thus, the use of a static value of the fluid-melt partition coefficient for the purpose of modeling bulk iron mass transfer may yield inaccurate results.

Late stage magmatic oxidation has also been suggested to play a major role in the evolution of magmatic-hydrothermal ore deposits. Halter et al. (2005) hypothesize that late stage magma oxidation is responsible for the destabilization of metal-rich crystalline and liquid sulfides, resulting in the availability of ore metals and sulfur to be scavenged by magmatic aqueous fluids. Considering the ubiquitous presence, and critical importance in terms of metal transport, of a Cl-bearing aqueous phase in all porphyry-

type and high-sulfidation ore deposits, the modification of the ferrous iron content of the melt by a Cl-rich fluid, as observed in the present study, is a geologically plausible oxidation mechanism that is likely a salient feature of all magmatic-hydrothermal systems. In the case of sulfide saturated magmas, the fluid induced decrease in the activity of ferrous iron in the melt will also alter the stable sulfide phase assemblage. The composition of stable liquid Cu-Fe sulfide and mono-sulfide solid solutions will be driven away from their iron rich end members or destabilized altogether. Late stage chloride degassing is a parsimonious explanation for the destabilization of sulfide phases. Further, the new experimental data have important implications for the development of large-scale, iron-rich ore bodies such as Kiruna-type ore deposits where the nearly characteristic presence of the light rare earth element (LREE) enrichment is also consistent with aqueous-fluid transport of iron and the LREE (cf. Reed et al., 2000. Future experiments are planned to constrain the ability of magmatic-aqueous fluid to scavenge and transport the REE and other prominent elements in these types of iron-rich deposits.

Table 16. Recovered Phase Assemblages by Experiment

Run	Duration (Hrs)	fO_2	Phase Assemblage
TZM 12	24	FMQ + 4.5 ± 0.5	Melt; Mt; Cpx; Plg
TZM 20	18.5	FMQ + 4.5 ± 0.5	Melt, Mt, Cpx, Plg
IHPV 1-1	172	FMQ + 4.5 ± 0.5	Melt; Ol(Fo_{94}); Cpx
IHPV 1-2	144	FMQ + 4.5 ± 0.5	Melt; Ol(Fo_{92}); Cpx
TZM 23	6	FMQ ± 0.5	Melt; Ol(Fo_{77}); Cpx
TZM 31	24	FMQ ± 0.5	Melt; Ol(Fo_{78}); Cpx
IHPV 1	192	FMQ ± 0.1	Melt; Ol(Fo_{91}); Cpx

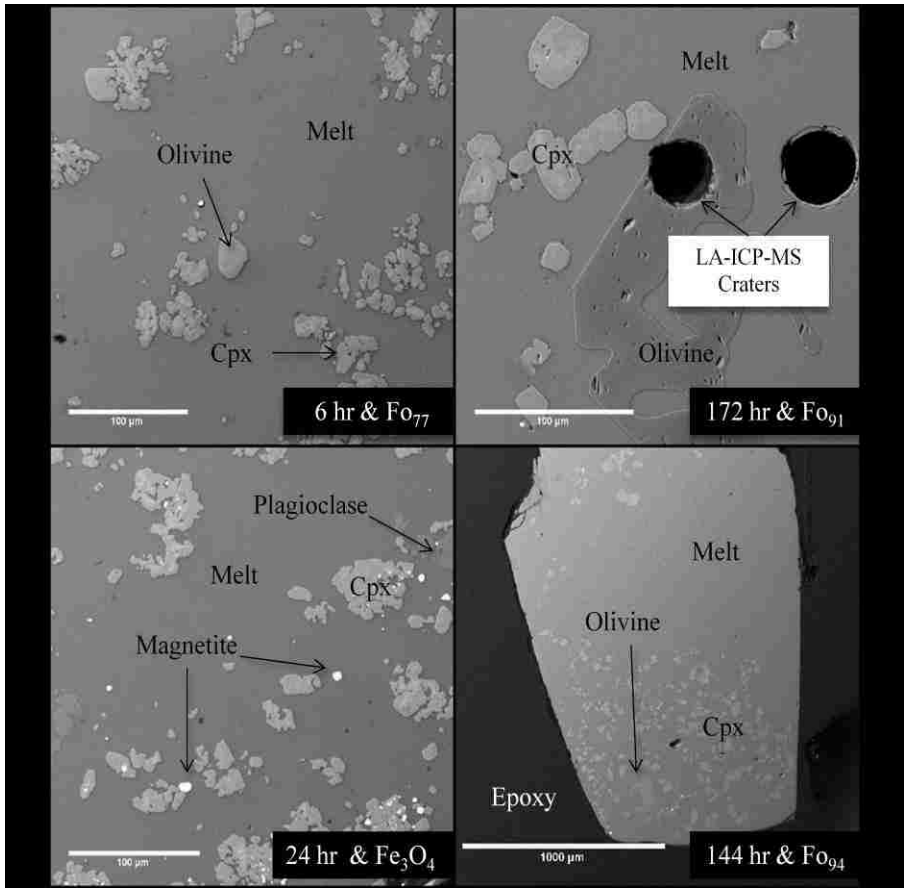

Figure 16. Backscattered electron images of the differing, recovered stable phase assemblages. The box in the lower corner indicates the composition of the recovered olivine as well as the run time.

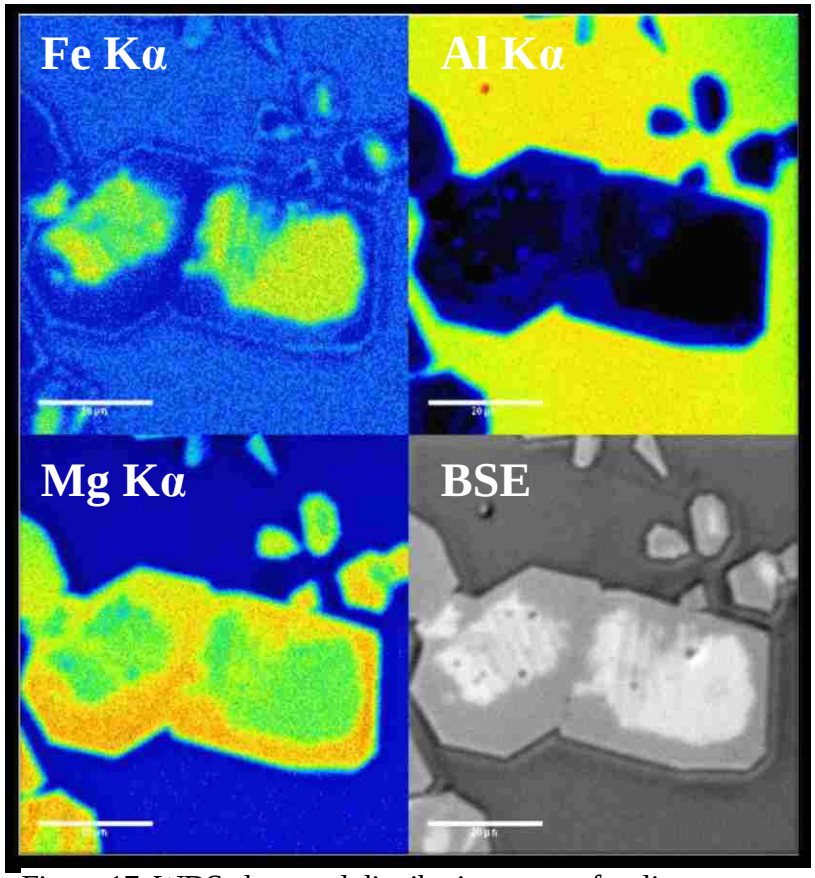

Figure 17. WDS elemental distribution maps of a clinopyroxene crystal displaying compositional Zoning with respect to Mg, Fe, and Al.

REFERENCES CITED

Audétat, A., Günther, D., and Heinrich, C. (1998) Formation of a magmatic-hydrothermal ore deposit: insights with LA-ICP-MS analysis of fluid inclusions. Science 279, p. 2091.

Auge T. M., Petrunov R. and Bailly L. (2005) On the origin of the PGE mineralization in the elatsite porphyry Cu–Au deposit, Bulgaria: comparison with the Baula–Nuasahi complex, India, and other alkaline PGE-rich porphyries. Can. Mineral. 43, p. 1352.

Ballhaus C. and Ulmer P. (1995) Platinum-group elements in the Merensky reef: II. Experimental solubilities of platinum and palladium in Fe1-xS from 950 to 450 C under controlled *f*S2 and *f*H2. Geochim. Cosmochim. Acta 59, p. 4888.

Bell, A., Simon, A., and Guillong, M., 2009, Experimental constraints on Pt, Pd and Au partitioning and fractionation in silicate melt–sulfide–oxide–aqueous fluid systems at 800° C, 150MPa and variable sulfur fugacity: Geochim. Cosmochim. Acta 73, p. 5778.

Berndt, J., Koepke, J., and Holtz, F. (2005) An experimental investigation of the influence of water and oxygen fugacity on differentiation of MORB at 200 MPa: J. Petrol. 46, p. 135.

Blaine F. A., Linnen R. L., Holtz F. and Brugmann G. E. (2005) Platinum solubility in a haplobasaltic melt at 1250 C and 0.2 GPa: the effect of water content and oxygen fugacity. Geochim. Cosmochim. Acta 69, p. 1273.

Bodnar R. J., Burnham C. W. and Sterner S. M. (1985) Synthetic\ fluid inclusions in natural quartz. III. Determination of phase equilibrium properties in the system H2O–NaCl to 1000 C and 1500 bars. Geochim. Cosmochim. Acta 49, p. 1873.

Borisov, A., and Palme, H. (1996) Experimental determination of the solubility of Au in silicate melts: Mineralogy and Petrology 56, p. 312.

Borisov A., and Palme H., (1997) Experimental determination of the solubility of platinum in silicate melts. Geochim. Cosmochim. Acta 61, p. 4357.

Borisov , A., and Palme, H. (2000) Solubilities of noble metals in Fe-containing silicate melts as derived from experiments in Fe-free systems: Am. Mineral. 85, p. 1665.

Botcharnikov, R.E., Linnen, R.L. and Holtz, R (2010) Solubility of Au in Cl- and S-bearing hydrous silicate melts: Geochim. Cosmochim. Acta, In Press doi:10.1016/j.gca.2009.09.021

Botcharnikov, R.E, Koepke, J., Almeev, R.R., Holtz, F. (2008) Experimental phase relations, mineral-melt equilibria and liquid lines of descent in a hydrous ferrobasalt – Implications for the Skaergaard intrusion and Columbia River flood basalts J. Petrol. 49, p. 1727.

Botcharnikov, R.E., Koepke, J., Holtz, F., McCammon, C., and Wilke, M. (2005) The effect of water activity on the oxidation and structural state of Fe in a ferrobasaltic melt. Geochim. Cosmochim. Acta 69, p. 5071.

Boudreau, A., and Simon, A., 2007, Crystallization and degassing in the Basement Sill, McMurdo Dry Valleys, Antarctica: J. Petrol. 48, p. 1369.

Brenan, J.M., McDonough, W.F., and Ash, R. (2005) An experimental study of the solubility and partitioning of iridium, osmium and gold between olivine and silicate melt: Earth and Planetary Sci. Let. 237, p. 855.

Burgisser, A., and Scaillet, B. (2007) Redox evolution of a degassing magma rising to the surface. Nature 445, p. 194.

Candela, P.A. (1986) The evolution of aqueous vapor from silicate melts: Effect on oxygen fugacity: Geochim. Cosmochim. Acta 50, p. 1205.

Candela P. A. (1991) Physics of aqueous phase exsolution in plutonic environments. Am. Mineral. 76, p. 1081.

Carmichael, I. (1991) The redox states of basic and silicic magmas: a reflection of their source regions? Contrib. Mineral. and Petrol. 106, p. 129.

Carroll M. R. and Rutherford M. J. (1988) Sulfur speciation in hydrous experimental glasses of varying oxidation states. Results from measured wavelength shifts of sulfur X-rays. Am. Mineral. 73, p. 845.

Cassidy K. F., Lang, Jr., Lueck, B. A., Mortensen J. K., Russel J. K., Thompson J. F. H. (1996). Geochemical and isotopic characteristics of Mesozoic alkalic intrusions in the Cordillera of British Columbia: tectonic significance and implications for Cu–Au metallogeny. Geol. Soc. Austral., 13th Australian Geological Convection, Canberra, February, 1996. #41.

Cortes, J., Wilson, M., Condliffe, E., Francalanci, L. (2006) The occurrence of forsterite and highly oxidizing conditions in basaltic lavas from Stomboli Volcano, Italy. J. Petrol. 46, p. 1345.

Chou, I., and Eugster, H. (1977) Solubility of magnetite in supercritical chloride solutions: Am. J. Science 277, p. 1296.

Chou I.-M. (1987). Oxygen buffer hydrogen sensor techniques at elevated pressures and temperatures. In Hydrothermal Experimental Techniques (eds. G. C. Ulmer and H. L. Barnes), p. 61.

Chou I.-M., Sterner S. M. and Pitzer K. S. (1992) Phase relations in the system NaCl

KCl–H2O: IV. Differential thermal analysis of the sylvite liquidus in the KCl–H2O binary, the liquidus in theNaCl–KCl–H2O ternary, and the solidus in the NaCl–KCl binary to 2 kb pressure, and a summary of experimental data for thermodynamic-PTX analysis of solid–liquid equilibria at elevated P–T conditions. Geochim. Cosmochim. Acta 56, p. 2281.

Clemente B., Scaillet B. and Pichavant M. (2004) The solubility of sulphur in rhyolitic melts. J. Petrol. 45, p. 2171.

Cottrell E. and Walker D. (2006) Constraints on core formation from Pt partitioning in mafic silicate liquids at high temperatures. Geochim. Cosmochim. Acta 70, p. 1565.

Dingwell, D., and Virgo, D., 1988, Viscosities of melts in the Na2O-FeO-Fe2O3 SiO2 system and factors controlling relative viscosities of fully polymerized silicate melts Geochim. Cosmochim. Acta 52, p. 395.

Dixon J. E., Clague D. A. and Stolper E. M. (1991) Degassing history of water, sulfur, and carbon in submarine lavas from Kilauea Volcano, Hawaii. J. Geol. 99, p. 371.

Dolejš, D., and Wagner, T., 2007, Thermodynamic modeling of non-ideal mineral–fluid equilibria in the system Si–Al–Fe–Mg–Ca–Na–K–H–O–Cl at elevated temperatures and pressures: Implications for hydrothermal mass transfer in granitic rocks: Geochim. Cosmochim. Acta

Driesner, T., and Heinrich, C. (2007) The system H2O–NaCl. Part I: Correlation formulae for phase relations in temperature–pressure–composition space from 0 to 1000° C, 0 to 5000 bar, and 0 to 1 XNaCl. Geochim. Cosmochim. Acta 71, p. 4880.

Ertel W., O'Neill H., Sylvester P. J. and Dingwell D. B. (1999) Solubilities of Pt and Rh in a haplobasaltic silicate melt at1300 C. Geochim. Cosmochim. Acta 63, p. 2439.

Ertel, W., Walter, M.J., Drake, M.J., and Sylvester, P.J. (2006) Experimental study of platinum solubility in silicate melt to 14 GPa and 2273 K: Implications for accretion and core formation in Earth Geochim. Cosmochim. Acta 70, p. 2591.

Farges F., Neuville D. R. and Brown G. E. (1999) Structural investigation of platinum solubility in silicate glasses. Am. Miner. 84, p. 1562.

Fleet M. E., Crocket J. H. and Stone W. E. (1991) Partitioning of palladium, iridium, and platinum between sulfide liquid and basalt melt: effects of melt composition, concentration, and oxygen fugacity. Geochim. Cosmochim. Acta 55, p. 2545.

Fleet M. E., Crocket J. H., Liu M. and Stone W. E. (1999) Laboratory partitioning of platinum-group elements (PGE) and gold with application to magmatic sulfide-PGE deposits. Lithos 47, p. 127.

Frank M. R., Candela P. A., Piccoli P. M. and Glascock M. D. (2002) Gold solubility, speciation, and partitioning as a function of HCl in the brine-silicate melt-metallic gold system at 800 C and 100 MPa. Geochim. Cosmochim. Acta 66, p. 3719.

Gaillard, F., Scaillet, B., and Pichavant, M. (2002) Kinetics of iron oxidation-reduction in hydrous silicic melts. Am. Mineral. 87, p. 829.

Gaillard, F., Pichavant, M., and Scaillet, B. (2004) Experimental determination of activities of FeO and Fe_2O_3 components in hydrous silicic melts under oxidizing conditions. Geochim. Cosmochim. Acta 67, p. 4389.

Gaillard, F., and Scaillet, B. (2009)The sulfur content of volcanic gases on Mars: Earth and Planetary Sci. Let. 279, p. 34.

Guillong M., Meier D. M., Allan M. M., Heinrich C. A. and Yardley B. (2008) SILLS: A MATLAB-Based Program for the Reduction of Laser Ablation ICP–MS Data of

Homogeneous Materials and Inclusions: Mineralogical Association of Canada Short Course 40. Vancouver, B.C., p. 328.

Guillong M. and Heinrich C. A. (2007) Sensitivity enhancement in laser ablation ICP-MS using small amounts of hydrogen in the carrier gas. J. Anal. Atomic Spectrom. 22, p. 1488.

Halter W. E., Heinrich C. A. and Pettke T. (2005) Magma evolution and the formation of porphyry Cu–Au ore fluids: evidence from silicate and sulfide melt inclusions. Miner. Depos. 39, p. 845.

Hedenquist, J., and Lowenstern, J. (1994) The role of magmas in the formation of hydrothermal ore deposits. Nature 370, p. 519.

Holzheid A. and Lodders K. (2001) Solubility of copper in silicate melts as function of oxygen and sulfur fugacity, temperature, and silicate composition. Geochim. Cosmochim. Acta 65, p. 1933.

Hulbert L. J., Duke J. M., Eckstrand O. R., Lydon J. W. and Scoates R. F. J. (1988) Geological environments of the platinum group elements. Geol. Surv. Canada Open File 1440, p. 148.

Jugo P. J., Candela P. A. and Piccoli P. M. (1999) Magmatic sulfides and Au:Cu ratios in porphyry deposits: an experimental study of copper and gold partitioning at 850 C, 100 MPa in a haplogranitic melt-po-intermediate solid solution-gold metal assemblage, at gas saturation. Lithos 46, p. 573.

Jugo, P., Luth, R., and Richards, J. (2005) Experimental data on the speciation of sulfur as a function of oxygen fugacity in basaltic melts. Geochim. Cosmochim. Acta 69, p. 497.

Koděr, P., Rankin, A.H., and Lexa, J. (1998) Evolution of fluids responsible for iron skarn mineralisation: An example from the Vyhne-Klokoc deposit, Western Carpathians, Slovakia. Mineralogy and Petrology 64, p. 119.

Kodera, P., Murphy, P., and Rankin, A. (2003) Retrograde mineral reactions in saline fluid inclusions: The transformation ferropyrosmalite-clinopyroxene. Am. Mineral 88, p. 151.

Lange, R., and Carmichael, I. (1987) Densities of Na2O-K2O-MgO-FeO-Fe2O3-Al2O3 TiO2-SiO2 liquids: New measurements and derived partial molar properties: Geochim. Cosmochim. Acta 51, p. 2931.

Li C., Ripley E. M. and Mathez E. A. (2003) The effect of S on the partitioning of Ni between olivine and silicate melt in MORB. Chemical Geol. 201, p. 295.

Lynton S. J., Candela P. A. and Piccoli P. M. (1993) An experimental study of the partitioning of copper between pyrrhotite and a high silica rhyolitic melt. Econ. Geol. 88, p. 901.

Matthews, W., Linnen, R., and Guo, Q. (2003) A filler-rod technique for controlling redox conditions in cold-seal pressure vessels. Am. Mineral. 88, p. 701.

Mavrogenes, J.A., and O'Neill, H.S.C. (1999) The relative effects of pressure, temperature and oxygen fugacity on the solubility of sulfide in mafic magmas: Geochim. Cosmochim. Acta. 63, p. 1173.

McMillan P. and Holloway J. (1987) Water solubility in aluminosilicate melts. Contrib. Mineral. and Petrol. 97, p. 320.

Morgan G. B. and London, VI, D. (1996) Optimizing the electron microprobe analysis of hydrous alkali aluminosilicate glasses. Am. Mineral. 81, p. 1176.

Morgan, G., and London, D. (2005) Effect of current density on the electron microprobe analysis of alkali aluminosilicate glasses. Am. Mineral. 90, p. 1131.

Mulja T. and Mitchell R. H. (1991) The Geordie Lake intrusion, Coldwell complex, Ontario: a palladium- and tellurium-rich disseminated sulphide occurrence derived from an evolved tholeiitic magma. Econ. Geol. 86, p. 1050.

Mungall, J.E. (2002) Roasting the mantle: Slab melting and the genesis of major Au and Au-rich Cu deposits. J. Geology 30, p. 915.

Mustard, R., Ulrich, T., Kamenetsky, V., and Mernagh, T. (2006) Gold and metal enrichment in natural granitic melts during fractional crystallization. J. Geology. 34, p. 85.

Mutschler F. E., Griffin M. E., Scott S. D. and Shannon S. S. (1985) Precious metal deposits related to alkaline rocks in the North American Dordillera – an interpretative review. Trans. Geol. Soc. S. Africa 88, p. 355.

Naldrett, A., and Duke, J. (1980) Platinum Metals Magmatic Sulfide Ores: Science, 208, p. 1417.

Mysen, B.O. (2006) Redox equilibria of iron and silicate melt structure: Implications for olivine/melt element partitioning. Geochim. Cosmochim. Acta 70, p. 3121.

Ohnenstetter D. and Watkinson D. H. (1998) Low-temperature evolution of the platinum group mineralogy, Two Duck Lake intrusions, Coldwell Complex, Ontario, Canada. In International Platinum 1998 (eds. N. P. Laveroux and V. V. Dislter). Theophrastus Publishing, St. Petersburg, p. 116.

O'Neill, H., Dingwell, D., Borisov, A., Spettel, B., and Palme, H. (1995) Experimental petrochemistry of some highly siderophile elements at high temperatures, and some

implications for core formation and the mantle's early history. Chem. Geol. 120, p. 255.

O'Neill H. St. C. and Mavrogenes J. A. (2002) The sulfide capacity and the sulfur content at sulfide saturation of silicate melts at 1400 C and 1 bar. J. Petrol. 43, p. 1049.

Peach C. L., Mathez E. A. and Keays R. R. (1990) Sulfide–silicate melt distribution coefficients for noble metals and other chalcophile elements as deduced from MORB implications for partial melting. Chem. Geol. 54, p. 3379

Popp, R., Nagy, K., and Hajash, A. (1984) Semiquantitative control of hydrogen fugacity in rapid-quench hydrothermal vessels. Am. Mineral. 69, p. 557.

Reed, M.J., Candela, P.A. and Piccoli, P.M. (2000) The distribution of rare earth elements between monzogranite melt and the aqueous volatile phase in experimental investigations at 800 ºC and 200 MPa. Contrib. Mineral and Petrol. 140, p. 251.

Righter, K., Humayun, M., and Danielson, L. (2008) Partitioning of palladium at high pressures and temperatures during core formation: Nature Geoscience. 1, p. 321.

Ringwood, A., (1966) Chemical evolution of the terrestrial planets: Geochim. Cosmochim. Acta 30, p. 41.

Scaillet B. and MacDonald R. (2001) Phase reations of peralkaline silicic magmas and petrogenetic implications. J. Petrol. 42, p. 825.

Simon G., Kesler S. E. and Essene E. J. (2000) Gold in porphyry copper deposits: experimental determination of the distribution of gold in the Cu–Fe–S system at 400 to 700 C. Econ. Geol. 95, p. 259.

Scaillet, B., and Evans, B. (1999) The 15 June 1991 eruption of Mount Pinatubo. I. Phase

equilibria and pre-eruption P-T-fO2-fH2O conditions of the dacite magma. J. Petrol. 40, p. 381.

Scaillet, B., and Macdonald, R. (2006) Experimental and thermodynamic constraints on the sulphur yield of peralkaline and metaluminous silicic flood eruptions: J. Petrol. 47, p. 1413.

Scaillet, B., and Pichavant, M. (2004) Role of fO_2 in fluid saturation of oceanic basalt: Nature. 430, p. 6999.

Simon, A., Pettke, T., Candela, P., Piccoli, P., and Heinrich, C., 2003, Experimental determination of Au solubility in rhyolite melt and magnetite: Constraints on magmatic Au budgets: Am. Mineral. 88, p. 1644.

Simon, A.C., Pettke, T., Candela, P.A., Piccoli, P.M., and Heinrich, C.A., 2004, Magnetite solubility and iron transport in magmatic-hydrothermal environments: Geochim. Cosmochim. Acta 68, p. 4905.

Simon A. C., Pettke T., Candela P. A., Piccoli P. M. and Heinrich C. A. (2005) Gold partitioning in melt–vapor–brine systems. Geochim. Cosmochim. Acta, 69, 3335.

Simon A. C., Pettke T., Candela P. A., Piccoli P. M. and Heinrich C. (2006) Copper partitioning in sulfur bearing magmatic systems. Geochim. Cosmochim. Acta 70, p. 5583.

Simon A. C., Pettke T., Candela P. A., Piccoli P. M. and Heinrich C. (2007) The partitioning behavior of As and Au in a haplogranite – vapor at magmatic conditions in sulfur-free and sulfur-bearing systems. Geochim. Cosmochim. Acta 71, p. 1764.

Simon A. C., Pettke T., Candela P. A., Piccoli P. M. and Heinrich C. (2008) The partitioning behavior of silver in a vapor–brine– rhyolite melt assemblage. Geochim.

Cosmochim. Acta 72, p. 1638.

Stone W. E., Crocket J. H. and Fleet M. E. (1990) Partitioning of palladium, iridium, platinum, and gold between sulfide liquid and basalt melt at 1200 C. Geochim. Cosmochim. Acta 54, p. 2341.

Toulmin P. and Barton P. B. (1964) A thermodynamic study of pyrite and pyrrhotite. Geochim. Cosmochim. Acta 64, p. 641.

Tsujimura T. and Kitakaze A. (2004) New phase relations in the Cu–Fe–S system at 800 C; constraint of fractional crystallization of a sulfide liquid. Neues Jahrbuch fu¨ r Mineralogie Monatshefte 10, p. 433.

Wallace P. and Carmichael I. S. E. (1992) Sulfur in basaltic magmas. Geochim. Cosmochim. Acta 56, p. 1683.

Werle J. L., Ikramuddin M. and Mutschler M. E. (1984) Allard Stock, La Plata Mountains, Colorado—an alkaline rock-hosted porphyry copper—precious metal deposit. Can. J. Earth Sci. 21, p. 630.

Witter J. B., Kress V. C. and Newhall C. G. (2005) Volca´n Popocate´petl, Mexico: Petrology, magma mixing, and immediate sources of volatiles for the 1994–present eruption. J. Petrol. 46, p. 2337.

Wohlgemuth-Ueberwasser C. C., Ballhaus C., Berndt J., Stotter nee Paliulionyte V. and Meisel T. (2007) Synthesis of PGE sulfide standards for laser ablation inductively coupled plasma mass spectrometry (LA-ICP-MS). Contrib. Mineral. and Petrol. 154, p. 607.

Whitney, J., Hemley, J., and Simon, F., 1985, The concentration of iron in chloride solutions equilibrated with synthetic granitic compositions; the sulfur-free system:

Economic Geology. 80, p. 444.

Wykes, J., Newton, R., and Manning, C., 2008, Solubility of andradite, Ca3Fe2Si3O12, in a 10 mol% NaCl solution at 800 C and 10 kbar: Implications for the metasomatic origin of grandite garnet in calc-silicate granulites: Am. Mineral. 93, p. 886.

VITA
Graduate College
University of Nevada, Las Vegas

Aaron Stephen Bell

Degrees:
Bachelor of Science, Geology, 2006
University of Oklahoma

Awards and Recognitions:

2010	Named a Kalbfliesch Postdoctoral Fellow at the American Museum of Natural History
2008	Mineralogical Association of Canada Research Grant
2008	Society of Economic Geologists Research Grant
2007	UNLV Graduate and Professional Student Association
2006	Nevada Stars Graduate Fellowship
2006	University of Oklahoma, School of Geology and Geophysics Charles N. Gould Award
2005	American Mineralogist Outstanding Undergraduate Award

Publications:

Bell, A. S., Simon, A., and Guillong, M. (2009) Experimental Constraints on Pt, Pd and Au Partitioning and Fractionation in Silicate Melt-Sulfide-Oxide-Aqueous Fluid systems at 800°C, 150 MPa and Variable Sulfur Fugacity. Geochimica et Cosmochimica Acta, 73, 5778– 5792.

Bell , A.S. Simon, A., and Guillong, M. (Submitted) Au Solubility in Hydrous, Chlorine Bearing Basaltic Melts at Variable Oxygen Fugacity. *Submitted to Geochimica et Cosmochimica Acta, 2010

S. Pookpanratana, R. France, M. Blum, A.S.Bell, M. Bär, L. Weinhardt, Y. Zhang, T. Hofmann, O. Fuchs, W. Yang, J. D. Denlinger, S. Mulcahy, T. D. Moustakas, and C. Heske. (Submitted) Chemical structure of vanadium-based contact formation on n-Aluminum-nitride. *Submitted to Physical Review B, January 2010

Bell, A.S., Simon, A., (2009) The effect of sulfur fugacity on Pt, Pd, and Au in Magmatic- Hydrothermal Systems. EoS Transactions: AGU Spring Meeting 2009

Bell, A.S., Simon, A., Guillong, M., Beckett, J. (2009) Alkali and Fe Exchange Between Basaltic Liquids and Supercritical Chloride Solutions at 200MPa and 1298 K: Geochemical Implications for Magmatic Degassing. EoS Transactions: AGU Fall Meeting 2009

Bell, A.S., Simon, A., Guillong, M., Heinrich, C. (2009) REE, HFSE, LILE, and transition metal exchange between basaltic melt and supercritical Cl-bearing aqueous fluid. Geochimica et Cosmochimica Acta, A106. Goldschmidt Conference 2009.

Swenberg, C., Bell, A.S., and Simon, A (2008) Exploring the chemical behavior of the platinum group elements. GSA Cordilleran Sectional Meeting, 9-7.

Simon, A.C. and Bell, A.S. (2007) Iron diffusivity in water saturated rhyolite melt. EoS Transactions: AGU Fall Meeting.

Bell, A.S., Simon, A., Guillong, M. and Heinrich (2007) Experimental constraints on Pt-Pd-Au partitioning in H_2O-haplogranite-sulfide-oxide phase assemblages. EoS Transactions: AGU Fall Meeting

Dissertation Title: An Experimental Investigation of Chemical Mass Transfer in Crystallizing, Hydrous Silicate Magmas: The Genesis of Ore Deposits and Metasomatic Fluids.

Dissertation Examination Committee:
Chairperson, Dr. Adam Simon
Committee Member, Dr. Eugene Smith
Committee Member, Dr. Oliver Tschauner
Committee Member, Dr. Jean Cline
Graduate Representative, Dr. Clemens Heske